Scanning tunneling microscopy of cobalt and iron complexes on metal surfaces

Dissertation

zur Erlangung des Doktorgrades der
Mathematisch-Naturwissenschaftlichen Fakultät der
Christian-Albrechts-Universität zu Kiel

vorgelegt von

Thomas Knaak

Kiel, 2017

Erster Gutachter:	Prof. Dr. Richard Berndt
Zweiter Gutachter:	Prof. Dr. Olaf Magnussen
Tag der mündlichen Prüfung:	23.01.2018

Hiermit erkläre ich an Eides statt, diese Arbeit selbstständig unter der Beratung meiner wissenschaftlichen Lehrer angefertigt und keine weiteren Hilfsmittel, außer den im Text angegebenen sowie den bekannten Nachschlagewerken der Naturwissenschaften, verwendet zu haben. Diese Arbeit wurde weder ganz noch in Teilen an anderer Stelle im Rahmen eines Prüfungsverfahrens vorgelegt. Frühere Promotionsversuche wurden von mir nicht vorgenommen. Die Arbeit ist unter Einhaltung der Regeln guter wissenschafticher Praxis der Deutschen Forschungsgemeinschaft entstanden.
Folgende Teile der Arbeit wurden in wissenschaftlichen Fachzeitschriften veröffentlicht:

- Kapitel 3:

  Thomas Knaak, Manuel Gruber, Christoph Lindström, Marie-Laure Bocquet, Jürgen Heck, and Richard Berndt.

  Ligand-Induced Energy Shift and Localization of Kondo Resonances in Cobalt-Based Complexes on Cu(111)

  Nano Lett. **17**, 7146 – 7151 (2017)

- Chapter 4

  Thomas Knaak, Manuel Gruber, Sarah Puhl, Florian Benner, Alejandra Escribano, Jürgen Heck, and Richard Berndt.

  Interconnected Cobaltocene Complexes on Metal Surfaces

  J. Phys. Chem. C **121**, 26777 – 26784 (2017)

- Kapitel 5:

  Thomas Knaak, Thiruvancheril G. Gopakumar, Bettina Schwager, Felix Tuczek, Roberto Robles, Nicolás Lorente, and Richard Berndt.

  Surface cis Effect: Influence of an Axial Ligand on Molecular Self-Assembly

  J. Am. Chem. Soc. **138**, 7544 – 7550 (2016)

Thomas Knaak

Abstract

In this thesis, structural, magnetic and electronic properties of different classes of transition metal complexes are studied by means of low-temperature scanning tunneling microscopy (STM). Electrospray ionization (ESI) is used for the deposition of these large molecules on metal surfaces. Four different experiments on organometallic complexes on metal surfaces are briefly introduced in the following.

Magnetic sandwich complexes are of particular interest for molecular spintronics. We evidence the successful ESI deposition of a trinuclear organometallic complex, TCBB, composed of three connected magnetic sandwich units, on Cu(111). Scanning tunneling spectra reveal two distinct spatial dependent narrow resonances close to the Fermi level for the trimer molecules as well as for molecular fragments composed of one and two magnetic units. With the help of density functional theory (DFT), these resonances are interpreted as two Kondo resonances originating from two distinct non-degenerate *d*-like orbitals. These Kondo resonances are found to have defined spatial extents dictated by the hybridization of the involved orbitals with that of the ligands.

The investigation of interconnected magnetic sandwich molecules was extended by changing the ligand of the metal center, the organic linker (naphthalene or benzene) and the number of magnetic units. Although these molecules are composed of the same magnetic cobaltocene unit, only one of these compounds shows a Kondo resonance, whose amplitude varies from molecule to molecule. The amplitude variation and its absence for the other investigated complexes are attributed to different molecule-substrate coupling, which is strongly influenced by the linker. Parameters influencing the molecule-substrate coupling and molecular properties are extracted from the experimental data.

Adding ligands to molecules can have drastic and unforeseen consequences for the properties of metal-organic complexes. Little is known about the influence of axial ligands on intermolecular interactions on surfaces. We show a surface cis effect where an axial ligand at adsorbed transition metal complexes enables lateral bonding among the molecules. In the absence of this ligand, FeTMTAA molecules remain isolated at low coverages on Au(111). Exposure to CO leads to axial CO bonding and induces reordering into extended clusters of chiral molecular trimers. The changed self-assembly pattern is due to a CO-induced modification of the molecular structure, which impacts the charge transfer between the molecule and the substrate. In turn, the different charge transfer changes the lateral intermolecular forces.

Spin-crossover (SCO) compounds can be switched between two spin states and are promising building blocks for spin-based applications. Understanding the conditions for stability of SCO complexes on solid surfaces is therefore desirable. We report on the ESI deposition of SCO iron terpyridine (tpy) complexes on Au(111). STM topographs reveal a decomposition of the first complex into single tpy ligands. Three distinct isomeric conformations of the tpy ligand are identified, which is corroborated by gas-phase DFT calculations. In order to minimize the fragmentation on the surface, a second SCO complex with additional carbon linkers was synthesized and investigated. It turned out that this approach does not prevent surface-induced flattening of the complex, but allows the observation of interconnected tpy dimers.

Kurzdarstellung

In dieser Arbeit werden strukturelle, magnetische und elektronische Eigenschaften von unterschiedlichen Übergangsmetallkomplexen mittels Rastertunnelmikroskopie (STM) bei tiefen Temperaturen untersucht. Für die Deposition dieser großen Moleküle wird das Verfahren der Elektrospray-Ionisation (ESI) verwendet. Im Folgenden werden vier unterschiedliche Experimente an metallorganischen Komplexen auf Metalloberflächen vorgestellt:

Magnetische Sandwichmoleküle sind von besonderem Interesse hinsichtlich molekularer Spintronik. Es wird die erfolgreiche ESI Deposition von einem metallorganischen Komplex (TCBB), bestehend aus drei gekoppelten, magnetischen Sandwich-Einheiten, auf Cu(111) gezeigt. Rastertunnelspektren zeigen zwei voneinander räumlich deutlich getrennte, schmale Resonanzen nahe des Fermi-Levels für das Trimer-Molekül, sowie für Molekülfragmente, die aus ein oder zwei magnetischen Einheiten bestehen. Mit der Hilfe von Dichtefunktionaltheorie-Rechnungen (DFT-Rechnungen) werden diese Resonanzen als zwei Kondo-Resonanzen interpretiert, die ihren Ursprung in zwei nicht entarteten *d*-ähnlichen Orbitalen haben. Es zeigt sich, dass diese Kondo-Resonanzen eine definierte räumliche Ausdehnung haben, die von der Hybridisierung der beteiligten Orbitale mit denen der Liganden bestimmt wird.

Die Untersuchungen von gekoppelten, magnetischen Sandwichmolekülen wurden auf Moleküle mit unterschiedlichen Liganden und organischen Verbindern (Naphthalin oder Benzol), sowie zwei oder drei magnetischen Einheiten ausgeweitet. Obwohl diese Moleküle aus den gleichen magnetischen Cobaltocen-Einheiten aufgebaut sind, zeigt nur einer dieser Komplexe eine Kondo-Resonanz, deren Amplitude von Molekül zu Molekül variiert. Die Änderung der Amplitude und das Ausbleiben der Kondo-Resonanz für die anderen untersuchten Komplexe wird Unterschieden in der Bindung zum Substrat zugeschrieben. Die Molekül−Substrat-Bindung ist stark durch den Verbinder beeinflusst.

Das Hinzufügen von Liganden an Moleküle kann drastische und unvorhergesehene Auswirkungen auf die Eigenschaften von metallorganischen Komplexen haben. Dabei ist wenig über den Einfluss von axialen Liganden auf die intermolekularen Wechselwirkungen auf Oberflächen bekannt. Ein Oberflächen-*cis*-Effekt wird gezeigt, bei dem ein axialer Ligand an adsorbierten Übergangsmetallkomplexen eine laterale Bindung zwischen den Molekülen ermöglicht. Ohne diesen Liganden bleiben FeTMTAA Moleküle bei niedriger Bedeckung auf Au(111) isoliert. Die Exposition mit CO führt zu einer axialen CO-Bindung und induziert eine Umordnung der Moleküle hin zu ausgedehnten

Clustern, bestehend aus chiralen Trimeren. Die geänderte Selbstorganisation ist durch eine CO-induzierte Modifikation des Moleküs bedingt, welche den Landungstransfer zwischen Molekül und Substrat verändert. Die Größe des Ladungstransfers bestimmt die lateralen, intermolekularen Kräfte.

Spin-Crossover (SCO) Moleküle können zwischen zwei Spin-Zuständen geschaltet werden und sind vielversprechende Bausteine für spin-basierte Anwendungen. Daher ist es wünschenswert, die Bedingungen für stabile SCO Komplexe auf Festkörperoberflächen zu verstehen. Es wird von der ESI Deposition von SCO Eisenterpyridin (tpy) Komplexen auf Au(111) berichtet. STM Topographien enthüllen die Zersetzung eines Komplexes in zwei einzelne tpy Liganden. Es werden drei unterschiedliche Isomere des tpy Liganden indentifiziert, die mit DFT-Rechungen in der Gasphase übereinstimmen. Um die Zersetzung auf der Oberfläche zu minimieren, wird ein mit zusätzlichen Kohlenstoffketten verstärkter SCO Komplex synthetisiert und untersucht. Es zeigt sich, dass diese Herangehensweise zu einer Oberflächen-induzierten Verflachung der Komplexe führt, die das Auffinden von gekoppelten tpy Dimeren ermöglicht.

Contents

Introduction

Over the last decades top-down miniaturization of electronic devices was the main driving force of technological progress. Beyond increasing the capability of computers, novel applications in data storage, sensing, energy harvesting or medicine will benefit from further miniaturization of numerous technologies. However, there is an inevitable size limit to the miniaturization of nanoscale devices constructed with traditional top-down approaches such as lithography based device design. A bottom-up approach of molecular nanotechnology seem to promise an alternative route to overcome these size limitations [1–8]. Molecular systems promise considerable advances on scalability, component density, cost and power consumption criteria when weighed against solid-state materials [9–11].

Stimulated by the idea of using single molecules as functional building block for electronic devices, researchers around the world pushed the frontiers of both measurement capabilities and fundamental understanding of various physical phenomena at the single-molecule level. Recent experimental advances include the demonstration of conductance [12–16] and magnetic state [17–20] switching, rectification of current [21–23] or light emission [24–29].

For both fundamental and application perspectives, molecules may be attached to electrodes (e. g., surfaces). Yet, the adsorption of molecules on metallic surfaces can have unforeseen consequences and may considerably change the molecular properties. One therefore needs a better understanding of the physics that take place at molecule−metal interfaces. Scanning tunneling microscopy (STM) performed in ultrahigh vacuum and at low temperatures allows to investigate electronic, magnetic, and optical properties of nanostructures on surfaces at the atomic scale [30–35] and is therefore ideally suited for the investigation of single molecules on metal surfaces.

The present thesis is devoted to the investigation of single organometallic molecules on metal surfaces. Organometallic complexes represent an attractive family of molecular material, which combines atomic-level control of organic structure afforded by synthetic chemistry and the electronic and magnetic diversity offered by metallic elements [10, 36]. The aim of this thesis is to contribute to the fundamental understanding of single organometallic molecules and their interaction with metal surfaces.

In particular, this thesis is organized as follows. Chapter 1 gives a short introduction into the basic principles of STM-based molecular physics necessary for the understanding of the results. Of particular interest is the Kondo effect, which can be

utilized as a readout channel of magnetic properties of adsorbed molecules. Since all molecules investigated in this thesis were modeled by density functional theory, the fundamentals of this method are given.

Chapter 2 gives details and characteristics of the experimental setup used for this work.

Chapter 3 deals with the Kondo effect in cobalt-based complexes on metal surfaces. Thanks to a particular hybridization of the metal and ligand orbitals, the Kondo resonances can be independently studied by selecting adequate areas of investigation over the molecule. This is in contrast to magnetic adatoms, where the orbitals at the origin of Kondo resonances may be degenerate and spatially overlap.

Chapter 4 reports on the investigation of magnetic complexes composed of two or three cobaltocene units deposited on metallic surfaces. It is shown that the nature of the linker between the cobaltocene units strongly influences the adsorption geometry and therefore the interaction between the magnetic subunits and the substrate.

In Chapter 5 the influence of axial ligands on adsorbed transition metal complexes is studied. A surface cis effect is shown where axial CO bonding at iron complexes enables lateral bonding among the molecules.

In Chapter 6 the adsorption of iron based spin crossover molecules on Au(111) is investigated. STM topographs reveal a decomposition of the complexes into single terpyridine (tpy) ligands. Three distinct isomeric conformations of the tpy ligand are identified.

The following parts of this thesis have been published in peer-reviewed journals:

- Chapter 3:

  Thomas Knaak, Manuel Gruber, Christoph Lindström, Marie-Laure Bocquet, Jürgen Heck, and Richard Berndt.

  Ligand-Induced Energy Shift and Localization of Kondo Resonances in Cobalt-Based Complexes on Cu(111)

  Nano Lett. **17**, 7146 – 7151 (2017)

- Chapter 4

  Thomas Knaak, Manuel Gruber, Sarah Puhl, Florian Benner, Alejandra Escribano, Jürgen Heck, and Richard Berndt.

  Interconnected Cobaltocene Complexes on Metal Surfaces

  J. Phys. Chem. C **121**, 26777 – 26784 (2017)

- Chapter 5:

  Thomas Knaak, Thiruvancheril G. Gopakumar, Bettina Schwager, Felix Tuczek, Roberto Robles, Nicolás Lorente, and Richardt Berndt.

  Surface cis Effect: Influence of an Axial Ligand on Molecular Self-Assembly

  J. Am. Chem. Soc. **138**, 7544 – 7550 (2016)

1 Fundamentals

1.1 Scanning tunneling microscopy in molecular science

Nowadays, the scanning tunneling microscope is one of the most important tools in surface-based nanoscience [37]. The working principle of STM is to move a metallic tip in close proximity over a surface of interest. If a bias voltage is applied, a tunneling current flows between the tip and the sample. Because the tunneling current is exponentially dependent on the vacuum-barrier thickness, its analysis allows to measure various properties of the surface in real space with atomic resolution. A detailed description of the fundamentals of STM is given in Section 1.2.

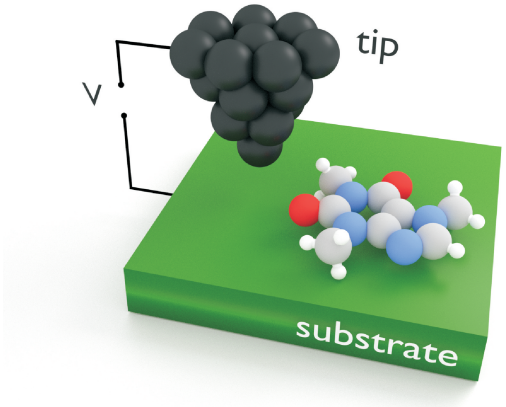

Figure 1.1: Schematic view of the STM working principle.

Soon after its invention in 1981 by Binnig and Rohrer[1] [39, 40], the STM was utilized to investigate molecules. Within a few years, the STM was successfully applied to the imaging of individual molecules on surfaces [41, 42]. STM may be used in combination with an atomic force microscope (AFM) [43, 44] which allows i.a. additional force measurements. To date, the technical progress in scanning probe microscopy enabled various applications in the field of molecular science:

- **Molecule identification.** The atomic resolution of STM/AFM can be employed to verify the structure of synthesized molecules or to determine the organic structure of natural molecules [45–48]. Here, the key step to achieve atomic resolution is the functionalization of the tip apex with a suitable, atomically well-defined termination, such as a CO molecule [45, 49, 50].

- **Electronic structure.** STM is particularly suited to probe the electronic properties of single molecules. Spectroscopic measurements are used to determine the energy of occupied and unoccupied molecular orbitals. Furthermore, the isodensity of molecular orbitals can be inferred from particular topographic measurements [51]. Recently, it was shown that quantum motion of molecules can be probed at the femtosecond-scale [52].

- **Magnetic properties.** The spin state of individual molecules can be inferred from spin-polarized STM (SP-STM) [53] or by taking advantage of the Kondo effect (see Section 1.3) [54]. Moreover, the utilization of magnetic tips in SP-STM allows spin-resolved imaging [55].

- **On surface chemistry.** STM is capable of manipulating objects, like single atoms and molecules [56]. Tip-induced manipulation can be used to modify the conformation of adsorbed molecules [57]. In addition, local chemical reactions involving bond dissociation and formation are feasible [58–61].

Besides the above-mentioned fundamental applications further scanning probe methods address molecular vibration [62], electroluminescence [26–29, 63] or charge effects [64]. Combining these methods STM is a key instrument for the investigation of molecular systems ranging from diatomic molecules to artificial molecular machines [65, 66].

STM and AFM is still an active field and new concepts and measurements come out every day. Certainly, very recent STM techniques like shot noise measurements [67] or electron spin resonance STM [68, 69] will be applied to single molecules.

[1] In 1986 Binnig and Rohrer received the nobel prize in physics for the design of the STM [38].

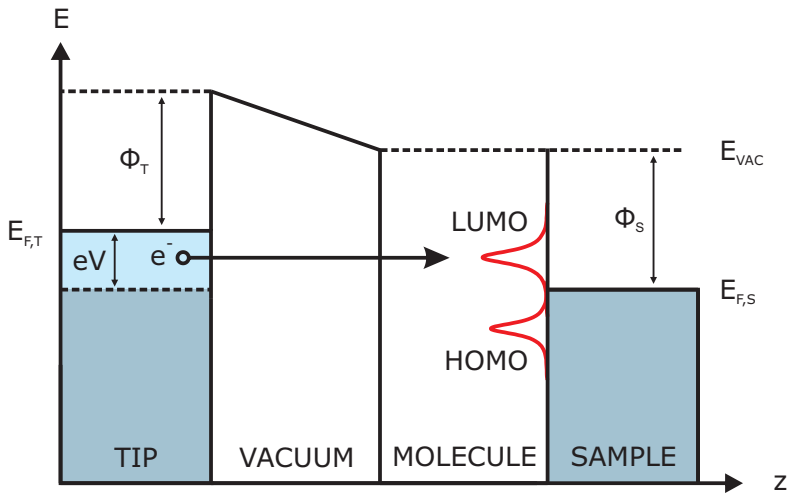

FIGURE 1.2: Schematic diagram of the tunneling barrier junction that applies to molecules on a metal surface. At zero temperature the electronic states of tip and sample up to their Fermi energy $E_{F,T}$ and $E_{F,S}$ are occupied. Φ_T and Φ_S denote the work functions of tip and sample with respect to the vacuum energy level E_VAC. With a positive voltage V applied to the sample the electrons of occupied tip states can tunnel into unoccupied states of the sample.

1.2 Scanning tunneling microscopy and spectroscopy

STM is based on the general principle of moving a probe tip across the surface of a conductive sample to be examined. If the distance z between tip and sample is in the range of a few ångströms, the electron wavefunctions of the tip overlap electron wavefunctions of the sample surface. This allows electrons to tunnel from the tip to the sample or vice-versa. Applying a voltage V between the tip and the sample leads to a tunneling current I, i. e. electrons pass the vacuum barrier between tip and sample. This tunneling current I depends in a first approximation exponentially on the distance z. Thus, the measurement of I as imaging signal enables a precise measurement of the tip−sample distance and therefore facilitates a mapping of the surface including possible adsorbed molecules with atomic resolution.

Actually, I depends additionally on other factors and may be used to provide insight into the electronic properties of the surface. Figure 1.2 shows a schematic diagram of the tunneling barrier. Two metal electrodes, representing tip and sample, are separated by a small tunneling gap. At a temperature of $T = 0$ K the electrons are filled up to the Fermi energies of tip $E_{F,T}$ and sample $E_{F,S}$. When a voltage is applied to the sample, the Fermi energies are shifted by eV to each other. For positive sample voltages the electrons of occupied tip states can tunnel into unoccupied states of the sample.

The transmission probability, $T(z, V, E)$, may be approximated by a one-dimensional trapezoidal tunnel barrier [70, 71]. In the Wentzel-Kramers-Brillouin (WKB) approximation [31, 72] $T(z, V, E)$ reads [31, 73]:

$$T(z, V, E) \propto \exp\left(-\alpha z \sqrt{\Phi + \frac{eV}{2} - E}\right), \tag{1.1}$$

with $\alpha = 2\sqrt{2m}/\hbar$ (m: free electron mass; $\hbar$ Planck's constant divided by 2π), $\Phi = \frac{1}{2}(\Phi_S + \Phi_T)$ is the averaged work function.
For low temperatures, i. e. $T \ll eV/k_B$ (k_B: Boltzmann's constant; $-e$: electron charge), the tunneling current at a tip−sample distance z and a voltage V is then expressed as [31]:

$$I(z, V) \propto \int_0^{eV} \rho_S(E)\rho_T(E - eV)T(z, V, E)dE, \tag{1.2}$$

where ρ_T and ρ_S are the local densities of states (LDOS) of tip and sample, respectively. E denotes the energy of states participating in the tunneling process. Although there are more theories of tunneling specifically applied to the STM [74–80], the one-dimensional WKB tunneling theory is sufficient to describe the data in many cases [31, 81].

In this thesis, molecules adsorbed on metal surfaces are investigated. If a molecule is in the tunneling junction, the electrons can directly tunnel from the tip into unoccupied molecular orbitals (MO) of the molecule (or from an occupied MO to the tip depending on the sample voltage). The highest occupied molecular orbital (HOMO) and the lowest unoccupied molecular orbital (LUMO) are also shown in Figure 1.2. It is often assumed that the states of an adsorbed molecule are pinned with respect to the chemical potential of the substrate. If adsorbed molecules are decoupled from the metal substrate by insulating layers or thanks to their particular structure, a double-barrier tunneling junction has to be considered [24, 51, 82, 83].

For imaging, the tunneling current is usually kept constant using a feedback loop circuit, which varies the tip−sample distance. The vertical displacement of the tip is then used to generate a topography of the surface. Therefore, the STM image reflects the geometry as well as the electronic structure of the surface. In the case of additional adsorbates the interpretation of STM images is thus far from being straightforward. An illustrative example is carbon monoxide on Cu(111). The diatomic molecule reduces the conductance and leads to a depression in constant-current STM images over a range of bias voltages [84, 85].

Scanning tunnneling spectroscopy

It is possible to gain further information on the electronic density of states (DOS) by performing local scanning tunneling spectroscopy (STS). Here, a voltage ramp is applied to the tunneling junction while the tip is kept fixed at a selective position on the sample. At the same time, the differential conductance ($\mathrm{d}I/\mathrm{d}V$) is usually acquired by lock-in technique. The spectral LDOS has to be obtained by normalization from $\mathrm{d}I/\mathrm{d}V$ spectra [78, 81, 86, 87]. At a constant distance ($z = z_0 = \text{const}$) the differential conductance can be approximated to [87]:

$$\frac{dI(z_0, V)}{dV} \propto e\rho_S(eV)T(z_0, V, eV) - \frac{e\alpha z_0}{\sqrt{\Phi}} I(V). \tag{1.3}$$

Here, the tip DOS is assumed to be constant, which is a reasonable approximation if the tip is well prepared. Solving Eq. 1.3 for ρ_S, the LDOS is obtained from constant-distance spectra. The apparent barrier height Φ and the tip−sample distance z_0 may be determined from experimental current-versus-distance data.

Covering a wide range of voltages requires a large dynamic range of current when measuring at constant height. However, excessive currents during spectroscopy can damage or alter molecules at surfaces. This can be avoided by recording spectra at constant and low current, which implies a variation of the tip−sample distance. Therefore, for the normalization a variation of the tip−sample distance $z(V)$ has to be considered. Following Ref. [81] the LDOS can be determined from constant-current spectra via

$$\rho_S(eV) = \frac{1}{eT(z(V), V, eV)} \left\{ \frac{dI(z(V), V)}{dV} + \frac{e\alpha z(V)}{\sqrt{\Phi}} I_0 \right\}. \tag{1.4}$$

I_0 is the constant current set for the measurements. Because the absolute distance $z(V)$ is not known in experiments, it is estimated by $z = z_0 + \Delta z$. The tip excursion $\Delta z(V)$ can be measured simultaneously with recording $\mathrm{d}I(V)/\mathrm{d}V$. In Chapter 5 this procedure was used for the normalization of $\mathrm{d}I/\mathrm{d}V$ spectra of NiTMTAA molecules on Au(111) .

In Chapter 3 and 4 sharp spectral features with a full-width at half-maximum (FWHM) of approximately 30 meV are observed. Besides the intrinsic line width of these features, some broadening may appear, which should be discussed. In general, two broadening mechanisms are important, namely the thermal broadening and the lock-in instrumental broadening.

The thermal broadening is due to the finite width of the involved Fermi levels. It can be roughly estimated by $\Delta E_T \approx 3.5 k_B T$, i. e. $\Delta E_T \approx 0.3$ meV K^{-1} [88–90]. ΔE_T is the FWHM of a thermal-broadening function, which is convoluted with the surface DOS. Most of the experiments presented in this thesis have been performed at a temperature below 5 K, which corresponds to $\Delta E_T \approx 1.5$ meV.

The instrumental broadening depends on the AC modulation of amplitude V_{mod} and is given by $\Delta V_{lock-in} \approx \sqrt{3} V_{mod}$ [89, 90]. An amplitude of 1 mV_{rms} yields therefore a width of $\Delta V_{lock-in} \approx 2.5$ mV ($V_{mod} = \sqrt{2} V_{rms}$).

As the estimated thermal and instrumental broadening is significantly smaller than the width of the spectral features observed in this thesis, it may be neglected.

For a more detailed description of the working principle and measurement modes of STM and STS, the reader is referred to the existing textbooks on this topic [30–35].

1.3 The Kondo effect

The magnetic properties of molecules on conductive surfaces are of great interest with the prospect of future spintronic applications [91]. The so-called *Kondo effect* allows the extraction of certain magnetic properties of molecules with non-magnetic tips and surfaces. The Kondo effect results from the scattering of conduction electrons of a host metal with the localized spin of magnetic impurities [92, 93]. First experimental evidence for the Kondo effect was presented in the 1930s, where measurements on different metals incorporating magnetic impurities showed a resistence minimum at very low temperatures [94, 95]. This stands in contrast to the general finding that the electrical resistance of a metal decreases with temperature as the number of scattering events decreases. The temperature at which the increase of resistivity is observed was termed *Kondo temperature* T_K.

In STS measurements on magnetic atoms or molecules a Kondo resonance can be detected as a narrow conductance peak- or dip-like feature close to E_F (Fig. 1.3a). Thus, evaluation of this *Kondo resonance* permits conclusions about the magnetic state of the analyzed system.

Using STM, the first observations of the Kondo effect on single adatoms were reported in 1998 [97, 98]. From the year 2005 on the Kondo effect was also utilized to investigate the magnetism of metal-organic complexes [54, 99] and is nowadays a widely studied effect [100, 101]. The Kondo effect can be also detected in fully organic molecules, where the impurity spin arises from charge transfer processes [102–104].

Anderson model

The *Anderson single-impurity model* is typically used to explain the Kondo phenomenon [96, 105, 106]. It simplifies the full electronic structure of an adsorbate by assuming only a single d-orbital state which can be filled with one, two or no electrons. The singly occupied $3d$ orbital (d^1) is located below the Fermi energy E_F with a binding energy ϵ. Adding a second electron to the very same orbital increases the energy by the Coulomb repulsion U as sketched in Fig. 1.3. This orbital (d^2) is therefore occupied with opposite spins. Due to the hybridization between the d states and the continuum

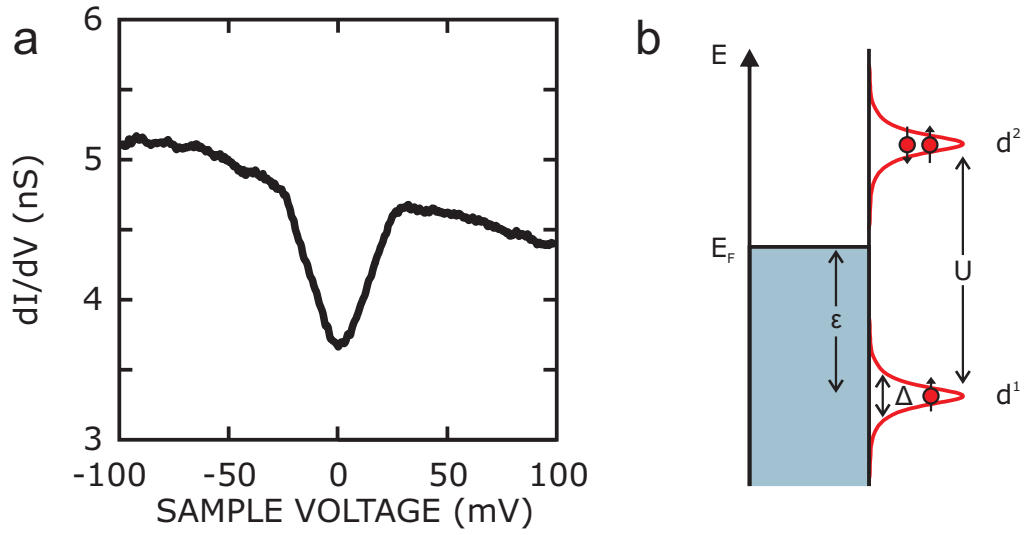

Figure 1.3: (a) Kondo resonance measured on a cobaltocene complex on Au(111). The experimental data is taken from Chapter 4. (b) Schematic drawing of the energy-dependent DOS of a single d orbital in interaction with a metal surface. The singly occupied state d^1 is located at an energy ϵ below the Fermi level E_F and at an energy U below the doubly occupied state d^2. Due to the interaction with the metallic host, the orbital levels have a half-width at half-maximum of Δ. Adapted from Ref. [96].

of electronic states of the metal, the d states are broadened by $\Delta = \rho_0 |V|^2$. Here, ρ_0 is the DOS of the metal at E_F and V the hybridization matrix element that describes the coupling between the d states and the metal conduction electrons [96].

To flip the spin in the singly occupied d state, a bulk electron of opposite spin is needed. Two spin-flip processes are possible in which the d state is either doubly occupied or empty in the intermediate step. Taking into account a multitude of these processes, they modify the energy spectrum by generating a new many-body state close to E_F – the Kondo resonance.

In the Anderson model electrons originating from a STM tip have three possibilities to tunnel into the sample (Fig. 1.4) [96, 107]: They can tunnel directly into empty bulk states above E_F of the substrate (1), into the Kondo resonance (2) or indirectly into the localized state of the magnetic impurity (3). The tunneling current is determined by the interference between spin-conserving channels 1 and 2. Both paths are chosen by the tunneling electrons with probabilities given by the tunneling matrix elements t_1 and t_2 for tunneling into bulk states and the Kondo resonance, respectively.

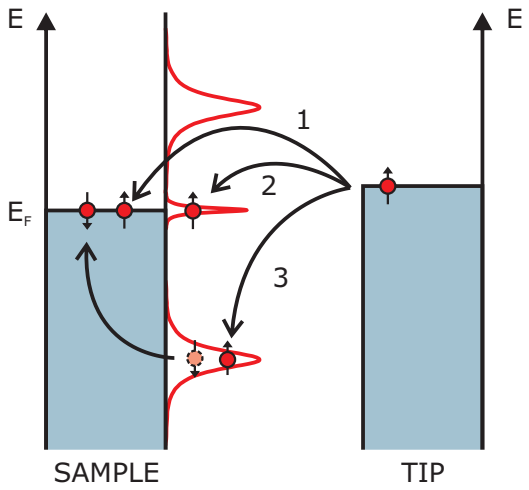

FIGURE 1.4: Possible scattering channels for an electron tunneling from tip to metal through a magnetic impurity adsorbed on a metal surface. Adapted from Refs. [96, 107].

Fitting of the Kondo resonance

To extract quantities from the Kondo resonance the line shape is usually fitted by an appropriate function. In many Kondo studies done by STM/STS the fitting of the Kondo resonance is performed with a Fano function [96, 108–116]:

$$\frac{dI}{dV} \approx A \cdot \frac{(q+\epsilon)^2}{1+\epsilon^2} + B, \tag{1.5}$$

with the asymmetry parameter q, the elementary charge e, the sample voltage V, constants A,B and the energy dependent variable

$$\epsilon = \frac{eV - E_K}{\Gamma_\mathrm{L}}. \tag{1.6}$$

E_K is the energy position of the resonance and Γ_L the half-width at half-maximum (HWHM) of the obtained curve. The Kondo temperature is then described as HWHM at $T = 0$ K [96]:

$$\Gamma_\mathrm{L}(0\mathrm{K}) = k_B T_K. \tag{1.7}$$

The line shape of the resonance is linked to the ratio of the tunneling probabilities t_1 and t_2 [96, 107]. In Equation 1.5 this is incorporated by the asymmetry factor q. For electrons dominantly tunneling into the Kondo resonance ($t_2 \ll t_1$), the q factor is large and the Fano function has the shape of a Lorentzian peak (Fig 1.5). For $t_2 \gg t_1$ q is close to zero and the Fano function has a dip shape. An asymmetric line shape corresponds to intermediate q values.

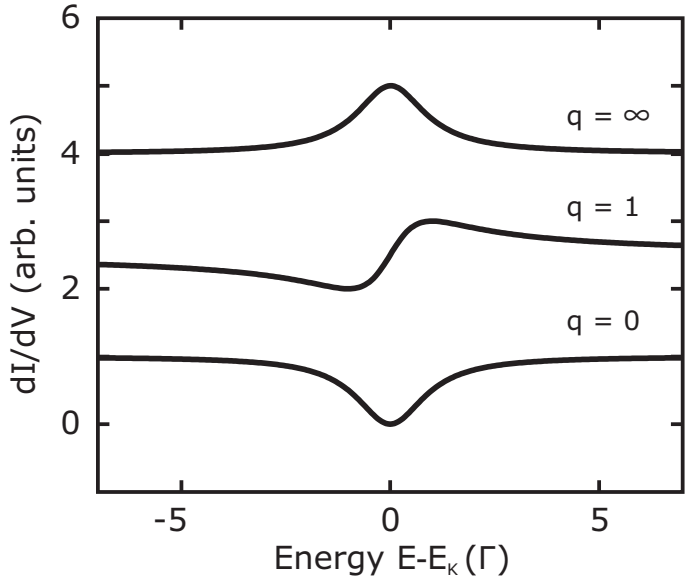

Figure 1.5: Set of curves calculated with the normalized Fano equation (Eq. 1.5) for different q values. The curves are vertically shifted for clarity.

In recent works [83, 101, 104, 117–121] the Fano equation (Eq. 1.5) was exchanged by a Frota function [118, 122] with a background:

$$\frac{\Delta dI}{dV} = A \ \mathrm{Im}\left[ie^{i\Phi}\sqrt{\frac{i\Gamma}{eV - e_k + i\Gamma}}\right] + BV + C. \tag{1.8}$$

The line shape parameter Φ results for even multiples of π in a dip and for odd multiples of π in a peak. The Kondo temperature can be extracted via $T_K(Frota) = \Gamma_{\mathrm{Frota}}/(1.43 \cdot k_B)$ [118]. The Frota function closely reproduces the solution that can be obtained with numerical-normalization group (NRG) theory [117, 123]. A comparison between the Frota function, the Fano function and the resonance calculated with the NRG theory are shown in Figure 1.6. However, some dI/dV spectra of Kondo resonances are better approximated by a Fano function than a Frota function.

Independent of the choice of the fit function, the fit of resonance signals in STS often results in different parameter sets depending on the assumed background and on the energy window of the data taken into account for the fit.

Confirmation by external perturbations

The observation of a zero bias anomaly can have different origins. For example, some features observed at the Fermi level are due to the excitation of low energy vibrations [124–126]. One possibility to confirm the Kondo effect as origin of an observed zero-bias conductance feature is the application of an external magnetic field. When external

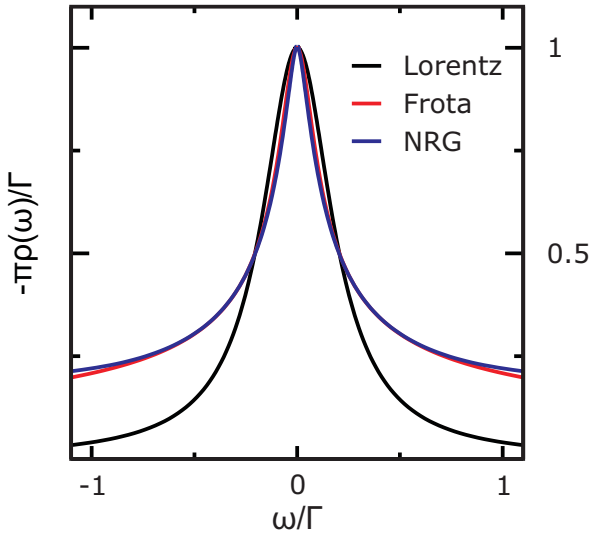

FIGURE 1.6: Comparison of the Kondo resonance calculated with the phenomenological Frota form and Lorentzian. Adapted from Ref. [117].

magnetic fields which exceed the Kondo correlation energy, i. e. $g_0\mu_B B > k_B T_K$ (g_0 is the Landé factor of a free electron and μ_B the Bohr magneton) are applied, the Kondo resonance splits into two distinct parts [101]. The splitting of the resonance scales with the Zeeman energy and depends strongly on the direction of the magnetic field [127]. Experimentally, a Kondo splitting was shown for single adatoms [127–129] as well as for adsorbed molecules [104, 130, 131].

Since the Zeeman splitting as a function of the magnetic field is given by $\Delta = 2g_0\mu_B B$, large magnetic fields of several Tesla are required for a splitting of some meV. Taking into account that spectra are thermally broadened by approximately $3.5k_B T$, i. e. ≈ 0.3 meV K^{-1}, temperatures in the low Kelvin range are an additional requirement for the observation of the splitting. For the experiments presented in this thesis no external magnetic field was available.

Another hallmark of the Kondo effect is a strong temperature-induced broadening of the Kondo resonance. For increasing temperatures, the width of a Lorentzian Kondo resonance broadens with [132]

$$\Gamma_{\mathrm{L}}(T) = \sqrt{(\pi k_B T)^2 + 2(k_B T_K)^2}. \tag{1.9}$$

The match of Equation 1.9 with temperature dependent measurements of the resonance width is often used to attribute zero-bias features to the Kondo effect [54, 102, 115, 132]. It is worth mentioning that the thermal broadening of the Fermi levels introduced by the tunneling mechanism by $\Delta E_T \approx 3.5k_B T$ has to be considered (see Sec. 1.2).

Findings from the Kondo resonance

In the following, the information, which can be obtained by the analysis of Kondo resonances, is presented in a non-exhaustive way:

- **Localization of magnetic moments.** The observation of a Kondo resonance is the evidence of a magnetic moment. Furthermore, spatial resolved STS measurements allow a localization of the involved orbitals.

- **Identification.** The line shape (width and symmetry) of the Kondo resonance may be utilized as a fingerprint of adsorbates. Once the fingerprint is known, it can be used to identify unknown adsorbates on the surface [133].

- **Occupation number.** The occupation number n_d for the $3d$ states of a metal atom can be estimated by the position E_K and the width Γ of the Kondo resonance [96, 112, 134]:

$$n_d = 1 - \frac{2}{\pi} \tan^{-1} \left(\frac{E_K}{k_B T_K} \right). \tag{1.10}$$

  The occupation number ranges between $n_d = 0$ for an empty and $n_d = 2$ for a doubly occupied orbital. Therefore, the occupation of molecular orbitals with an unpaired spin may be estimated.

- **g-factor**. The application of external magnetic fields enables the direct measurement of g values of adsorbates [128].

1.4 Molecular interactions

For the investigation of complex molecules on metal surfaces it is important to understand adsorption and lateral interactions. Firstly, the knowledge of the involved interactions is crucial for the interpretation of STM data of molecules. Secondly, a precise understanding of the mechanisms behind self-assembly is needed to enable the fabrication of well-definded molecular structures in a predictable manner. Therefore, the basic molecular interactions on metal surfaces are shortly reviewed in the following. Table 1.1 gives an overview of the basic molecular interaction types. Additionally, significant STM experiments on metal complexes are discussed.

Interaction type	Energy range	Distance
van der Waals	$E_{as} \approx 0.02 - 0.1$ eV	< 10 Å
Hydrogen bonding	$E_{as} \approx 0.05 - 0.7$ eV	$\approx 1.5 - 3.5$ Å
Electrostatic ionic	$E_{as} \approx 0.05 - 2.5$ eV	up to several nm
Metal−ligand interactions	$E_{as} \approx 0.5 - 2$ eV	$\approx 1.5 - 2.5$ Å

TABLE 1.1: Intermolecular interaction types with associated energies and typical distances. Adapted from Refs. [137, 145].

Adsorption

Depending on the strength of the interaction between an adsorbate and the substrate, adsorption is subdivided into the terms *physisorption* and *chemisorption* [135, 136]. Physisorbed adsorbates are bond to the substrate by weak van der Waals forces with typical binding energies in the order of $10 - 100$ meV [135]. As the interaction is weak, the electronic structure of the molecules is hardly perturbed upon adsorption [136]. To exclude appreciable thermal desorption at room temperature, the adsorption energy per molecule should exceed significantly the thermal energy $k_B T \approx 25$ meV [137].

In contrast, chemisorption corresponds to the case when a molecule forms strong chemical bonds with the substrate atoms. These bonds can be either covalent (with sharing of electrons) or ionic (involving electronic charge transfer [138]). Typical binding energies are in the order of $1 - 10$ eV [135]. The strong interaction changes the electronic structure of the molecules and can even cause their dissociation [139, 140].

For the interpretation of STM data it is therefore crucial to consider the influence of the substrate. In STM experiments ultrathin insulating films can be used to disentangle the electronic structure of adsorbed molecules from the influence of the substrate [51]. Furthermore, adsorption-induced charge transfer has to be taken into account in the analysis of Kondo resonances [102].

In the case of adsorbed metal complexes, the chemical bond strength to the substrate depends on the electronic structure of the metal center [60, 141]. It was shown that the bonding interaction can be altered by dehydrogenation of the ligand [54], the influence of an additional axial ligand [141, 142] or by increasing the coverage [143, 144].

Lateral interaction types

Lateral intermolecular interactions between adsorbed molecules have different origins.

Dipole forces may be related to permanent dipole moments of adsorbed molecules or to the permanent dipoles formed by the adsorption bond due to a charge transfer. This strong and long-range interaction can lead to the formation of highly dispersed superstructures as shown for dipolar iridium complexes on Cu(111) [146]. Fernandez-Torrente *et al.* reported on the formation of a superlattice of nonpolar molecules spaced

several nanometers apart due to localized charges built up at the molecule-surface interface by charge redistribution occurring upon chemisorption [147].

Hydrogen bonding is the electrostatic attraction between hydrogen atoms and highly electronegative atoms such as nitrogen, oxygen or fluorine. The selectivity and directionality of hydrogen bonds offer excellent means for noncovalent synthesis on surfaces [148].

The *van der Waals attraction*, which is due to correlated charge fluctuations, is comparably weak and usually superimposed by stronger interactions, which dominate the net interaction. For physisorbed inert gas atoms at low temperatures van der Waals attraction is the only important force [136].

In addition to these direct intermolecular interactions, it is also possible that the interaction between molecules is mediated by the substrate. An example for substrate-mediated interaction is the oscillatory interaction induced by the two-dimensional electron gas of the surface state, which was proved for separations of up to 7 nm [149, 150].

Generally, the structure formation is governed by the balance between the intermolecular and molecule−substrate interactions. In this thesis, the self-assembly of molecules was controlled by the choice of the substrate (Au, Ag, Cu) and the temperature of the substrate during deposition.

1.5 Spin-Crossover

Coordination compounds of transition-metal ions may, under certain conditions, exhibit a switching phenomenon, whereby the central metal ion changes its spin state upon external perturbations, such as a change in temperature or excitation with light. This phenomenon is known as *spin-crossover* (SCO) [151]. The occurrence of SCO is governed by the relationship between the strength of the ligand (the electrostatic field acting at the central metal ion) and the mean spin-pairing energy. Octahedral complexes of d^{4-7} ions may be either in a magnetic high-spin (HS) or low-spin state (LS), depending on whether the ligand field strength is weaker or stronger, respectively, than the spin pairing energy. The change of spin state is accompanied by a markedly change of the properties of the substance. Most noticeable is the reversible change of magnetic behavior and color, which makes SCO complexes promising candidates for the realization of molecule-based electronic and spintronic components, e. g. switching or memory elements.

Chapter 6 reports on the investigation of Fe(II)bis(terpyridine) complexes. Therefore, the thermal SCO of Fe^{2+} complexes with d^6 electronic configuration will be explained in the following. Figure 1.7a is a simplified illustration of the d orbital configuration in the presence of an octahedral ligand field. The octahedral symmetry of six ligands breaks the degeneracy of the metal ion's d orbitals and splits them into two subsets with an energy difference Δ. If Δ is larger than the spin pairing energy P, the electrons will fill the lower energy orbitals completely leading to the LS state.

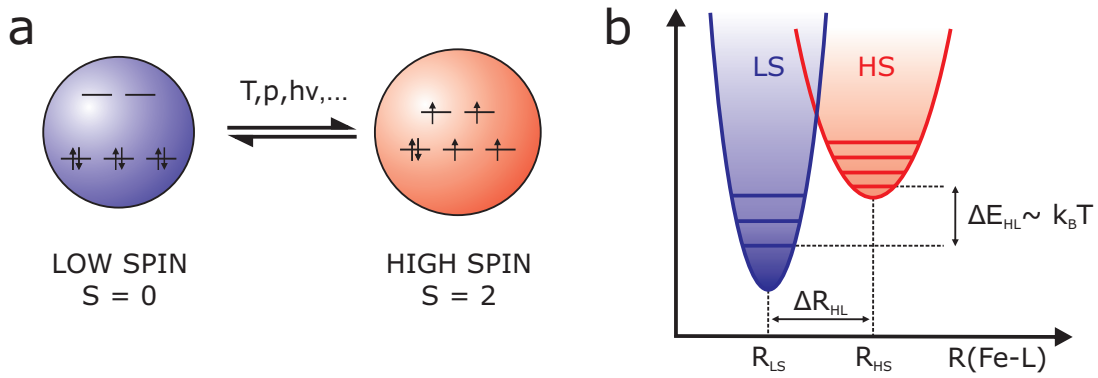

FIGURE 1.7: Schematics of the spin-crossover transition in a $3d^6$ system. (a) If the ligand-field splitting of the d states exceeds the spin pairing energy, a low-spin state with $S = 0$ is obtained. Otherwise the d states are filled according to Hund's rules, resulting in four unpaired electrons and a high-spin state with $S = 2$. Blue and red colors indicate that SCO is mostly accompanied by a color change. Adapted from Ref. [152]. (b) Depletion of charge in the antibonding orbitals during HS to LS transition shortens the metal-to-ligand bond distances. Adapted from Ref. [153].

Conversely, a HS state occurs if the electrons populate the higher energy orbitals before pairing with electrons in the lower lying orbitals ($\Delta < \mathrm{P}$).

Redistribution of charge during HS to LS transition shortens the metal-to-ligand bond distance and reduces the molecular volume (Fig. 1.7b). The change of the bond length is usually in the range $0.1 - 0.2$ Å [151]. The condition to fulfill in order to observe thermally induced SCO is $\Delta E_{HS} \approx k_B T$ [153].

Thermal spin transition occurs nearly exclusively with coordination complexes of $3d$ metal ions [153]. A SCO is not expected for $4d$ and $5d$ transition element compounds. The strength of the ligand field increases notably relative to analogous $3d$ compounds and is therefore generally much larger than the spin pairing energy.

Depending on the system, various stimuli can trigger the SCO:

- **Temperature.** Temperature is the historical SCO trigger and remains the most common stimuli to induce SCO [151]. A typical transition temperature between HS and LS state is 175 K, as reported for $Fe(phen)_2(NCS)_2$ in thin films [154].

- **Pressure.** An increase in pressure usually stabilizes the LS state, i. e. the transition temperature is increased [151]. This can be understood in terms of the volume reduction, which accompanies the HS/LS transition, arising primarily from the shorter metal−ligand bond length.

- **Light.** Light-induced switching of the spin state is triggered by optical excitation with an adequate energy. After excitation the electronic state can relax either to the LS ground state or to the HS state. At sufficiently low temperatures the metastable HS state can have a lifetime of several hours. Thus, the SCO

system can be trapped into the HS state (LIEEST: light-induced excited spin-state trapping). For instance, the magnetic moment of $Fe(bpz)_2phen$ molecules on HOPG was switched by illumination with green light ($\lambda = 520$ nm) [155].

- **Electric field and current.** SCO can be induced by electric field [156] or the tunneling electrons of a STM tip [17, 19]. Those electrons can induce a spin transition with a mechanism similar to the photo-excitation. However, it is experimentally not always possible to unambiguously distinguish between electric field- and current-induced transitions.

- **Magnetic field.** The application of an external magnetic field favors the HS state of SCO molecules and decreases the transition temperature. Qi *et al.* observed a shift of -0.1 K in the transition curve for $Fe(phen)_2(NCS)_2$ in an applied magnetic field of 5.5 Tesla [157].

In bulk and in solution SCO has been extensively studied since the 60s [151]. Nowadays, technological advance of the past years enables the investigation of SCO complexes on surfaces at the single-molecule level [158]. However, the interaction with a surface acts on the metastable balance of the spin states and easily results in a quenching of the SCO transition. Therefore, an important milestone is the reversible switching of single SCO molecules in direct contact with the substrate by a STM [17]. The spin state of the molecules could be determined by the presence (HS) or absence (LS) of a Kondo resonance in the STS spectra.

1.6 Density functional theory

STM is ideally suited for the imaging and investigation of single molecules. However, in many cases it is helpful to complement the experimental results with *ab initio* calculations of the molecule. A basic example is the comparison of STM topographs with the calculated structure of the molecule. A match of dimensions and shape of an imaged adsorbate with the expected molecular structure is already a big step towards the successful identification. Whereas the geometric structure of a molecule can be obtained by other experimental techniques like X-ray crystallography, *ab initio* calculations - ideally including the substrate - may answer further questions concerning the electronic structure and energies of adsorbed molecules.

The ultimate goal of most quantum chemical approaches is the approximate solution of the time-independent Schrödinger equation [159]:

$$\hat{H}\Psi_{mol} = E\Psi_{mol}, \tag{1.11}$$

where $\hat{H}$ is the Hamilton operator for a molecular system consisting of M nuclei and N electrons. In the *Born-Oppenheimer* approximation the electronic Hamiltonian is given by[2] [159]:

[2] Atomic units are used.

$$\begin{aligned}\hat{H}_{elec} &= -\frac{1}{2}\sum_{i=1}^{N}\nabla_i^2 + \sum_{i=1}^{N}\sum_{j>i}^{N}\frac{1}{r_{ij}} - \sum_{i=1}^{N}\sum_{A=1}^{M}\frac{Z_A}{r_{iA}} \\ &= \hat{T} + \hat{V}_{ee} + \hat{V}_{Ne},\end{aligned} \tag{1.12}$$

including the kinetic energy of the electrons $\hat{T}$, the Coulomb repulsion between electrons $\hat{V}_{ee}$, and the Coulomb attraction between nuclei and electrons $\hat{V}_{Ne}$. Except for a few cases, the Schrödinger equation with this Hamiltonian is too difficult to be solved analytically [159, 160]. Also numerical solutions are too complex for most cases, since the many-electron wave function for a N electron system contains $4N$ variables, three spatial and one spin coordinate for each electron.

One successful way of solving the Schrödinger equation is the density functional theory (DFT) [159, 160]. It is based on the fundamental idea of describing a system through its electronic density $n(\mathbf{r})$ instead of its complicated many-body wave function. In the following, a very basic introduction to DFT will be given, followed by a discussion of the exchange-correlation functionals and basis sets, which were used in this thesis.

Hohenberg and Kohn proved that the ground state electronic energy is completely determined by the electron density $n(\mathbf{r})$ [161]. $n(\mathbf{r})$ is a function of only three variables independent of the number of electrons and is therefore much easier to deal with. This enables DFT to be applied to large systems with hundreds of atoms. The ground-state energy can be written as a function of the electron density:

$$E_0\left[n_0\right] = T[n_0] + V_{ee}\left[n_0\right] + V_{Ne}\left[n_0\right]. \tag{1.13}$$

It is advantageous to separate the energy expression into those parts that depend on the actual system, i. e. the potential energy due to the nuclei-electron attraction, and those which are universally valid. Collecting the system independent parts into a new quantity, the *Hohenberg-Kohn functional* $\mathrm{F}_{HK}\left[n_0\right] = T[n_0] + V_{ee}\left[n_0\right]$, it is

$$E_0\left[n_0\right] = F_{HK}[n_0] + V_{Ne}\left[n_0\right]. \tag{1.14}$$

Within the *Kohn-Sham approach* a non-interacting reference system built from a set of orbitals, i. e. one electron functions, is introduced such that the major part of the kinetic energy can be calculated to good accuracy [162]. The remainder is merged with the non classical-contributions to the electron-electron repulsion, which are also unknown but fairly small. By this method, as much information as possible is computed exactly, leaving only a small part of the total energy to be determined by an approximate functional. The energy expression in terms of this separation is:

$$E\left[n\right] = T_S\left[n\right] + J\left[n\right] + E_{xc}\left[n\right] + V_{Ne}\left[n\right] \tag{1.15}$$

where E_{xc} is the so-called *exchange-correlation energy*. E_{xc} contains not only the non-classical effects of self-interaction correction, exchange and correlation, but also a portion belonging to the kinetic energy, i. e. $T \neq T_S$. The subscript S denotes that it is the kinetic energy calculated from a Slater determinant. $J[n]$ is the classical electrostatic energy due to electron repulsion. The next step is to define an effective single-particle potential

$$V_{eff} = V_{Ne}(\mathbf{r}) + \int \frac{n(\mathbf{r'})}{|\mathbf{r} - \mathbf{r'}|} d\mathbf{r'} + V_{xc}(\mathbf{r}), \tag{1.16}$$

where $V_{xc}(\mathbf{r})$ is the exchange-correlation potential as defined as:

$$V_{xc}(\mathbf{r}) = \frac{\delta E_{xc}[n(\mathbf{r})]}{\delta n(\mathbf{r})}. \tag{1.17}$$

This leads to the one-electron Schrödinger-like *Kohn-Sham* equations:

$$\left[-\frac{1}{2}\nabla^2 + V_{eff}\right] \Phi_i = \epsilon_i \Phi_i. \tag{1.18}$$

Here, $\{\Phi_i\}$ are the Kohn-Sham one-electron orbitals with

$$n(\mathbf{r}) = \sum_{i=1}^{N} |\Phi_i|^2, \tag{1.19}$$

The general strategy of DFT is to begin with an initial guess of the electron density, construct V_{eff} from Eq. 1.16 and then get the Kohn-Sham orbitals. Based on these orbitals, a new density is obtained from Eq. 1.19. This procedure is repeated until convergence is achieved. Finally, the total energy will be calculated from Eq. 1.15 with the final electron density.

Exchange-Correlation Functionals

Because the exchange-correlation energy E_{xc} is not known exactly, it is necessary to approximate it. Since the beginnings of DFT different approximated functionals with varying levels of accuracy has been developed [159, 163, 164]. The central goal of DFT is to find better and better approximations to the exchange-correlation energy E_{xc} and the corresponding potential V_{xc}.

A useful way to categorize and improve the E_{xc} functionals is known as "Jacobs ladder" proposed by Perdew [165]. The strategy can be viewed as a ladder with five rungs, leading from the Hartree approximation "on earth" to the exact exchange-correlation "heaven". Thus, the functionals are grouped according to their complexity on the rungs of the ladder. The first rung is the *local density approximation* (LDA), where only the electron density at a point in the system is used for determining this point's contribution to the total exchange correlation energy of the system [160].

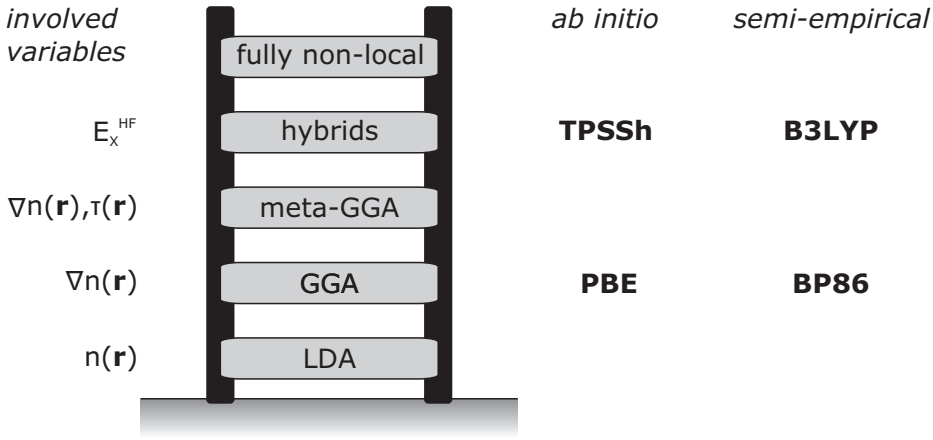

FIGURE 1.8: Schematic diagram of the "Jacob's ladder" of exchange-correlation functionals proposed by Perdew [165] with indication of the involved variables in each rung. The functionals used in this thesis are assigned to the corresponding rung.

The next rung holds the *generalized gradient approximation* (GGA), where the gradient of the density is included in order to account for the non-homogeneity of the true electron density [160]. Prominent representatives are the implementations of Perdew, Burke and Ernzerhof **PBE** [166] and **BP86**, a combination of Becke's exchange functional [167] with Perdew's 1986 correlation functional [168].

The third generation of functionals comprise the *meta-GGA* methods, which depend on higher order derivatives of the electron density, with the Laplacian ($\nabla^2 n$) being the second order term [160]. Alternatively, the functional can be taken to depend on the new introduced orbital kinetic energy density τ.

The *hybrid functionals* of the fourth rung are based on the concept of adding "exact exchange" from Hartree-Fock theory to some conventional treatment of DFT exchange and correlation [160]. Furthermore, the amount of exact exchange in the functionals can be determined through additional, semi-empirical coefficients ("semi-empirical functionals"). The most popular hybrid functional is known as **B3LYP** [169, 170]. For example, the **B3LYP** exchange-correlation energy expression is

$$E_{xc}^{B3LYP} = (1-a)E_x^{LSDA} + aE_x^{HF} + bE_x^{B88} + cE_c^{LYP} + (1-c)E_c^{VWN}. \tag{1.20}$$

The coefficients $a = 0.2$, $b = 0.72$ and $c = 0.81$ are suggested by Becke based on fitting to heats of formation of small molecules. The **B3LYP** functional demonstrated good performances in many chemical applications and is widely used. An example for a nonempirical hybrid functional is the **TPSSh** functional [171, 172]. This meta-GGA functional has been augmented with $\approx 10\%$ exact exchange.

At the fifth level of the Jacob's ladder classification, the full information of the Kohn-Sham orbitals is employed [160]. This means that not only the occupied but also the virtual orbitals are included.

	BP86	**Experiment**	**Deviation**
C1−C8	255.9	255.9	0
C1−C11	1.47	1.48	0,8
Co1−C11	2.22	2.17	1,9
Co1−Co2	6.82	6.74	1,3
C11−C1−C8−C21	32.6	29.7	9,8

Table 1.2: Selected interatomic distances [pm] and torsion angles [°] of the NBC molecule (see Sec. 4) with deviations from experiment [%]. Calculated geometries were obtained at the BP86 def2TZVP level. Experimental values were determined by single-crystal X-ray structure analysis (adapted from Ref. [173]).

In this thesis the well-known functionals **B3LYP**, **BP86**, **PBE** and **TPSSh** have been used for the gas-phase calculations. These functionals offer a good compromise of required accuracy and computational effort [159].

For the calculations performed in the scope of this thesis the reliability of the particular calculations was tested by two different approaches: (i) Calculations have been performed with different functionals to compare the results of pure DFT and hybrid methods. For example, gas-phase calculations of the SCBB molecule (see Chap. 3) were performed with four different functionals (see Fig. A.9). Although the energies of the orbitals vary with the functional, the sequence and the filling of the orbitals are identical. In addition, the spatial distributions of the orbitals found with the different functionals coincide. For the properties used in the analysis all functionals lead to identical results.

(ii) Comparisons between DFT results and experimental observations were made. For instance, Chapter 4 reports on different interconnected cobaltocene complexes. For the smallest compound, NBC, an experimental structure analysis was available [173]. Table 1.2 shows selected interatomic distances and torsion angles of NBC molecules obtained with DFT and single-crystal X-ray structure analysis. Although the Co−C bonds are slightly overestimated, the BP86 functional yield a sufficient agreement with experiment. As the larger compounds also consist of cobaltocene units as chemical building block, it is assumed that their calculations with the same functional yield a similar accuracy.

On-surface calculations of molecules are considerably more difficult and out of scope of this experimental thesis. Therefore, some calculations have been performed by collaborators specialized on DFT calculations. The description of these calculations can be found at the corresponding passage in the thesis.

Basis sets

All electronic structure methods rely on the expansion of the unknown wave functions, i. e. molecular orbitals, by a finite set of basis functions. As a thumb rule, the number of basis functions determines the accuracy of this approximation: The smaller the basis set, the poorer the representation. In contrast, it is important for the computational effort to make the basis set as small as possible. The computational effort scales at least with number of basis functions N_{basis} with N_{basis}^4[160]. In this thesis, the DFT calculations were performed on a NEC high performance system at the University Computing Centre (CAU Kiel) [174] with a peak performance of 64 GFlops of each core. For example, the structure optimization at the BP86/def2TZVP level of a trinuclear cobalt complex with 91 atoms (see Chap. 4) has a job cpu time of 11 days on this system.

Furthermore, the type of basis functions used also influences the performance of the calculation. The better a single basis function is able to reproduce the unknown function, the fewer basis functions are necessary for achieving a given level of accuracy.

The gas-phase calculations in this thesis have been performed using the Gaussian 09 package [175]. This program uses mainly a linear combination of *Gaussian functions* as basis functions. The calculations in this thesis have been carried out with the Gaussian basis set **def2TZVP** of *triple zeta valence* (TZV) quality [176, 177]. This basis consists of three times as many functions as the minimum basis and is partially polarized (P). Polarization functions have by definition more angular nodal planes than occupied atomic orbitals and thus ensure that the orbitals can distort from their original atomic symmetry and better adapt to the molecular environment [159].

The calculation of molecules including the substrate requires the consideration of a much larger number of atoms. These on-surface calculations can be simplified by a periodically treatment of a unit-cell. For the calculation of periodic systems *plane wave* basis sets are the appropriate choice, because they implicitly involve the concept of periodic boundary conditions.

2 Experimental setup

In this chapter, the instruments used for the experiments are briefly described. The majority of data presented in this thesis has been acquired with a commercial STM/AFM [178] (Sec. 2.1) connected to a home-built ESI setup (Sec. 2.2). The results of Chapter 5, were partially obtained with another STM setup. For the description of this home-built apparatus the reader is referred to Ref. [179].

2.1 Low-temperature STM

Figure 2.1 shows the main experimental setup used in this thesis. In total it consists of three UHV chambers: A chamber housing the microscope, a preparation chamber and a so-called load-lock. Additionally, a home-built ESI setup for the deposition of fragile molecules is connected to the preparation chamber, which will be discussed in detail in Section 2.2. All vacuum chambers are separated by pneumatic gate valves. The two main chambers are pumped by turbomulecular, ion getter and titanium sublimation pumps so pressures around 10^{-10} mbar are routinely achieved. The load-lock is a small chamber pumped separately that allows introducing samples and tools to be transferred without breaking the vacuum in the other chambers.

In the preparation chamber samples can be cleaned by sputtering and annealing. For that purpose, the chamber is equipped with a sputter gun and a gas inlet. The samples can be heated by resistive button heater on the sample holder. The temperature of the sample is directly monitored by a thermocouple.

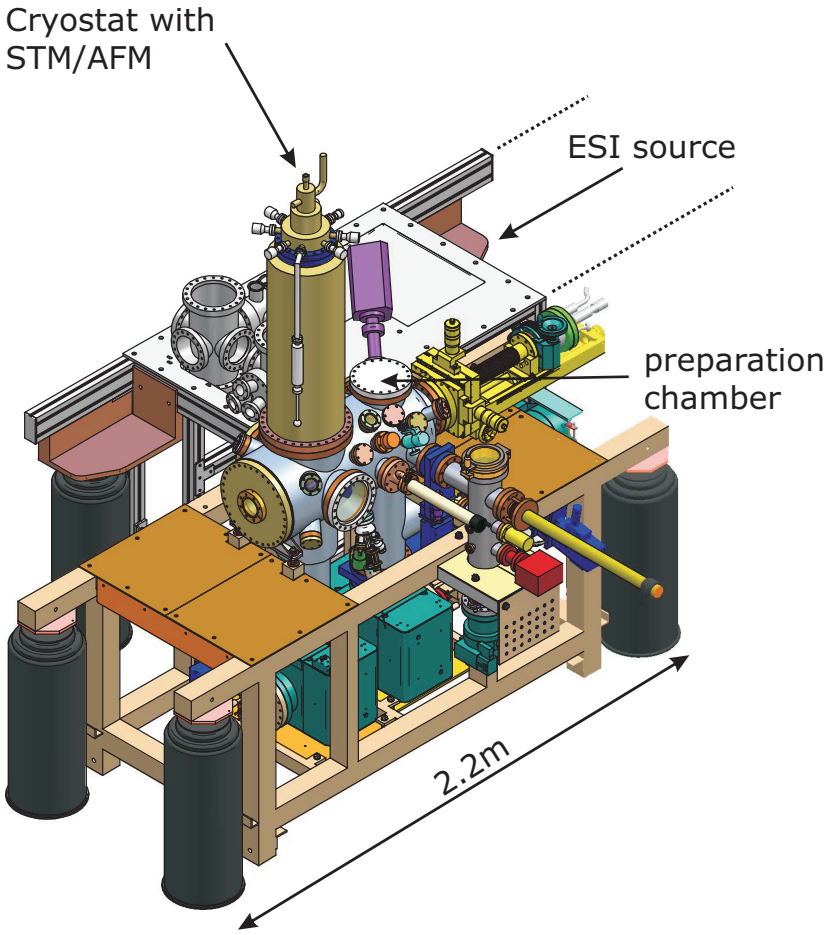

FIGURE 2.1: A combined low-temperature scanning tunneling and atomic force microscope (LT-STM/AFM) consisting of three chambers. A home-built electrospray ion source (grey) can be used for the *in situ* deposition of molecules. Adapted from Refs. [180, 181] by permission of the authors.

The deposition of molecules can be performed either from a Knudsen cell or from the electrospray ion source. A rotatable manipulator, which can be cooled to liquid nitrogen temperature, is used during sample preparation and for the transfer to the microscope chamber. A bath cryostat is mounted on the microscope chamber with a capacity of 4 l of liquid helium and 13 l of liquid nitrogen. It affords sample temperatures below 5 K during STM measurements.

To avoid vibrations during STM measurements, the complete instrument can be lifted by a pneumatic damping system. What is more, the base plate of the STM is attached to the helium cryostat via three springs.

The scanner of the STM is based on the Besocke beetle-type design [182, 183]. The microscope is controlled with electronics and software from Nanonis [184]. The

tunneling current is amplified using a DLPCA-200 amplifier from FEMTO Messtechnik GmbH [185], which has a bandwidth of 1.1 kHz (7 kHz) at a gain of 10^9 V/A (10^8 V/A). Differential conductance measurements are performed with a SR830 DSP lock-in amplifier from Stanford Research Systems [186] while a sinusoidal modulation is added to the sample voltage.

If not stated otherwise, all STM images shown throughout this thesis, were acquired in constant current mode using a constant voltage applied to the sample electrode and the tip on ground. After the acquisition all images were processed using WSxM [187].

2.2 Electrospray Ion Source

In this thesis the electrospray ion-beam deposition technique is applied for the deposition of large organometallic molecules. Therefore, an introduction to the ESI technique is given in the following. Afterward, the home-built ESI setup used in this thesis is presented.

For the investigation of single molecules with STM the first step is their deposition onto a surface in a controllable and reproducible way. The most common method for molecular deposition is thermal sublimation. However, this technique is restricted to small and stable molecules. Such molecules can be rather easily deposited because high vapor pressures can be reached before the molecules decompose.

Recent advances in synthetic molecular chemistry have resulted in complex organic and inorganic compounds that provide special functionalities or properties. For instance, large multinuclear transition-metal complexes [188–191], molecular magnetic switches [192, 193] or platform based functional compounds [194–197] have been successfully synthesized recently. Unfortunately, large molecules typically decompose before any sublimation occurs, because the vapor pressure usually decreases quickly with increasing molecular size [198, 199].

Therefore, various alternative techniques have been developed for the deposition of large molecules in UHV. These include *ex situ* techniques, such as the simple treatment with a droplet of solution or Langmuir-Blodgett films [200]. These techniques are able to deposit nonvolatile molecules to a surface, but the intermittent exposition to air can lead to unwanted adsorbates on the surface. *In situ* techniques avoid this contamination by performing all preparation steps under controlled UHV conditions.

Electrospray ionization was introduced by Fenn[1] *et al.* for mass spectrometry [198]. ESI is a soft-ionization technique that accomplishes the transfer of molecules from solution to gas phase. By now, ESI has become a prevalently used technique in mass-spectrometry [202]. Adopted to the deposition on surfaces this methods retains the capability of mass-filtering [203, 204]. Here, ESI deposition has an advantage over other *in situ* techniques like pulse injection [205] or dry-imprinting [206], which have

[1] John B. Fenn was awarded with the Nobel prize in chemistry in 2002 [201].

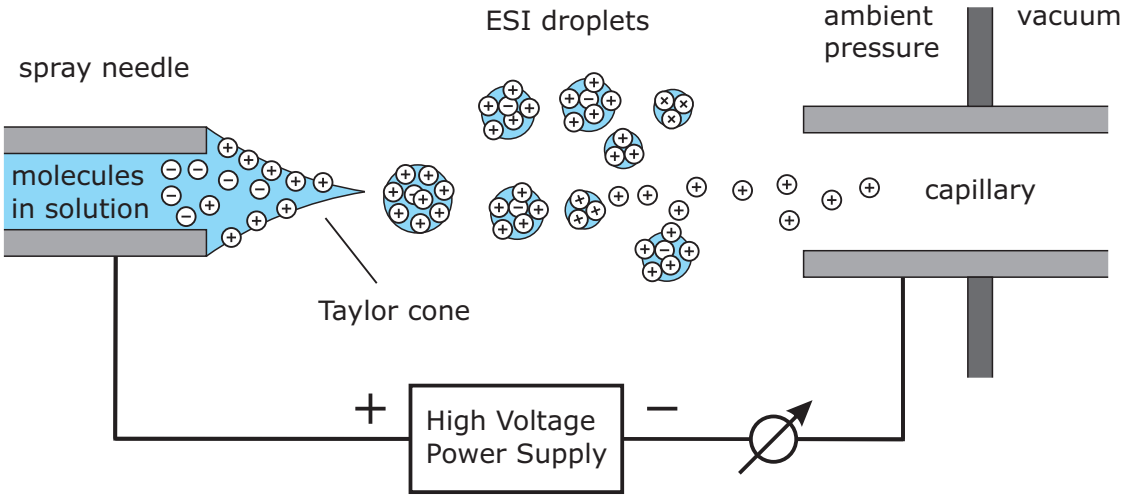

FIGURE 2.2: Schematic depiction of the electrospray ionization process. Adapted from Ref. [208].

no mass-filter ability. In combination with scanning probe microscopy the ESI technique was first implemented in 2006 by Rauschenbach *et al.* [207].

Figure 2.2 shows a schematic representation of the ESI process. Initially, the molecules of interest are solved in a volatile solvent. The resulting solution is guided through a needle facing a capillary for the gas inlet. A high voltage applied between the needle and the capillary results in a strong electric field at the needle's apex. This electric field causes a charge separation in the liquid. If the field is strong enough, the charged surface of the liquid forms a so-called *Taylor cone* [209], which ejects a fine jet of liquid droplets from its apex towards the capillary. Since the charge density is highest at the tip of the cone, the resulting droplets are charged. In the electric field the droplets of the jet are accelerated towards the counter electrode. Simultaneously, the droplets are driven away from each other due to their charge by Coulomb repulsion.

On their way to the gas inlet electrode the droplets shrink due to the evaporation of neutral solvent molecules. In addition, the evaporation of the solvent is further supported by a heated gas flow in counter direction. While the size of the droplets is thereby reduced the charge density on their surface is continuously increased. As soon as electrostatic repulsion exceeds the competing force of surface tension, disintegration of the droplets into smaller sub-units occurs [210]. The point at which this critical size of the charged droplets is reached is known as *Rayleigh limit* [211]. The iteration of solvent evaporation and Coulomb fission finally results in desolvated molecular ions. The final step to individual gas phase ions is surprisingly difficult and remains an active area of research [202, 212]. At last the gas phase ions enter the capillary and are

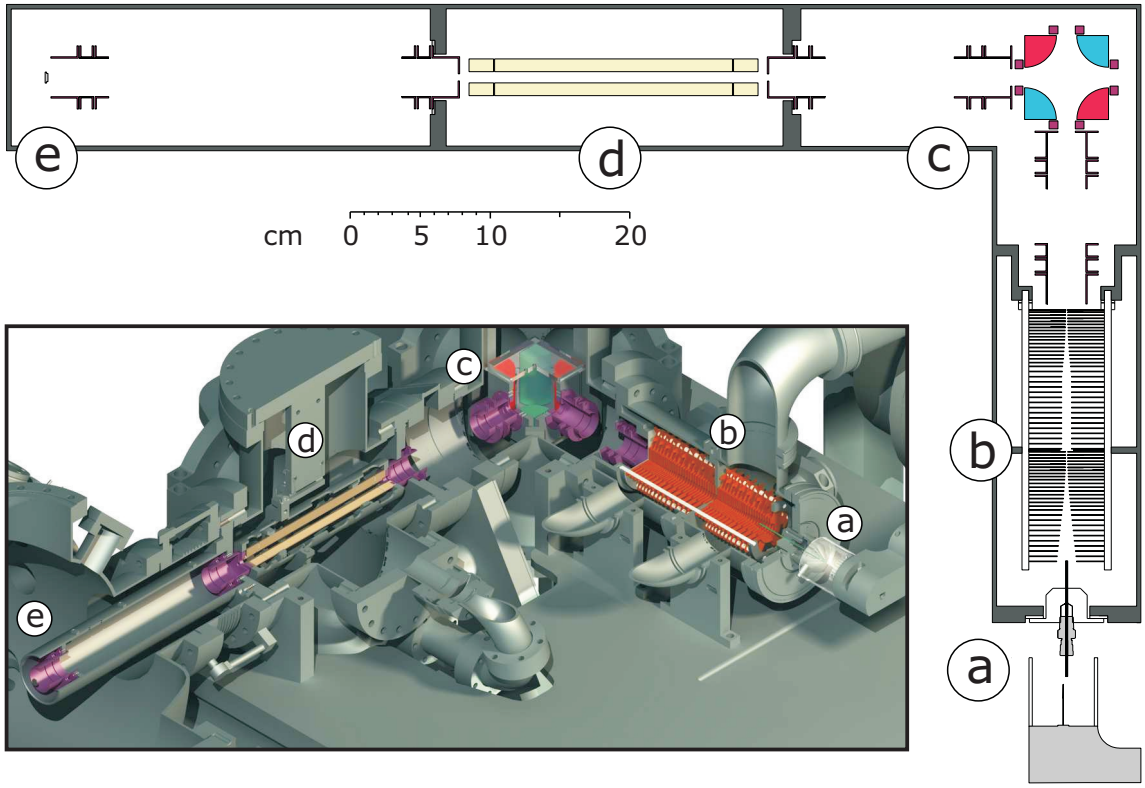

Figure 2.3: Electrospray ionization deposition setup. (a) Spray needle and desolvation capillary for ambient pressure ESI. (b) Radio frequency ion funnel. (c) Electrostatic quadrupole deflector for separation of charged particles. (d) Quadrupole mass filter. (e) Ion deposition on the sample. Adapted from Ref. [180] by permission of the author.

available for analysis or deposition purposes.

The ions produced in the ESI process may be quasimolecular ions created by the addition or removal of hydrogen ions [180, 202]. Ionic metal complexes are ionized by the removal of their counter ions [213]. This is the case for the organometallic complexes investigated in this thesis. Depending on the charge of the molecules, ESI is operated with a different polarity of the applied voltages (positive/negative ion mode). It is quite common for ESI to form multiple charged species. Advantageously, this allows the detection of large analytes within a limited m/z range.

The home-built ESI apparatus (Fig 2.3) used in this thesis was designed and built by Christian Hamann [180, 214]. After the actual ESI process the ions enter the system trough the desolvation capillary (a). The system consists of five differentially pumped vacuum chambers to bridge the pressure gap of 12 order in magnitude. In all vacuum stages, guiding and focusing of the ion beam are done by electrostatic ion optical lenses.

To increase the transmission through the setup the ions are first guided trough a so-called ion funnel setup (b). It is composed of a series of ring electrodes to which both radio frequency (RF) and direct current (DC) potentials are applied. The alternating RF fields result in a repulsive so-called RF pseudopotential, which accelerates charged particles towards the ion funnel axis, while the DC potentials drive the ions to the next stage.

The focused ion beam is afterward redirected by a electrostatic quadrupole deflector (c). The deflection from the ion funnel axis by 90° prevents neutral contamination, e. g. solvent molecules, from reaching the ultrahigh vacuum preparation chamber. Additionally, the deflector acts as energy filter, which is used to control the mean impact energy at the substrate.

A quadrupole mass spectrometer is used for the mass spectrometric analysis of the ion beam (d). This allows the identification of all molecular species in the ion beam. After this, the spectrometer can be set to a specific mass to charge ratio to filter unwanted charged particles out of the beam.

Finally, the ion beam is conducted to the sample in the preparation chamber (e). To prevent fragmentation on the substrate the impact energy of the ions can be further reduced by a decelerating electric field.

The current of the ion beam can be measured at different locations of the setup by a picoammeter. This way it is possible to characterize and optimize the produced ion beam step by step. The measurement directly at the sample surface during the deposition allows for estimating the achieved coverage. The ion current at the sample is typically in the range of $10 - 50$ pA. Dependending on the current a deposition time of 30 min up to several hours is needed for useful coverages, e. g. 0.05 ML. Each molecule deposition requires the optimization of the ion transmission by adjusting a multitude of settings, e. g. the voltages for the optical lenses.

Since I started my thesis several parts of the setup were improved so that it differs slightly from the description in Refs. [180, 214]. A new designed ion funnel was built in [215] and the pumping of the last stage was improved by an additional cryo pump.

By now, this ESI setup was successfully used for the deposition of high mass biomolecules like DNA [180, 214], metal complexes [216–218] and complicated organic compounds [181, 215, 219, 220]. In this thesis, the setup was used for the first time for the deposition of interconnected transition metal sandwich compounds.

3

Ligand-Induced Energy Shift and Localization of Kondo Resonances in Trinuclear Cobalt-Based Complexes on Cu(111)

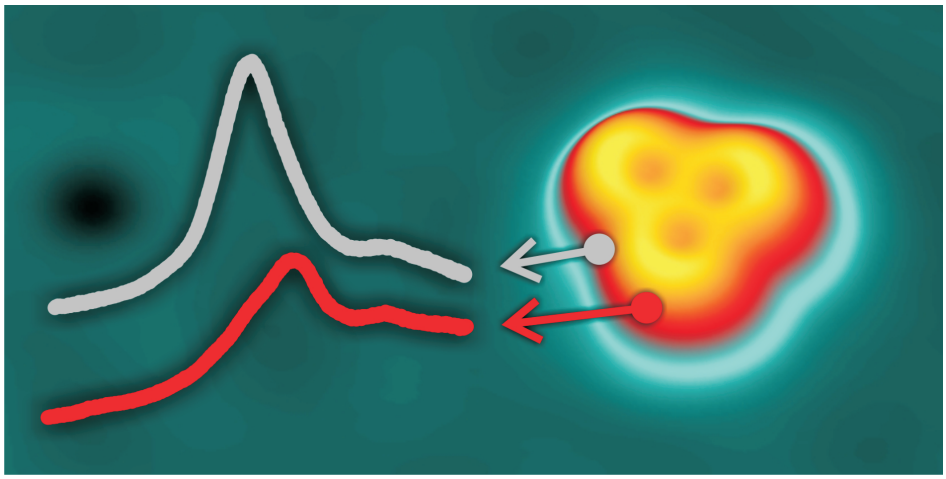

3.1 Introduction

Molecular spintronics is a fertile research field aiming to exploit the spin of electrons within molecules [221, 222]. Considerable attention is focused at the interface between molecules and metallic substrates as intriguing magnetic properties emerge [152, 223–230]. Of particular interest is the Kondo effect, which is notably employed as a readout channel of magnetic properties of adsorbed molecules [17, 54, 104, 139, 231–241]. The Kondo effect results from the interaction between a localized magnetic moment (e. g., at a magnetic adatom or molecule) and conduction electrons of a nonmagnetic substrate, leading to a resonance in the excitation spectrum close to the Fermi energy [92, 112]. In scanning tunneling spectra, an approximate Fano line shape is observed close to zero bias [97, 98, 108]. When the spin of the investigated magnetic object is 1/2 and only one orbital is singly occupied, the broadening and the energy of the Kondo resonance may be used to extract the Kondo temperature, which is related to the strength of the interaction, and the electronic occupation of the involved orbital, respectively [96]. A similar analysis is often performed for a single Kondo resonance appearing in more complex magnetic systems that involve more than one partially occupied orbital ($S > 1/2$). However, in these cases the extracted information may be inaccurate or incomplete. Indeed, each partially occupied orbital can lead to a Kondo resonance forming a Kondo channel and different Kondo channels may interfere. Such multi-orbital Kondo systems would nevertheless represent an ideal playground for strongly correlated physics provided that information from the different Kondo channels are separately retrieved.

Despite numerous studies of the Kondo effect on molecular systems adsorbed on metal surfaces [17, 54, 104, 115, 121, 130, 131, 139, 231–250], there is little experimental evidence suggesting the involvement of more than one orbital in the Kondo effect [251, 252]. The main difficulty in such systems is that the different Kondo resonances almost always appear at the same spatial location and the same energy, making it difficult to disentangle the contributions of different orbitals. To the best of our knowledge, only the study by Pacchioni *et al.* [252] clearly evidence a two-orbital Kondo system where each Kondo resonance is observed at different spatial locations. However, the two resonances have similar energies and the magnetic atom of the metal-organic complex is in direct contact to the substrate hindering possible engineering of the Kondo-interaction strength.

Here, we report on low-temperature scanning tunneling microscopy investigation of a trinuclear sandwich complex interconnected by a benzene unit, deposited on Cu(111). It is substituted in the 1, 3, and 5 positions with the η^6-borabenzene-η^5-cyclopentadienylcobalt complex (TCBB) forming an overall threefold symmetry (Fig. 3.1a). TCBB molecules along with fragments composed of one and two magnetic centers are observed on the surface. Each of these three adsorbates exhibits two distinct spatially-varying resonances close to the Fermi level. With the help of density functional theory calculations, the resonances are interpreted as Kondo resonances originating from two distinct partially-occupied *d*-like orbitals. These Kondo

resonances are found to have defined spatial extents determined by the hybridization of the "Kondo" orbital with ligand orbitals. Furthermore, the ligand field splits the degeneracy of the partially occupied orbitals, so that the two Kondo resonances occur at slightly different energies.

3.2 Methods

Synthesis of the molecules: TCBB molecules were synthesized according to Ref. 253 based on an earlier work on heterobimetallic complexes [254].

Tip and sample preparation: STM tips were electrochemically etched from tungsten wire and further prepared in situ by indentation into the substrate. The Cu(111) single-crystal surface was prepared by successive cycles of Ar^+ sputtering and annealing to 500 °C. The molecules were deposited using an home-built electrospray ionization setup with mass selection [214] (see Appendix A), which already demonstrated its potential to deposit fragile magnetic molecules [217, 218]. During the deposition the pressure at the sample stayed below 2×10^{-9} mbar.

STM: The measurements were carried out with a STM operating in ultrahigh vacuum at 5 K (Createc, Berlin). Differential conductance spectra were acquired using a lock-in amplifier (root-mean-square modulation voltage of 1.4 mV at 770 Hz) while the feedback loop was open.

DFT (Gas Phase): We used the BP86 functional [167, 168] with the def2TZVP basis set [176] using Gaussian 09 [175] (see Appendix A for comparison with other functionals).

DFT (on Surface): Ab initio calculations were performed with the DFT + U approach, wherein the strong electron−electron Coulomb interactions that exist in the open $3d$ shell of the $3d$ cobalt ion are captured by the supplemented Hubbard and exchange constants U and J. In the present calculations U and J were taken to be 4 and 1 eV, respectively. These values were previously shown to provide the correct spin state for adsorbed cobalt porphyrins [255]. We employed the VASP full-potential planewave code, in which pseudopotentials together within the projector augmented wave method are used [256, 257]. A kinetic energy cutoff of 400 eV was employed for the plane waves. For the DFT exchange-correlation functional the generalized gradient approximation was used, in PBE parametrization [166]. The metallic surface was modeled through four atomic Cu layers and a p(7 x 7)-Cu(111) unit cell at a single k-point (Gamma). The atomic position of the two topmost layers and the molecule were relaxed until forces were smaller than 0.05 eV/Å. An important tool is the projected density of states of the adsorbed system onto a molecular orbital (MO), where MO is the free-molecule state onto which the density of states is projected. The MO is calculated for the free molecule distorted to its chemisorption geometry. The PDOS is informative of the molecular character of the chemisorbed system and has been successfully used a previous study of surface reactivity [258].

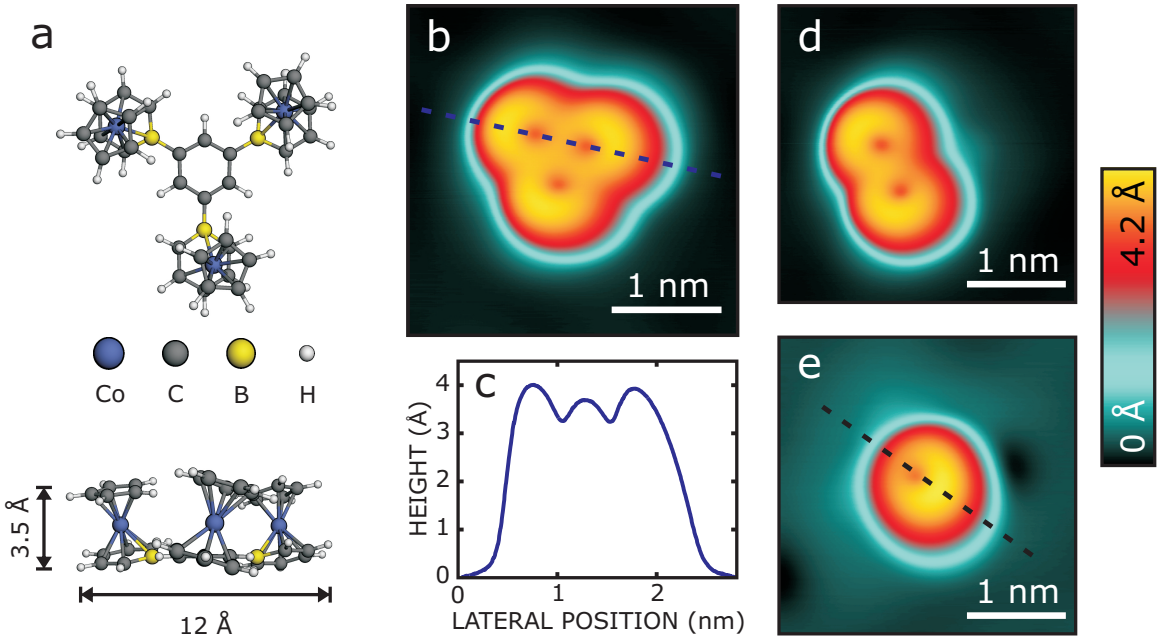

FIGURE 3.1: (a) Top and side views of the calculated gas-phase structure of TCBB. (b) Constant-current STM topograph ($I = 200$ pA, $V = 0.1$ V) of TCBB on Cu(111). (c) Height profile of TCBB on Cu(111) along the line shown in (b). STM topographs ($I = 200$ pA, $V = 0.1$ V) of (d) DCBB and (e) SCBB molecules. The dashed line in (e) indicates the symmetry axis as defined in the main text.

3.3 Results and Discussion

TCBB molecules are composed of three η^6-borabenzene-η^5-cyclopentadienylcobalt (CBB) units connected by a benzene ring (Fig. 3.1a). The CBB units consist of a Co atom coordinated by cyclopentadienyl (Cp, C_5H_5) and borabenzene (BC_5H_5) ligands. The connection of the CBB units to the benzene ring is realized through the B atom of the borabenzene ligands. The base of the TCBB molecule, composed of three borabenzene ligands connected to the benzene ring, has an overall triangular-like shape (top view in Fig. 3.1a), where each side of the triangle has a length of 12 Å (side view in Fig. 3.1b). The three CBB units extrude from the base of the molecule in the same direction, leading to a molecular height of 3.5 Å. Since the CBB units are connected to the benzene ring only through a B atom, the relative orientation of the CBB molecular axis can vary. This is corroborated by gas-phase DFT calculations (see details below) where the calculated TCBB molecule exhibits three CBB units tilted relative to each other (side view in Fig. 3.1a). We note that the CBB units are similar to but different from metallocene molecules, which are composed of a metal atom sandwiched by two Cp rings [121, 259–262].

Upon deposition of TCBB on Cu(111), isolated adsorbates with three ring-like protrusions exhibiting an apparent height of up to 4 Å are observed (Figs. 3.1b,c). The STM topograph of TCBB matches the calculated gas-phase structure in lateral and vertical dimensions and symmetry (Fig. 3.1a,b). Indeed, the adsorbate exhibits a threefold symmetric shape with a width of 17 Å compared to the 12 Å width of the calculated structure (Fig. 3.1a,c). This apparent discrepancy is expected as the topograph is related to the overlap of the molecular orbitals with those of the tip. Although the experimental data cannot unambiguously prove that the CBB units remain connected on the surface, the adsorbate observed in Fig. 3.1b will be considered as a single TCBB molecule. From the arguments described below, we deduce that the TCBB molecule is adsorbed through its base (containing the benzene ring) on the surface. The Cp rings of the three CBB units are facing upward, each of them imaged as a ringlike protrusion in topographs (Fig. 3.1b). Yet, the line profile over two CBB units exhibits three peaks (Fig. 3.1c), the middle one being lower than the ones at the extremities. As further discussed in Appendix A, this is a consequence of a tilt of the CBB units toward the center of the TCBB molecule. The tilt of the CBB units is also reflected by the fact that the depression (dark spot) corresponding to the center of the Cp ring is not observed at the center of the ring structures. As shown in Appendix A, the tilt of individual CBB units within TCBB may be modified upon tip-induced manipulation. The link between the tilt of the sandwich molecules and the position of the depression is discussed in Refs. 121, 260, and 261.

In addition to TCBB, smaller adsorbates with only two or one rings are observed (Fig. 3.1d,e). These adsorbates are ascribed to molecules with two or one CBB units, which will be referred to as double CBB (DCBB) and single CBB (SCBB), respectively. Since the settings of the mass spectrometer (see Appendix A) only allowed transmission of intact TCBB molecules, SCBB and DCBB molecules presumably result from the fragmentation of deposited TCBB molecules. Topographs of SCBB and DCBB molecules reveal off-center depressions in the ringlike structures, indicating a tilt of the CBB units (see Appendix A), similar to TCBB. To simplify the discussion below, we define the symmetry axis (SA) of a CBB unit as the axis passing through the center of the ring-like structure and the depression (e. g., dashed line in Fig. 3.1e).

To investigate the magnetic and electronic properties of the adsorbed molecules differential conductance spectra $\mathrm{d}I/\mathrm{d}V(V)$ were measured. Since the observed spectroscopic features are independent of the number of CBB units per molecule (see below and Appendix A), we first discuss the case of SCBB molecules. Figure 3.2a shows typical spectra acquired over two different positions on a SCBB molecule. The tip positions during acquisition are marked in the inset of Fig. 3.2a. The spectrum measured atop the lower-left part of the molecule (i. e., off the SA of the molecule; I) exhibits a narrow resonance near the Fermi energy. Interestingly, atop a position along the SA (II), the $\mathrm{d}I/\mathrm{d}V$ spectrum shows a peak but with a different line shape. For completeness, a spectrum acquired over the bare Cu(111) substrate (blue) is shown. This spectrum

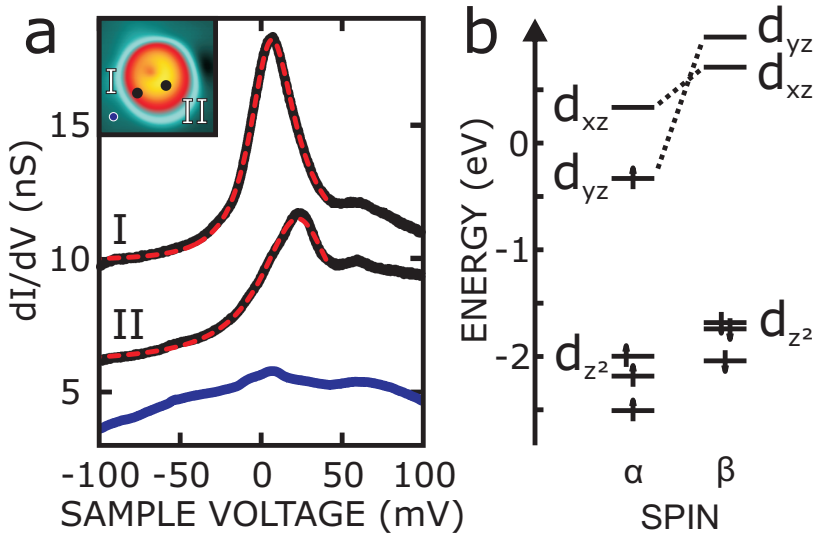

FIGURE 3.2: (a) dI/dV spectra of a SCBB molecule on Cu(111). The spectra were acquired at two positions over SCBB (I, II) and over bare Cu(111) (blue). The feedback loop was opened at $V = 100$ mV, $I = 500$ pA. The spectra are vertically shifted by 0, 5, and 8 nS, respectively. Fano fits of the Kondo resonance are shown as dashed red lines. The inset shows the positions used for spectroscopy. (b) Calculated electronic structure of gas-phase SCBB. Molecular orbitals are labeled according to their d-character. The Fermi level was defined halfway between SOMO and LUMO.

does not exhibit any characteristic, tip-related features so that associated modification of the molecular spectra is negligible.

The sharp resonances close to the Fermi energy suggest a Kondo resonance as reported for single magnetic adatoms [97, 98, 109, 113] or organometallic molecules [17, 54, 104, 115, 121, 130, 131, 139, 231–250] adsorbed on metallic substrates. Molecular states can be excluded because additional measurements of SCBB molecules on Au(111) reveal a broadening of the molecular states of about 1.3 eV (see Appendix A), that is, much larger than the narrow resonances shown in Fig. 3.2a. Furthermore, the molecule−substrate electronic coupling likely increases in going from a Au(111) to a Cu(111) substrate. Therefore, we expect that the molecular states of SCBB molecules on Cu(111) are broader than on Au(111). This is in agreement with the dI/dV spectra of SCBB molecules on Cu(111) over a larger voltage range of 3 V (see Appendix A), where the molecular states are barely discernible due to their large widths. Furthermore, since the Kondo temperature scales with the Kondo impurity−substrate coupling [96, 112], the decrease of the electronic coupling on Au(111) compared to that on Cu(111) is consistent with the nonobservation of a Kondo resonance at 5 K on SCBB on Au(111).

Considering the above arguments and DFT calculations (discussed below), we ascribe the origin of the narrow resonances presented in Fig. 3.2a to Kondo resonances. Both resonances are fitted with a Fano function [96, 108, 112]:

$$\frac{dI}{dV} \approx A \cdot \frac{(q+\epsilon)^2}{1+\epsilon^2} + B, \tag{3.1}$$

with the asymmetry parameter q, the elementary charge e, the sample voltage V, constants A, B and the energy-dependent variable

$$\epsilon = \frac{eV - E_K}{\Gamma}. \tag{3.2}$$

E_K is the energy position of the resonance and $T_K = \Gamma/k_B$ stands for the Kondo temperature. The Fano fits are superimposed on the experimental spectra in Fig. 3.2a. The agreement is remarkable. A comparison to fits with a Frota function [118, 122] is presented in Appendix A. It is worth mentioning the presence of an additional feature at the right side of the resonance. This feature is compatible with a very broad d-like orbital expected for II as discussed below and in Appendix A. Although this feature was excluded from the fit range, it affects the accuracy of the fit parameters for II, which therefore are provided for illustration only. The Fano fit on I (II) yields a Kondo temperature T_K of 201 K (320 K), $q = 11$ (85), and an energy shift of $E_K = 5.1$ meV (22.2 meV). We reproduced the measurements over a large number of SCBB molecules with different tips. Small variations were observed between different spectra leading to the following fit-parameter ranges: $T_K = 201 - 271$ K ($251 - 320$ K), $q = 5 - 100$ ($39 - 265$), and $E_K = 0 - 7.2$ meV ($21.4 - 24.9$ meV) for I and II, respectively.

The Fano fits of spectrum I reveal Kondo temperatures (T_K) and form factors (q) in the same range as those for spectrum II. The main difference between spectra I and II is the mean energy of the Kondo resonance E_K of 4.1 and 23.0 meV, respectively. This actually suggests that two different Kondo resonances are observed.

To check this hypothesis, we performed spin-resolved DFT calculations of SCBB molecules in the gas phase and for the molecule adsorbed on Cu(111). We first describe the results of the gas-phase calculations. Figure 3.2b presents the calculated electronic configuration of the gas-phase SCBB molecule. The d orbitals of the cobalt atom are strongly hybridized with the orbitals of the ligand rings. To simplify the discussion, the molecular orbitals are nevertheless labeled according to their major Co d-character. SCBB has a spin state $S = 1/2$ with an unpaired electron in the d_{yz} orbital [253, 263]. It represents the singly occupied molecular orbital (SOMO) of the complex. The d_{xz} orbital is the lowest unoccupied molecular orbital (LUMO). As a Kondo resonance requires a partially filled orbital [96, 112], we will consider the d_{yz} and d_{xz} orbitals in the following. The possible involvement of the d_{yz} orbital to the Kondo resonance is obvious as the calculations reveal a single charge in the orbital. Separately, the d_{xz} orbital may also lead to a Kondo resonance, as the adsorption of the molecule leads to a broadening of this orbital along with a possible shift in energy and a charge transfer.

This is corroborated by DFT calculations of SCBB on Cu(111). Indeed, the LUMO (d_{xz}) becomes occupied by approximately one electron upon adsorption of the molecule. The calculations therefore suggest two orbitals (d_{yz} and d_{xz}) to potentially be at the origin of the observed Kondo resonances.

In order to test the involvement of the d_{yz} and d_{xz} orbitals, further information is extracted from the fit parameters. Indeed, the average occupation of the Co d state involved in the Kondo resonance, referred to as the occupation number n_d, reads [96, 112, 134]:

$$n_d = 1 - \frac{2}{\pi} \tan^{-1}\left(\frac{E_K}{\Gamma}\right). \tag{3.3}$$

The occupation number ranges between $n_d = 0$ for an empty and $n_d = 2$ for a doubly occupied orbital. The Fano fit parameters of resonance I (II) yield an average occupation number $n_d \approx 0.9$ (0.5), validating our hypothesis. We nevertheless stress that the estimates of n_d are certainly not quantitative but are presented for qualitative comparison. Considering that the occupation extracted from the Kondo resonance I is larger than that of II, we suggest that the Kondo resonance I (II) originates from the d_{yz} (d_{xz}) orbital. It should be mentioned that the occupation number of 0.9 found for I corresponds to the typical Kondo regime ($0.8 < n_d < 1.2$) [264], whereas II is at the crossover between the Kondo and mixed-valence regimes [112]. At the crossover, the Kondo resonance starts to merge with d state responsible for the resonance. In that case the feature appearing for II at the right side of the resonance is compatible with the expected very broad d_{xz} state (see Appendix A).

As discussed above, the calculated electronic configuration of gas-phase SCBB is compatible with the two Kondo resonances observed experimentally. More precisely, the SOMO (d_{yz}) and LUMO (d_{xz}) orbitals presumably are responsible for the Kondo resonances I and II (Fig. 3.2), respectively. Yet, there is a second requirement for the Kondo effect, that is, the "Kondo" orbital must be electronically coupled to the conduction electrons of the substrate [96, 112]. In the present case, such an electronic coupling is related to the spatial extents of the "Kondo" orbitals, and more specifically to their overlap with substrate states.

Figure 3.3a shows top and side views of calculated isosurfaces of the SOMO and the LUMO. Both orbitals involve a Co d orbital that is strongly hybridized with ligand π orbitals (side view in Fig. 3.3a). Because of the strong hybridization, the SOMO and LUMO orbitals extend over the entire molecule. In particular, both orbitals are spatially extended over the borabenzene ligand. This is a prerequisite for a strong hybridization with the substrate which the borabenzene ligand is in direct contact with. Furthermore, the density of states projected onto the SOMO and LUMO is strongly affected upon adsorption of the molecule on Cu(111) (see Appendix A). This independently indicates a strong coupling between the molecular orbitals and the substrate. These observations further corroborate the involvement of the SOMO and the LUMO in the experimentally observed Kondo resonances.

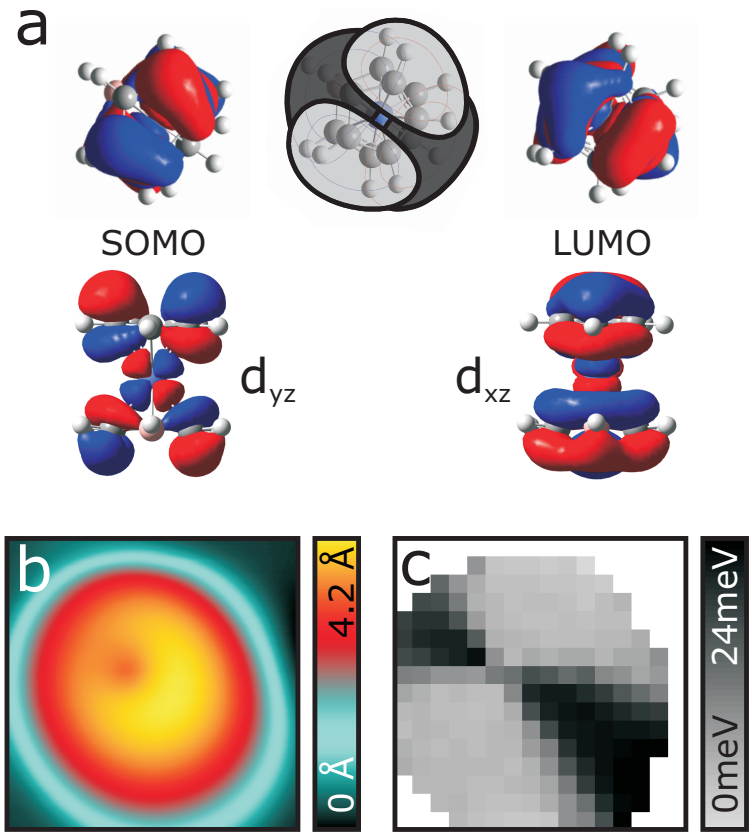

Figure 3.3: (a) Top and side views of the calculated wave functions of the SCBB SOMO and LUMO. The inset presents a top view of the SCBB molecule. Bright and dark colors qualitatively indicate the areas where the SOMO and LUMO are dominating, respectively. (b) Constant-current STM topograph of SCBB on Cu(111). (c) Spatial distribution of the resonance position (E_K) extracted from a grid of 16 × 16 spectra measured over the area shown in (b).

Interestingly, while the SOMO and LUMO both extend over the entire molecule, their spatial distributions remain different. Indeed, the SOMO exhibits a nodal plane, which passes through the Co atom, the center of the borabenzene ligand and the B atom (Fig. 3.3a). It is worth mentioning that the SA defined earlier is oriented along this nodal plane. From the top, the SOMO appears as two elliptical shapes separated by the nodal plane. The LUMO also presents a nodal plane, which, however, is perpendicular to that of the SOMO. Owing to their hybridization with the ligands the "Kondo" orbitals have particular spatial extents, which we address experimentally below. The inset of Figure 3.3a shows a top view of the SCBB molecule, divided into bright and dark areas. The shading indicates positions where the Kondo resonances I and II are respectively expected to be dominating.

To investigate the spatial distribution of both Kondo resonances over a SCBB molecule, a grid of 16×16 spectra was measured in the area shown in Fig. 3.3b. As the two Kondo resonances mainly differ by their positions E_K, each spectrum was fitted with a Fano function and the resulting peak positions (E_K) are displayed in the color map in Fig. 3.3c. Although some spectra exhibit two resonances (see Appendix A) just one Fano function was used for the fit. Consequently, the map qualitatively shows the spatial distribution of the two resonances. The map shows bright and dark areas, which correspond to areas where resonances I and II are dominating, respectively. The combination of the dark and bright areas, that is, locations where a resonance is observed in the corresponding spectrum, has the form of a circle with the size of the SCBB molecule (Fig. 3.3b,c). The dark areas extend along the SA, while the bright areas cover the rest of the SCBB molecule. The experimental map (Fig. 3.3c) remarkably matches the expectation from the DFT calculations (inset of Fig. 3.3a). A difference is nevertheless noticeable, as the two dark areas have different sizes in the experimental data. Indeed, the upper left dark area is smaller than the lower right area. This is due to the tilt of the molecule toward the upper-left corner, which is not accounted for in the calculated shape of the SOMO and LUMO.

Finally, we have demonstrated that (i) the occupation numbers extracted from the Kondo line shape parameters are consistent with the calculated electronic structure of SCBB, namely with the SOMO (d_{yz}) and LUMO (d_{xz}); (ii) both SOMO and LUMO extend over the borabenzene ligand allowing a strong hybridization with the substrate and (iii) the experimental spatial extents of the Kondo resonances I and II match those of the calculated SOMO and LUMO. We therefore attribute the Kondo resonance I (II) to the SOMO (LUMO).

STS measurements performed on the TCBB and DCBB molecules yield essentially the same results as observed for SCBB (see Appendix A). Each CBB unit shows the same Kondo features, independently of the total number of CBB units per molecule. Therefore, we deduce that within our energy resolution the CBB units are magnetically decoupled from each other. This observation is corroborated by our gas-phase computational analysis. In a simple picture the molecular orbitals of TCBB close the Fermi level reproduce SCBB molecular orbitals three times. We speculate that, by an adequate chemical engineering of the central connecting ligand, it may be possible to magnetically couple the CBB units.

In conclusion, we reported the ESI deposition of a trinuclear organometallic complex, TCBB, on Cu(111). Differential conductance spectra of SCBB, DCBB and TCBB molecules revealed two Kondo resonances with different spatial extents and different energies. In contrast to magnetic adatoms, where the orbitals at the origin of Kondo resonances may be degenerate and spatially overlap, here the strong ligand field lifts the orbital degeneracy. Furthermore, thanks to a particular hybridization of the metal and ligand orbitals, the Kondo resonances can be independently studied by selecting adequate areas of investigation over the molecule. A related approach may provide insights into complex Kondo systems with several “Kondo” orbitals.

4

Interconnected cobaltocene complexes on metal surfaces

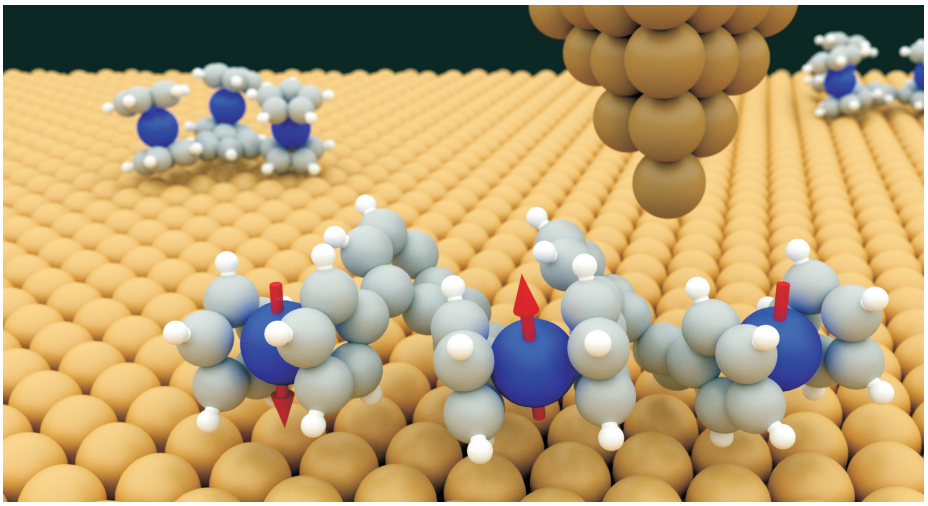

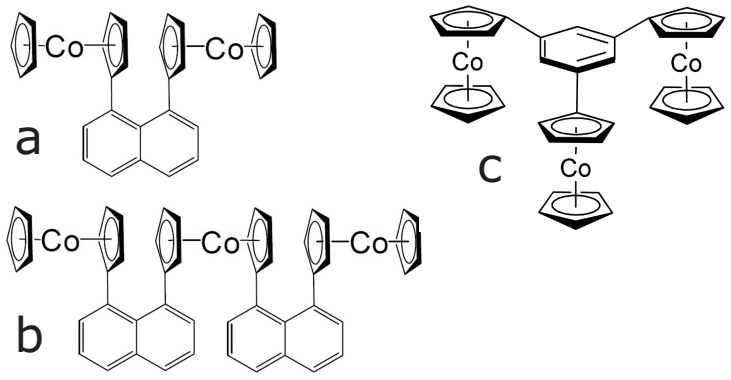

FIGURE 4.1: Schematic representation of the investigated complexes: (a) Naphthalene bridged biscobaltocene (NBC) and (b) triscobaltocene (NTC). (c) Benzene bridged triscobaltocene (BTC).

4.1 Introduction

Organometallic complexes are promising candidates for molecular spintronics [17, 19, 91, 222–226, 230, 265–268]. These complexes may posses a spin whose interaction with the substrate can lead to rich physics, such as the Kondo effect [17, 83, 121, 241, 249, 269–272]. Besides interaction of molecular spin centers with the substrate, it is desirable to couple the spins of different molecular complexes. This may be realized through particular interaction mediated by the substrate, e. g. RKKY interaction [228, 273], or by connecting the magnetic centers using chemical groups [188–190, 205, 244, 249, 274, 275]. The latter approach offers the opportunity to tune the interaction between the magnetic centers by a proper selection of chemical linkers.

Metallocenes are particularly interesting as building blocks of interconnected magnetic centers. These organometallic sandwich compounds consist of two cyclopentadienyl rings (C_5H_5, Cp) bonded to a metal center [276]. A wide variety of metallocenes with distinct magnetic properties may be realized by exchanging the metal center [277]. Furthermore, the Cp ring of the metallocene may be connected by organic groups in order to couple the magnetic centers [274, 278–281]. Various classes of interconnection designs were reported, ranging from simple fused-ring ligands to complex molecular switches [282, 283]. The coupling between the magnetic centers may be realized through the linker or the linker imposes a particular molecular arrangement where the π orbitals of one metallocene overlaps with that of the other metallocene [173, 284]. However, when the molecules are adsorbed on a surface, depending on the nature and size of the linker, it may enforce particular adsorption geometries of the molecule on the surface. In turn, different adsorption geometries can lead to different coupling to the substrate and subsequently affect the magnetic properties of the adsorbed molecules.

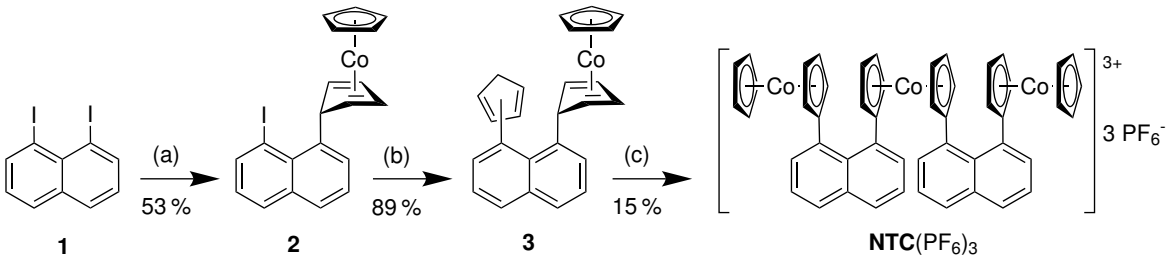

Figure 4.2: Synthesis of the trinuclear complex $NTC(PF_6)_3$; Reaction conditions: (a) 1) ^{n}BuLi/Et_2O, 2) $[CoCp_2]I/Et_2O$; (b) CpZnCl, CuI/thf; (c) 1) ^{n}BuLi/thf, 2) $CoCl_2$, 3) H_2O, O_2, NH_4PF_6.

Here, we report on a low-temperature scanning tunneling microscopy (STM) and spectroscopy investigation of three oligocobaltocene complexes deposited on metallic surfaces (Figure 4.1). The complexes, consisting of two or three cobaltocene ($CoCp_2$) units linked by naphthalene or benzene groups, were successfully deposited on metal surfaces. The $CoCp_2$ units linked by naphthalene (molecules a and b) are orientated horizontally on the surface whereas the $CoCp_2$ units linked by a benzene ring are oriented vertically. Differential-conductance measurements reveal a dip, compatible with a Kondo resonance, only for the smaller complex, naphthalene bridged biscobaltocene (a, NBC). The amplitude of the resonance strongly changes between different $CoCp_2$ units. The change of the resonance amplitude and its absence for the two other investigated complexes, are attributed to different molecule−substrate coupling, which is strongly influenced by the linker.

4.2 Experimental and Theoretical Methods

Synthesis of the molecules

$BTC(BF_4)_3$ (Ref. 285) and $NBC(BF_4)_2$ (Ref. 286) were synthesized according to literature. For the synthesis of the trinuclear target compound $NTC(PF_6)_3$ (Figure 4.2) 1,8-diiodonaphthalene **1** acted as the starting material. By using one equivalent *n*-butyllithium a mono iodine lithium exchange was performed, followed by a nucleophilic attack at cobaltocenium iodide leading to the asymmetric cobalt(I)-complex **2**. Subjected to a cross-coupling reaction with cyclopentadienyl zinc chloride in the presents of copper(I) iodide the cyclopentadiene functionalized cobalt(I) complex **3** is formed as a mixture of two isomers. No attempts were made to separate the isomers as the cyclopentadiene substituent is deprotonated and allowed to react with cobalt(II) chloride in the following step. Oxidation of the resulting central cobaltocene unit and hydride abstraction at the two remaining cobalt(I)-complexes finally yields the tricationic cobaltocenium complex $NTC(PF_6)_3$.

Sample preparation

The Au(111) and Cu(111) single-crystal surfaces were prepared by successive cycles of Ar^+ sputtering and annealing to 500 °C. STM tips were electrochemically etched from a tungsten wire and further prepared *in situ* by indentation into the substrate.

The deposition of the molecules on the metallic substrates was performed using two different methods. NBC molecules were sublimed from a Ta crucible heated at $\approx$ 150 °C, while the larger NTC and BTC molecules were deposited using an home-built electrospray ionization (ESI) setup with mass selection [214, 218, 272]. Stable spray conditions were achieved with NTC$(PF_6)_3$ (BTC$(BF_4)_3$) molecules dissolved in nitromethane. The deposition of NTC (BTC) molecules was performed by selecting a mass-to-charge ratio of 271 u/e (213 u/e) at a relative kinetic energy of approximately 1 eV (9 eV). The spray voltage was 3.7 kV (3.4 kV). During deposition, the pressure stayed below 2×10^{-9} mbar and the substrates were kept at room temperature.

STM

The measurements were carried out with a STM operating in ultrahigh vacuum at 5 K (Createc, Berlin). All STM topographs were acquired in the constant-current mode. The differential conductance was measured using a lock-in amplifier with a voltage modulation of 3.5 mV at a frequency of 1 kHz. The current feedback was turned off for spectroscopy while the sample voltage was swept.

DFT

DFT calculations were carried out using the Gaussian 09 software using the BP86 functional and the def2TZVP basis set [167, 168, 175, 176].

4.2.1 Results and Discussion

Naphthalene bridged biscobaltocene

The molecular structure of 1,8-bis(cobaltocenyl) naphthalene is presented in Figure 4.1a. The complex consists of two $CoCp_2$ units linked to a naphthalene at the position 1,8. Single-crystal X-ray structure analysis [286] indicate a head-to-head arrangement of the two $CoCp_2$ units (Figure 4.1a). The steric repulsion of the two cofacially arranged Cp ligands induces a twist angle between the naphthalene and the Cp-ring planes of approximately 47°. Furthermore, the C−C bonds between the Cp ligands and the 1 and 8 positions of the naphthalene have a torsion angle of 25°. The distance between the two cobalt atoms is 6.4 Å.

Deposition of approximately 0.5 ML of NBC molecules on Au(111) leads to the formation of molecular chains as well as disordered clusters (Fig. 4.3a,b). The length of the chains ranges from a few nanometers to some tens. The orientation of the chains

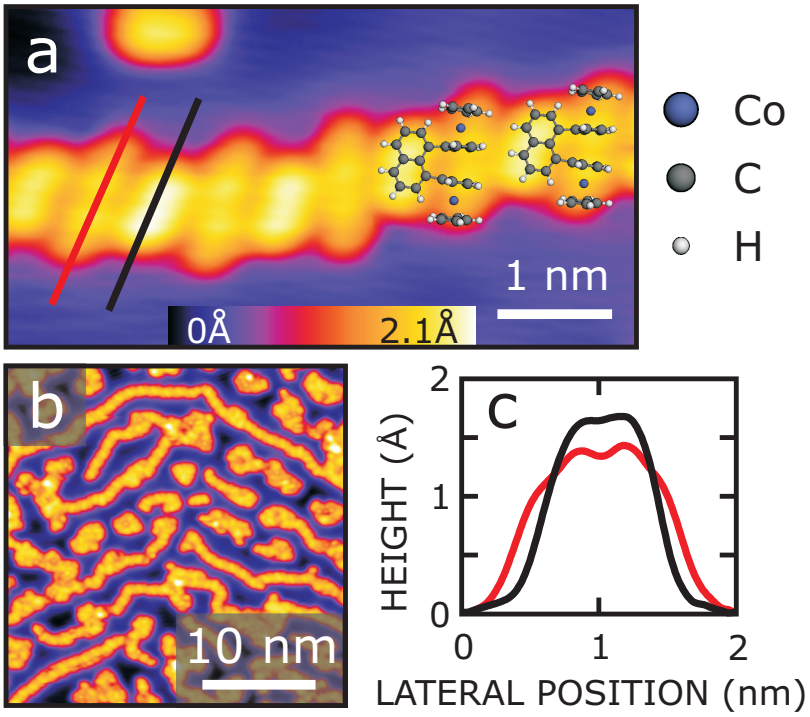

Figure 4.3: (a) STM topograph ($I = 30$ pA, $V = 0.2$ V) of a NBC molecular chain on Au(111) with two superimposed scaled molecular models of NBC. The geometry of the model is taken from Ref. 287. (b) Large-scale STM topograph ($I = 30$ pA, $V = 0.1$ V) revealing relatively long NBC molecular chains and NBC molecular islands on Au(111). (c) Height profiles over two flat-lying cobaltocene units (red) and a naphthalene linker (black) of NBC on Au(111). The profiles are taken along the colored lines indicated in (a).

follows the herringbone reconstruction lines of the Au(111) surface (Fig. 4.3b). Every chain is composed of two different alternating structures of distinct lengths (0.9 nm and 1.2 nm; Fig. 4.3a). We propose that the longer (shorter) structure corresponds to the two $CoCp_2$ (naphthalene) of a NBC molecule with the long axis of the two $CoCp_2$ units parallel to the surface.

To verify the above hypothesis, a scaled molecular model of NBC with the suggested structure (see below) is superimposed on the STM topograph in Fig. 4.3a. The agreement is relatively good. Indeed, the lateral extent of the model matches the structure in the topograph. The naphthalenes exhibit a length of 9 Å compared to the 7 Å of the calculated structure. The apparent height of around 1.7 Å (Fig. 4.3c) is comparable to similar planar molecules with π orbitals pointing out of the surface [288, 289]. The apparent height of $CoCp_2$ (1.4 Å) is slightly lower despite the Cp ring diameter of 4.4 Å. This apparent contradiction is not surprising as the measured apparent heights drastically depend on the overlap between the molecule's orbitals with that of the tip. The apparent height of the horizontal $CoCp_2$ is therefore considerably lower than the 3 – 4 Å observed for upright metallocene molecules [260, 261, 272]. The

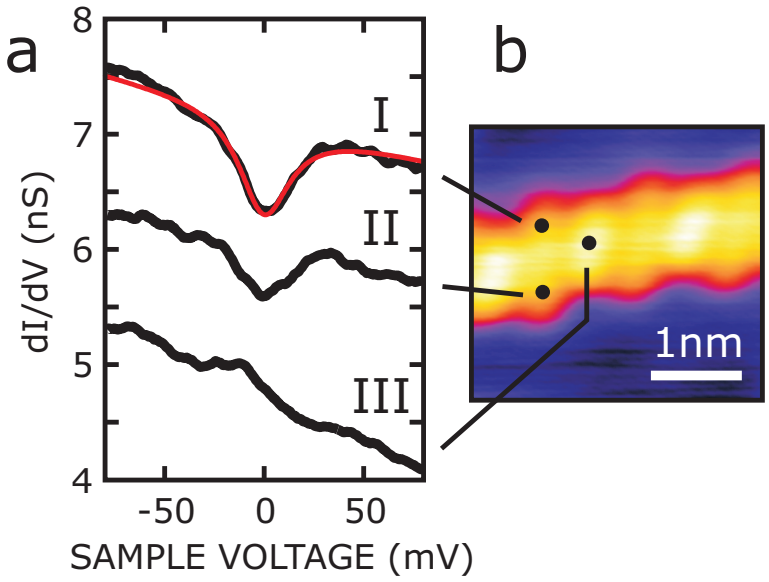

FIGURE 4.4: (a) dI/dV spectra of a biscobaltocene molecule on Au(111). The spectra were acquired over each $CoCp_2$ and over the naphthalene. The feedback loop was opened at V = −100 mV, I = 1 nA. The spectra are vertically shifted for clarity. A Fano fit of the resonance is shown as a red line. (b) STM topograph (I = 30 pA, V = 0.2 V) indicating the positions used for spectroscopy.

model used in Fig. 4.3a deviates from the structure inferred from X-ray diffraction data of bulk crystals [173, 286]. The twist angle, i. e. the angle between the naphthalene and the Cp planes, goes from ≈ 47° (bulk molecule) to ≈ 90° (model). This renders the naphthalene plane parallel to the long axes through the two Co atoms.

It was previously shown that single metallocenes can adsorb vertically and horizontally on metal surfaces, i. e. with the molecular axis perpendicular and parallel to the surface, respectively [260, 261]. Here, no vertically adsorbed $CoCp_2$ were observed and are actually not expected. Indeed, the two $CoCp_2$, which are connected to the 1 and 8 positions of the naphthalene, are so close that their molecular axes cannot be both perpendicular to the naphthalene plane.

In previous studies, scanning tunneling spectroscopy measurements on single metallocene adsorbed vertically on metallic substrates revealed spin-flip excitations or Kondo resonances [121, 262, 272]. The Kondo effect results from the interaction between a localized magnetic moment and the surrounding conduction electrons of a non-magnetic substrate [92, 96–98, 112].

In the present case, each cobaltocene unit of the NBC molecule should have one unpaired electron and hence a spin $S = 1/2$ [173]. The singly occupied molecular orbitals consists of d_{yz} cobalt orbitals, which are strongly hybridized with the orbitals of the ligand rings. However, in contrast to the earlier observations of the Kondo effect on metallocene molecules, the $CoCp_2$ are adsorbed horizontally. It therefore is not

clear a priori whether the electronic coupling of the $CoCp_2$ to the substrate is sufficient to give rise to a Kondo resonance.

Figure 4.4a shows typical differential-conductance spectra acquired over different positions above a NBC molecule within a molecular chain. These tip positions are marked in the STM topograph in Figure 4.4b. The spectra measured atop the expected horizontally-adsorbed cobaltocene positions (I,II) show a narrow dip near the Fermi energy. In contrast, the spectrum acquired over the naphthalene (III) does not exhibit any characteristic features in the measured voltage range. The narrow dip observed for the differential conductance over the $CoCp_2$ is fitted with a Fano line shape [96, 108, 112] (Fig. 4.4a). The Fano fit yields a Kondo temperature T_K of 190 K, a form factor q of 0.1, and energy shift of the Kondo resonance of 3.3 meV. Note that a similar Kondo temperature (T_K of 114 K) was observed for a Co-Ferrocene complex [121]. Considering the expected spin 1/2 of $CoCp_2$ and the good agreement between the Fano fit and the experimental differential conductance, the narrow dip is assumed to originate from the Kondo effect (further justifications below).

Interestingly, the amplitude of the differential-conductance spectrum acquired over the lower $CoCp_2$ unit (position II) is considerably smaller (approximately half the amplitude in Fig. 4.4a) than that acquired over the upper $CoCp_2$ unit (position I). The two $CoCp_2$ units of NBC therefore exhibit different resonances. This is not a singular case, rather different resonance amplitudes for the two $CoCp_2$ subunits were observed for most of the NBC molecules. It may reflect magnetic interaction between the two $CoCp_2$ units of a NBC molecule.

However, as the difference in the Kondo-resonance amplitude between the two $CoCp_2$ units varies from molecule to molecule, we suppose that it dominantly arises from different coupling to the Au(111) substrate. As the molecule is rather symmetric in the gas phase, we propose that different $CoCp_2-$surface couplings originate from different adsorption geometry of the two subunits [114, 290]. Indeed, the adsorption sites of the Co atoms within a NBC molecules should be different, as the distance between the two Co atoms (6.4 Å) imposed by the naphthalene linker is incommensurate with the Au(111) substrate. Furthermore, the distance between two Co atoms belonging to two neighboring NBC molecules may be such that it is also incommensurate with the Au(111) substrate. In that case, the $CoCp_2-$substrate coupling and henceforth the Kondo resonance of every $CoCp_2$ units is expected to vary, in agreement with the experimental evidence (see Appendix B for additional spectra). Note that, for simplicity, only differences in the Co adsorption site are discussed. However, the molecular orbital responsible for the Kondo effect most probably extends over the entire molecule (Ref. 272) such that the position of each atom of the $CoCp_2$ unit relative to the Au(111) substrate can be of importance.

We have seen that the amplitude of the dips in the differential conductance differs for every $CoCp_2$ unit. This difference is tentatively attributed to different adsorption sites of the $CoCp_2$ units imposed by (i) the naphthalene and (ii) the distance between neighboring NBC molecules within a molecular chain. Furthermore, we recall that without a change of the gas-phase structure of the NBC molecule, the naphthalene

group and the two $CoCp_2$ units would not all together be able to adsorb flat onto Au(111). These findings suggest that an additional naphthalene-bridged $CoCp_2$ unit may reduce the flexibility of the molecule rendering the issue of commensurate distances even more complex. May the new molecule adsorb in such a way that, any of the $CoCp_2$ unit exhibits a Kondo resonance?

Naphthalene bridged triscobaltocene

The molecular structure of NTC was determined by gas-phase DFT calculations (Fig. 4.5a). Similar to the NBC molecule, the three $CoCp_2$ units of NTC are arranged in an head-to-head stacking. However, the head-to-head Cp rings are not exactly parallel but tilted by approximately $20 - 30°$. Therefore the three $CoCp_2$ units are not parallel but form an arch (Fig. 4.5a). The two naphthalene units are parallel but titled by $\approx 40°$ to the plane defined by the Co atoms. This leads to an asymmetry of the NTC molecule. We emphasize that, in contrast to NBC, the two naphthalene groups of NTC cannot be parallel to the $CoCp_2$ units due to geometric constraints. Indeed, the limited length of the middle $CoCp_2$ unit prevents a planar arrangement of the two naphthalene units. Based on this consideration, we expect the adsorption of NTC on Au(111) to be different from the case of NBC on Au(111).

Since long molecules are generally incompatible with sublimation, we employed the soft-landing deposition capability of ESI (see methods) to deposit NTC onto Au(111). Prior to deposition, the NTC ion beam was analyzed by an in-line quadrupole mass spectrometer. Figure 4.5b shows a typical mass spectrum. A single well-pronounced peak is observed corresponding to intact, triply charged NTC molecules (271 u/e). This m/z value was used to deposit the mass-selected NTC molecules on the surface.

A typical large-scale STM topograph is shown in Figure 4.5c. The herringbone reconstruction of the clean Au(111) surface is clearly discernible as bright lines on a darker background. Several isolated adsorbates with a similar, elongated shape are observed. These adsorbates are assigned to intact NTC molecules. Despite gentle tunneling parameters ($I = 10$ pA, $V = -0.5$ V) used for imaging, two molecules were subject to tip-induced displacements (e. g. molecule encircled in Fig. 4.5c). Such tip-induced displacements were not observed for NBC on Au(111) with similar tunneling parameters and indicate a weaker coupling between NTC and Au(111). As discussed below, this has consequences for the Kondo effect.

Figure 4.5d shows a zoomed STM topograph of the molecular asorbate. The molecular structure of NTC obtained from gas-phase DTF calculations (Fig. 4.5a) is scaled and superimposed on the STM topograph (Fig. 4.5d). The agreement in shape and lateral dimensions is rather good. Indeed, the adsorbate has a length (width) of 2.4 nm (1.7 nm) relative to 1.8 nm (0.9 nm) of the molecular model. Interestingly, the line profile along the longitudinal axis of the molecule exhibits two peaks (Fig. 4.5e). Their lateral positions match the inferred positions of the naphthalene groups pointing upwards into vacuum. In other words, the naphthalene groups are standing upright (side

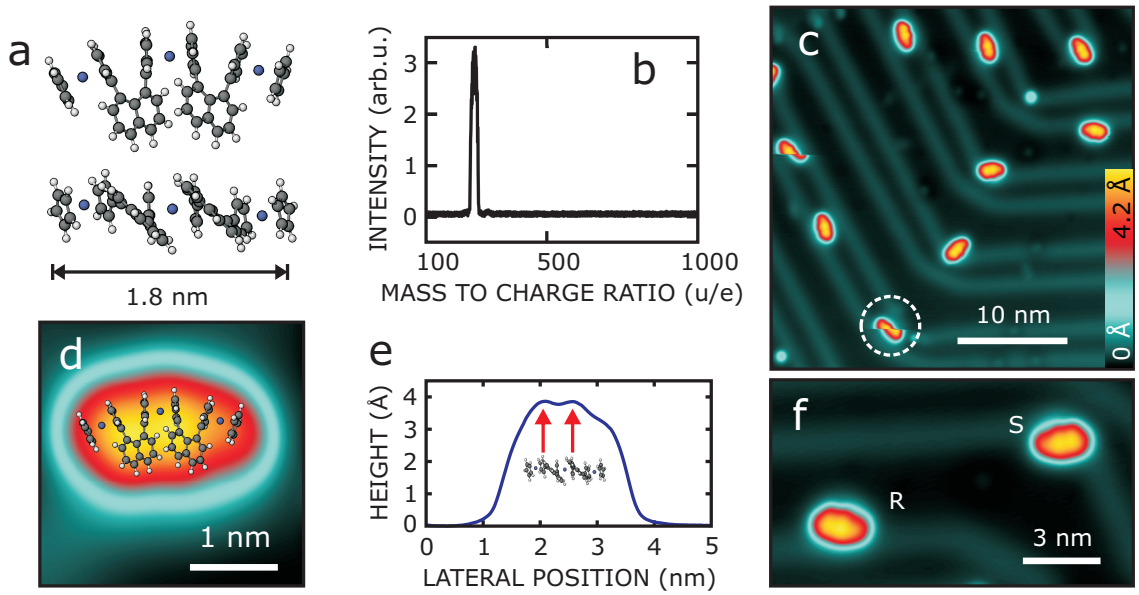

Figure 4.5: (a) Top and side views of the calculated gas-phase structure of NTC. (b) Typical mass spectrum of electrosprayed NTC ions. (c) STM topograph of NTC on Au(111) exhibiting several similar, longish adsorbates. Two single molecules moved during scanning (e. g. encircled molecule). (d) STM topograph of a single NTC molecule on Au(111) with a superimposed scaled molecular model. (e) Height profile of NTC on Au(111) along the long axis of a NTC molecule. (f) STM topograph of two molecules illustrating the chirality of NTC on the surface. Tunneling parameters: $I = 10$ pA, $V = -0.5$ V.

view presented in Fig. 4.5a). The upper part of the naphthalene groups leads to peaks in the line profile.

The line profile reflects the asymmetry of the molecular geometry which was discussed above. Actually, the direction of the naphthalenes rotation which respect to the curvature of the $CoCp_2$ units induces a chirality. Indeed, different enantiomers are obtained with the tilted naphthalenes pointing to the upper left (S) or right (R) side of the molecular model (Fig. 4.5a, side view). Both mirror symmetric enantiomers can be distinguished in the STM topograph (Fig. 4.5f). As expected, R and S enantiomers may not be simply interconverted by on-surface rotation.

Each $CoCp_2$ unit of NTC should bear a spin 1/2. However, in contrast to the STS measurements on NBC/Au(111) we could not observe any zero bias feature related to the Kondo effect on NTC/Au(111). We speculate that the absence of a Kondo resonance is due to a limited coupling between the $CoCp_2$ units and the Au(111) substrate. Presumably, the adsorption geometry adopted by the molecule is such that none of the $CoCp_2$ adsorption sites are compatible with a Kondo resonance. Additionally, it is conceivable that the geometrical constraints imposed by the naphthalene groups lead to different Co−Au(111) distances of the $CoCp_2$ units. Therefore, we have a system possessing magnetic centers, but due to limited coupling to the substrate, show no Kondo

resonance. This calls for a different strategy to interconnect the magnetic centers, e. g. by using linkers that enable an upright orientation of the $CoCp_2$ units.

Benzene bridged triscobaltocene

Figure 4.6a shows the molecular structure of the benzene bridged triscobaltocene BTC. The complex consists of three $CoCp_2$ units linked to a benzene ring at positions 1, 3 and 5. All three $CoCp_2$ units extrude in the same direction, perpendicular to the benzene ring (Fig. 4.6a). A very similar molecule was recently investigated [272] (Chap. 3), namely 1,3,5-tris-(η^6-borabenzene-η^5-cyclopentadienylcobalt) benzene (TCBB), composed of three η^6-borabenzene-η^5-cyclopentadienylcobalt (CBB) instead of three $CoCp_2$ units for BTC. In other words, one of the two CBB ring has an extra boron atom compared to $CoCp_2$. TCBB molecules were deposited on Au(111) and Cu(111). STM topographs revealed intact molecules with the CBB units oriented vertically. The benzene and borabenzene rings of TCBB face towards the surface. At 5 K, Kondo resonances were observed, but only when the TCBB complex is adsorbed on Cu(111) (not on Au(111)). As the coupling between TCBB and Au(111) is too low for the observation of a Kondo resonance, we speculate that it is also too low for BTC on Au(111) and therefore investigate BTC molecules deposited on Cu(111).

Similar to NTC molecules, the BTC molecules were deposited on Cu(111) using ESI (see methods and Appendix B). Figure 4.6b shows a STM topograph, upon deposition of BTC on Cu(111), exhibiting two adsorbates. Three lobes are discernible for each adsorbate, which have an overall three-fold symmetry (Fig. 4.6b). A scaled molecular model, resulting from gas-phase DFT calculations, is superimposed on the STM topograph (Fig. 4.6b). The good agreement of symmetry and lateral dimensions indicates that the $CoCp_2$ units are standing upright. This is corroborated by the larger apparent heights of the BTC lobes (between 4.4 and 4.7 Å) compared to that of the horizontally adsorbed $CoCp_2$ units of NBC ($\approx$ 1.5 Å (Fig. 4.3c)). The benzene ring is presumably in contact with the substrate as it was the case for TCBB on Cu(111) (Ref. 272). In contrast to TCBB on Cu(111) where only isolated molecules were imaged, Figure 4.6b shows two neighboring BTC molecules on Cu(111). It indicates that the diffusion of the BTC molecules was possible at room temperature, in turn suggesting a low molecule−substrate coupling.

No Kondo resonance was observed in scanning tunneling spectra acquired at different positions over BTC/Cu(111). At first glance, this is surprising, as TCBB, which is very similar to BTC, exhibits two Kondo resonances [272]. The difference between the two systems may again be different molecule−substrate couplings. We propose that the insufficient coupling of the $CoCp_2$ units within BTC on Cu(111) for the observation of a Kondo resonance originates from a tilt of the $CoCp_2$ units relative to the surface. Indeed, this tilt determines to which extent the π orbitals of the Cp rings overlap with that of the substrate.

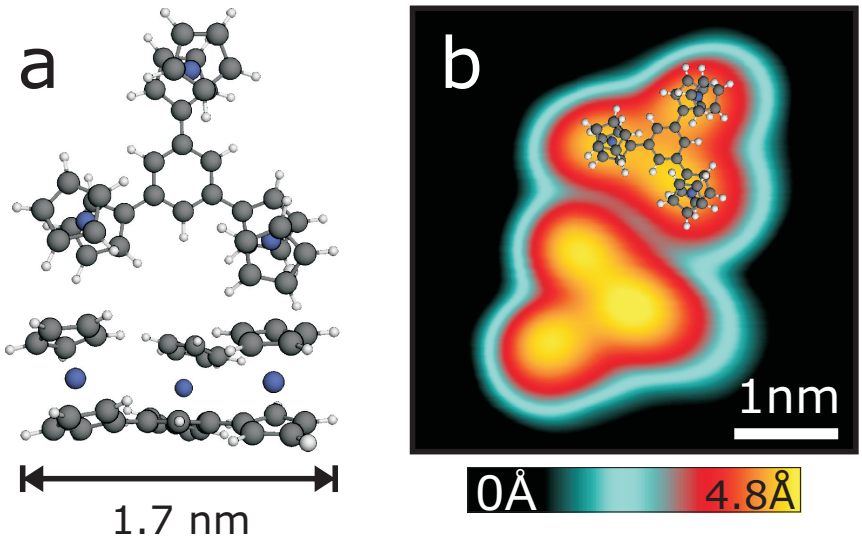

Figure 4.6: (a) Top and side views of the calculated gas-phase structure of BTC. (b) STM topograph ($I = 20$ pA, $V = 0.1$ V) of two BTC molecules on Cu(111) with a superimposed scaled molecular model.

Standing metallocene molecules adsorbed on metal surfaces are usually imaged as ring-like protrusions with a depression corresponding to the center of the upper Cp ring [121, 260–262, 272]. By analyzing the depressions' lateral position and with the help of DFT calculations, tilt angles of up to 9° were found. Interestingly, in the present case, the Cp rings of BTC on Cu(111) do not exhibit any depression in their center (Fig. 4.6b), suggesting a large tilt angle. From the absence of a depression, we infer a tilt angle exceeding 10°. The large tilt likely decouples the $CoCp_2$ units from the Cu(111) substrate, which in turn prevent a Kondo effect. The tilt may originate from an attractive interaction between the $CoCp_2$ units (metallocene units have a tendency to form dense layer [260, 261, 291]). However, in the present case, the benzene ring of the BTC molecules imposes a fixed distance between the $CoCp_2$ units at the surface, while no particular distance between the $CoCp_2$ units is expected in the upper part of the molecule.

Apparently the boron within TCBB does not only tune the electronic properties of the molecules but also adds rigidity to the molecule. The increased rigidity limits the tilting of the $CoCp_2$ units allowing the observation of the Kondo effect on TCBB/Cu(111). Considering the outcome of the investigation of NBC and NTC molecules on Au(111) and BTC molecules on Cu(111), it appears that the magnetic properties of interconnected magnetic centers on metal surfaces depend on (i) the coupling between the magnetic units, (ii) the distance between the units, i. e. commensurate with the underlying substrate lattice and (iii) the rigidity and overall geometry of the molecule. Such considerations should be taken into account for the development of new strategies to interconnect magnetic centers.

4.3 Conclusions

In conclusion, we demonstrated the deposition of three molecules, composed of interconnected $CoCp_2$ magnetic centers, on metallic substrates. Surprisingly, a dip in the differential conductance, assumed to originate from the Kondo effect, is observed for one complex only (NBC). Furthermore, the resonance amplitude strongly varies between $CoCp_2$ units. The different Kondo-resonance amplitudes of NBC on Au(111), and the absence of a Kondo resonance for NTC and BTC on Au(111) and Cu(111), respectively, are attributed to particular coupling of the $CoCp_2$ units to the substrate. By comparing the different cases, factors influencing the coupling are identified: (i) the linker imposes a distance between the magnetic centers, which may not be commensurate with the underlying substrate lattice; (ii) particular structures of the investigated molecule are geometrically hindered by the linker, in turn impacting the adsorption geometry of the magnetic units; (iii) the molecule will adopt a conformation dictated by the interaction between the magnetic units (and the substrate) compatible with the constraints (notably the bond rigidity) imposed by the linker. For future molecular-spintronics applications, it appears fundamental to take these factors into account in the design of new molecules composed of interconnected magnetic centers.

5

Surface cis effect: Influence of an Axial Ligand on Molecular Self-Assembly

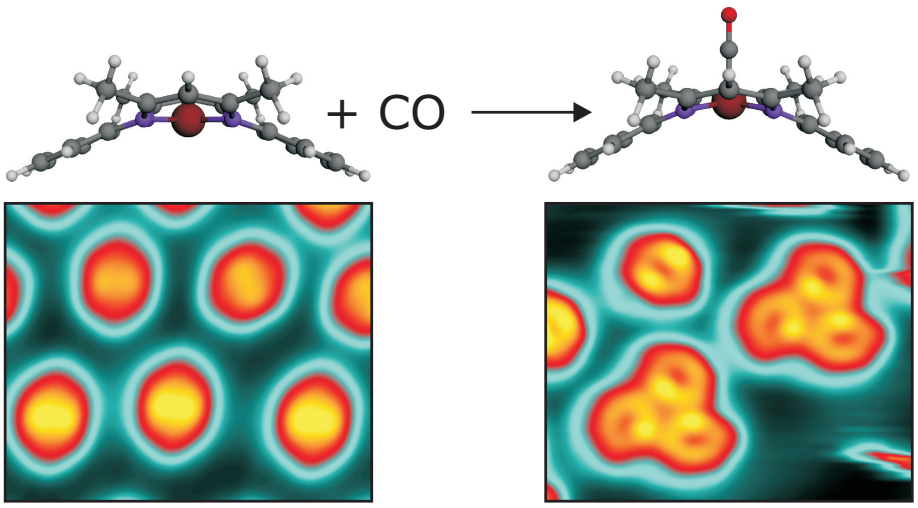

The results presented in this chapter were published in 2016 in the Journal of the American Chemical Society [292]. The coauthers are Thiruvancheril G. Gopakumar, Bettina Schwager, Felix Tuczek, Roberto Robles, Nicolás Lorente, and Richardt Berndt. In this publication, STM data on NiTMTAA measured by Thiruvancheril G. Gopakumar and STM data on FeTMTAA measured during the work for my diploma thesis [293] are compared. I performed additional STS measurements, gas-phase DFT calculations and further data analysis to show the surface *cis* effect, which is presented in the following.

5.1 Introduction

The properties of metal-organic complexes may be controlled through the number and type of ligands attached to the metal center. This concept from solution chemistry [294–298] has been extended to complexes adsorbed on metal surfaces. Both electronic and magnetic properties have been shown to respond to the addition or removal of a ligand [18, 141, 142, 192, 299–309].

Little is known about the influence of axial ligands on intermolecular interactions at surfaces. For planar metal complexes on surfaces, the ligands naturally occupy the axial position on the metal atom of the complex, conferring the metal atom with an octahedral-like ligand field, which changes the otherwise square-planar ligand field with consequences regarding the electronic and magnetic properties of the complex. Phthalocyanines, porphyrins and similar molecules belong to this class of metal-organic complexes with promise for ligand-induced modifications [58, 60, 310–312].

The *trans* effect in coordination chemistry is the weakening of a ligand on the metal center by the attachment of an additional ligand at a *trans* position. A closely related surface *trans* effect has recently been reported from NO bonding to metal tetraphenyl porphyrins on Ag(111) [141]. An overview of the surface *trans* effect and the closely related surface spin *trans* effect is available in a recent review [60]. As to intermolecular interactions, coadsorption of NO and largish molecules [313–318] has been reported to affect the molecular arrangements on a surface. In these cases, the transition-metal complex and the second species was coadsorbed side-by-side on the metal substrate and did not bind to the metal center as an additional ligand.

Here, we report on the formation of supramolecular bonds on a surface induced by the addition of an axial ligand to the metal center of a complex. We reveal this effect using CO ligands on Fe-tetramethyl-tetraazaannulene (FeTMTAA, Fig. 5.1a,b) on Au(111). While pristine FeTMTAA molecules on Au maximize their mutual distances at low coverages, the attachment of CO leads to a drastic rearrangement. CO causes the molecules to aggregate into ordered clusters. We discuss this striking observation in terms of the structure of the molecule, electrostatic intermolecular interactions and effect of CO on the charge transfer between FeTMTAA and the substrate. Moreover, we compare the results with equivalent measurements on Ni-tetramethyl-tetraazaannulene (NiTMTAA) [319] and DFT calculations. It turns out that CO attaches axially to

FeTMTAA, which lies flat on the substrate. As a result the interaction of the complex with its neighbors is changed from repulsive to attractive, which may be viewed as a surface *cis* effect.

5.2 Methodology

Experiment

Experiments were performed with a home-built STM operated in ultrahigh vacuum (UHV) at 5 K and 11 K. FeTMTAA was synthesized according to Ref. [320] and deposited onto clean Au(111) surfaces at room temperature by sublimation from a Ta crucible. Prior to sublimation, the material was repeatedly degassed close to its sublimation temperature of $\approx 200^\circ$ C in UHV. Exposure to CO was performed at 300 K and a CO pressure of $\approx 4 \times 10^{-5}$ mbar for 30 – 40 min. Prepared samples were transferred to the cold STM. Tips were electrochemically etched from tungsten wire and further prepared in situ by indentation into the substrate. A sinusoidal modulation (10 $\mathrm{mV_{rms}}$, 7 kHz) was added to the sample voltage V to record spectra of the differential conductance.

Theory

We applied DFT as implemented in the VASP code [321] using the generalized gradient approximation proposed by Perdew, Burke, and Ernzerhof (PBE) [166] to treat electronic exchange and correlation. Dispersion-corrections are included through the scheme proposed by Tkatchenko and Scheffler [322]. We have used a plane wave basis set and the projected augmented wave (PAW) method [323] implemented in VASP with an energy cutoff of 280 eV. The surface was represented by a five-layer slab and in all calculations we allowed the relaxation of the substrate atoms in the two topmost metal layers as well as all the atoms of the adsorbates. The substrate atoms in the three bottom layers were kept fixed to their bulk equilibrium positions. All geometry optimizations were carried out until the forces on mobile atoms were smaller than 0.02 eV/Å. The molecules were arranged in a periodic pattern formed by lozenges of 25 Au atoms following the ideal surface of Au(111). The k-point sampling corresponds to a Monkhorst and Pack mesh of $3 \times 3 \times 1$. DFT is known to underestimate the exchange splitting of localized orbitals, leading to an underestimation of magnetic moments. In order to correct for this, we have included an intra-atomic correlation correction $U - J = 3$ eV, where U corresponds to the Coulomb interaction and J to the exchange coupling, using the scheme by Dudarev *et al.* [324].

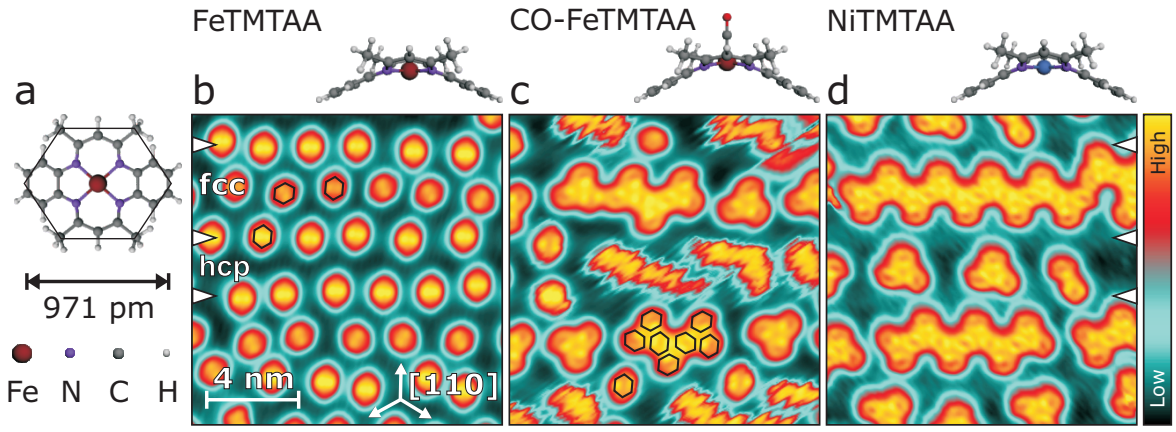

FIGURE 5.1: (a) Top view of the calculated gas-phase structure of FeTMTAA. Dark red, violet, dark gray, and light gray spheres indicate Fe, N, C, and H atoms, respectively. The model resembles an elongated hexagon (line), which is used to indicate the molecules and their orientations in STM images. (b) STM topograph ($I = 50$ pA, $V = 0.1$ V) of 0.2 ML of FeTMTAA on Au(111) along with a side view of the gas-phase structure of FeTMTAA. (c) The same coverage of FeTMTAA imaged after exposure to CO. $I = 50$ pA, $V = 0.2$ V. A side view of the structure of CO-FeTMTAA is also shown (light red indicating O). The molecular pattern has drastically changed with many molecules assembled into trimers and chains. Monomers in hcp areas appear fuzzy because they move during scanning. At low voltages, many monomers are more stable and are identified as pristine FeTMTAA molecules. (d) STM topograph of 0.2 ML of NiTMTAA ($I = 100$ pA, $V = 0.5$ V). The pattern is closely related to that of CO-FeTMTAA. A side view of the calculated structure is shown for each molecule.

5.3 Results

FeTMTAA adsorption on Au(111)

The macrocyclic ligand of FeTMTAA exhibits a pronounced saddle shape (Fig. 5.1a,b) owing to the steric interaction of the four methyl groups with the phenyl rings [325]. Figure 5.1b shows a STM topograph of 0.2 monolayer[1] (ML) FeTMTAA on Au(111). Single molecules are clearly resolved as oval protrusions. Some examples are indicated by elongated hexagons in Figure 5.1. The molecules form a fairly regular hexagonal pattern with an intermolecular distance of ≈ 1.9 nm. Molecules are aligned with their long axis along one of the three compact directions of Au(111). The reconstruction of the Au substrate causes small height variations [326, 327]. In particular, the transition region between fcc and hcp stacked areas of Au is elevated by $\sim 15 \pm 4$ pm and this height difference is also found on the molecules (~ 20 pm in our data).

[1]We define 1 ML as a coverage of 1 molecule per nm^2, the most dense structure we observed (see Appendix C).

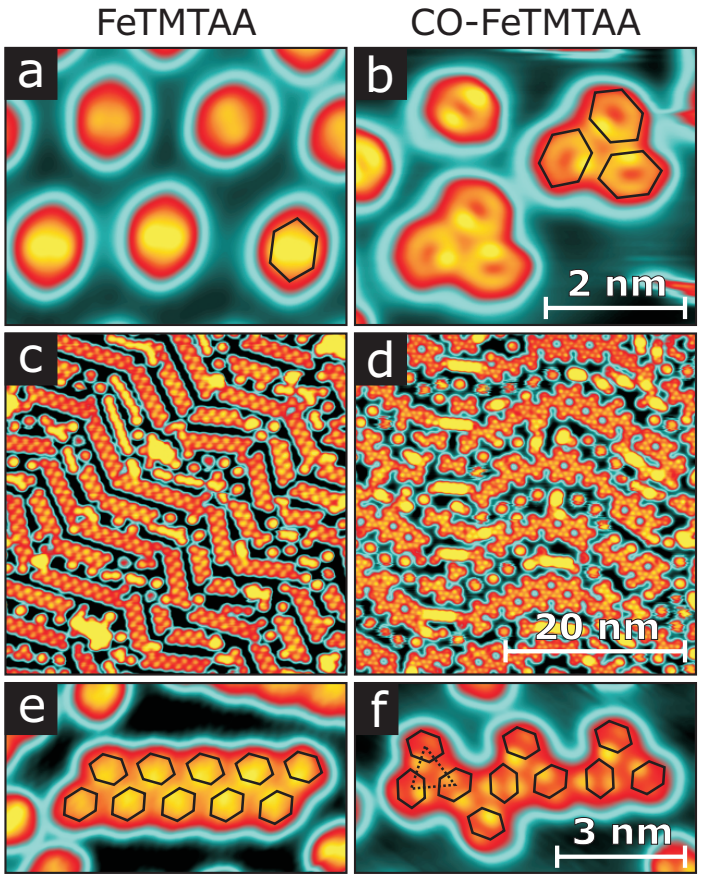

Figure 5.2: STM topographs of FeTMTAA and CO-FeTMTAA on Au(111). Detailed images (a,b) of 0.2 ML and (c,d) 0.5 ML. (e,f) Detailed images of chains of FeTMTAA and CO-FeTMTAA at 0.5 ML coverage. The color palette from Figure 5.1 is used, with some contrast enhancement in panels c and d. Tunneling parameters: $I = 50$ pA and $V = 0.1, 0.2, -0.25, -0.5, -0.06$, and -0.5 V in (panels a–f), respectively.

Intramolecular contrast is demonstrated in Figure 5.2a, which reveals that the molecules appear higher along the short axis. The STM image therefore indicates that FeTMTAA adsorbs with its phenyl rings pointing toward the substrate. While this geometric interpretation of the image contrast is a simplification, it is important to note that the STM image of FeTMTAA varies little over a range of sample voltages. This observation is consistent with spectra of the differential conductance ($\mathrm{d}I/\mathrm{d}V$) acquired above the center of FeTMTAA, which do not exhibit specific molecular states over a bias range of 3 V (Fig. 5.3).

Our calculations corroborate the above findings. An energy minimum was found for the molecule horizontally adsorbed on the surface with the methyl groups pointing into vacuum. This enables a strong bonding of the Fe center to the substrate. There is a weak preference for placing the Fe atom on top of a surface Au atom, with a

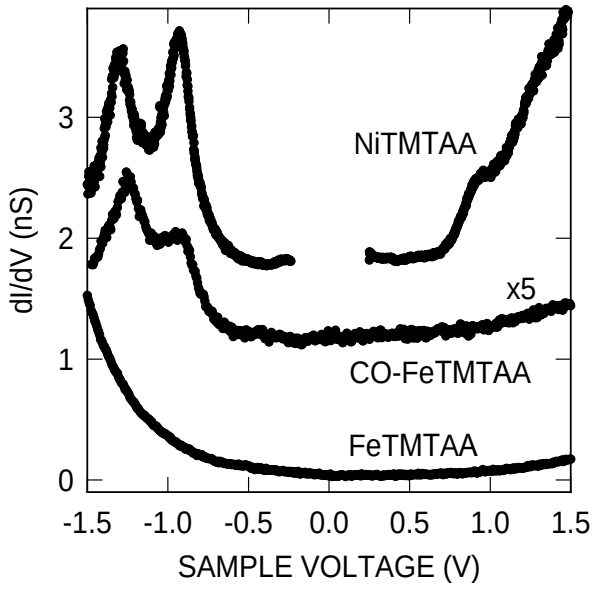

FIGURE 5.3: dI/dV spectra acquired above the centers of FeTMTAA, CO-FeTMTAA, and NiTMTAA molecules recorded at coverages of 0.8, 0.5, and 0.5 ML, respectively. Current feedback was opened at $V = 1.5$ V, $I = 100$ pA and $V = -1.5$ V, $I = 200$ pA for FeTMTAA and CO-FeTMTAA, respectively. The NiTMTAA data were recorded at a constant current of $I = 1$ nA and converted to an approximate constant-height spectrum using the procedure of Ref. [81]. Because the tip-sample distance is unknown, the calculated conductance is arbitrarily scaled for NiTMTAA. The CO-FeTMTAA data were multiplied by a factor of 5. The CO-FeTMTAA and NiTMTAA spectra have been shifted by 1 and 1.5 nS, respectively.

chemisorption energy of -2.35 eV (-54.2 kcal/mol). Adsorption at the fcc hollow and at bridge sites are less favorable by 80 and 800 meV, respectively. The small energy difference between the fcc and top adsorption sites suggests that molecules may be found to occupy different sites. The van der Waals interaction leads to a considerably flattening of the adsorbed molecule reducing the saddle-shape of the gas-phase molecule as can be seen in the calculated geometrical structure of Figure 5.4.

The optimized geometry of the molecule is actually affected by the molecular magnetic moment. On the top site, we find that the FeTMTAA molecule presents two possible spin values, high-spin 4.3 μ_B and low-spin 2.6 μ_B, with an energy difference of 23 meV. In the high-spin configuration the Fe ion is 2.7 Å away from the Au(111) surface, while the entire molecule is lifted by approximately 0.1 Å for the low-spin configuration. The hollow-site configuration, which is very close in energy (20 meV higher than the top-site configuration), pushes the Fe ion further to 2.9 Å. The charge transfer involving the Fe ion confers the molecule with its main properties. Indeed, this is corroborated by a more profound inspection of the STM images of FeTMTAA that reveals a central protrusion.

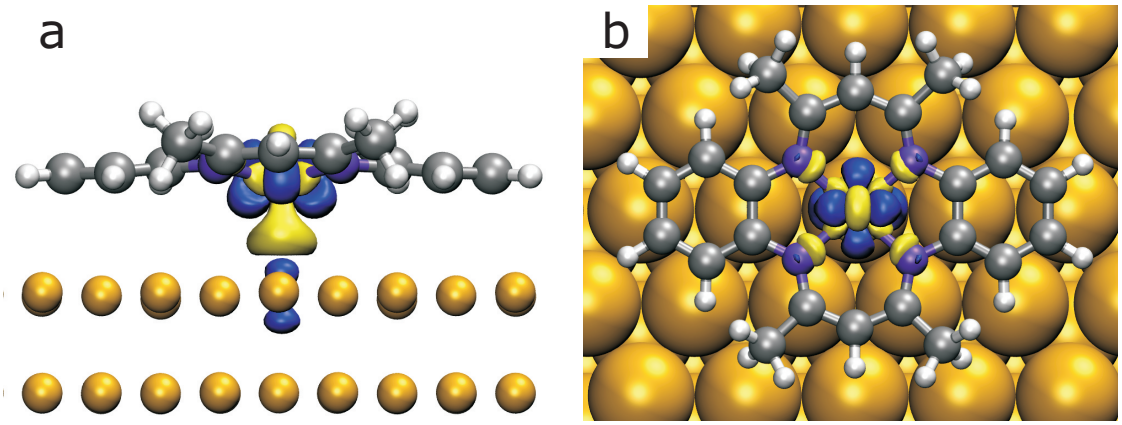

Figure 5.4: Electronic density induced by the molecule−substrate interaction. The isosurfaces correspond to a value of ± 0.0035 e/Å. The positive (negative) value indicates excess (defect) of induced electrons plotted in yellow (blue). Goldish, light gray, dark gray, and violet spheres indicate Au, H, C, and N atoms, respectively. The interaction between the molecule and the gold surface (after due atomic relaxation) leads to a transfer of approximately 0.14 electrons from the molecule to the substrate following our Bader charge analysis.

A Bader charge analysis of the adsorbed system reveals a net electron donation from the molecule to the substrate. The Fe atom loses 0.2 electrons whereas the N atoms acquire 0.08 electrons. The C atoms remain largely unaffected. Figure 5.4 displays the differences of electronic density due to the formation of the molecule−substrate bond. This induced charge is computed using the expression:

$$\delta\rho = \rho_{\text{all}} - \rho_{\text{molecule}} - \rho_{\text{substrate}}, \tag{5.1}$$

where ρ_{all} is the density of electrons of the full system, ρ_{molecule} is the density of electrons for the molecule in exactly the same geometry as the adsorbed molecule and $\rho_{\text{substrate}}$ is the corresponding density of the surface also with the adsorption geometry.

In the experiments, most of the isolated FeTMTAA molecules could only be stably imaged at low bias $|V| < 0.2$ V. When the voltage exceeded this value the molecules moved and the tunneling current became unstable. This fact agrees with the picture emerging from the calculations. The adsorbed molecules have acquired a positive charge and therefore interact with the strong and inhomogeneous electrical field under the STM tip. The charge analysis together with the computed energy landscape of the molecule on the surface provide a distinct picture of the molecular arrangement on the surface. Namely, the positive charge along with the corresponding image charge lead to repulsion via dipole−dipole interactions on a potential energy surface with little corrugation. The result, in equilibrium, is an array of equidistant single molecules.

A projection of the density of states (PDOS) on the d orbitals of the Fe ion provides further information on the electronic and magnetic properties of the molecule.

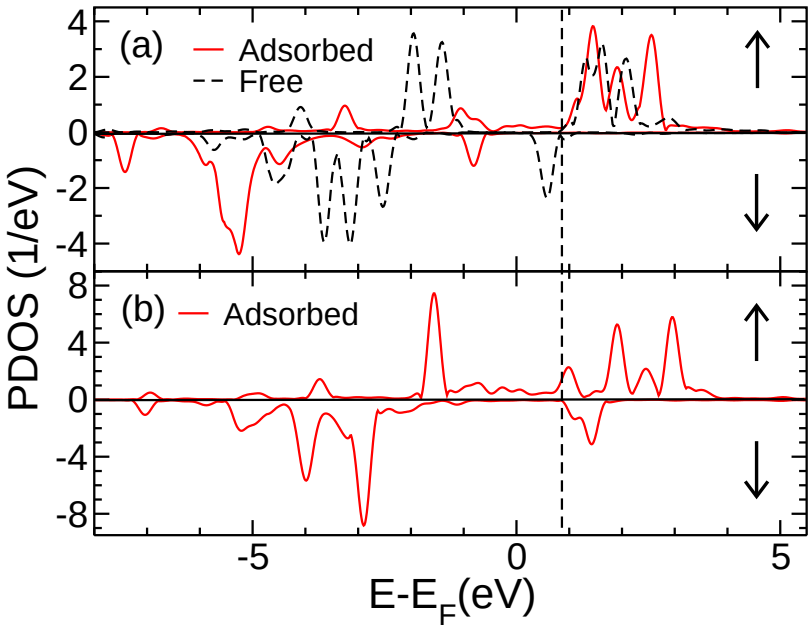

FIGURE 5.5: Density of states projected (PDOS) on the Fe d-manifold for (a) the high-spin configuration (4.3 μ_B) and (b) the low-spin one (2.6 μ_B). The black curve in panel a corresponds to the free-molecule configuration with a magnetic moment of 2.0 μ_B ($S = 1$). The adsorbed high-spin configuration (red in panel a) corresponds to a full d-shell for the majority spin ($\downarrow$) and approximately only one electron in the minority spin ($\uparrow$) leading to four unpaired spins or a total spin $S = 2$. This is in contrast with the free case (black) that displays two electrons from the minority spin but only four electrons for the majority spin, leading to a total spin $S = 1$. The low-spin configuration is closer to the free-molecule configuration although it displays some energy shifts similar to the high-spin one leading to a smaller occupation of the minority spin. As a consequence the low-spin configuration approximately corresponds to a total spin $S = 1$.

Figure 5.5 shows the PDOS for the free molecule as well as for the high- and low-spin configurations of the adsorbed molecule. Compared with the PDOS of the free molecule (black and dashed) the minority-spin components indeed carry less charge for the adsorbed species, in agreement with the donation of charge from the molecule. For the low-spin case, Figure 5.5, we see that charge transfer mainly affects the minority spin, reducing the magnetic moment of the molecule. Nevertheless, the low-spin molecule approximately maintains the magnetic moment of the free molecule, corresponding to a total spin $S = 1$. In the high-spin case, the donation from the minority channel is partially compensated from back-donation into the majority-spin d-states, which explains the larger magnetic moment of this configuration. The high-spin molecule rather corresponds to a total spin $S = 2$.

The electronic systems described above may be described as approximate d^6 configurations of the Fe ion, where only the actual filling of the different d-shells changes. In the case of the free molecule, the Fe ion is in a d^6 configuration, leading to $S = 1$ and

to an Fe(II) valence. Both high- and low-spin states involve a small reduction of the d-shell occupation, well below the transfer of one electron, and hence they remain in an approximate d^6 configuration corresponding to an Fe(II) oxidation state. The spin configurations that we find ($S = 2$ and $S = 1$) are indeed compatible with the Fe(II) oxidation state [328].

Adsorption of CO on FeTMTAA on Au(111)

FeTMTAA-covered surfaces were exposed to CO at ambient temperature. Because CO desorbs from gold below ambient temperature [329] no CO remains on the Au substrate. Subsequent imaging at low temperature revealed drastic changes. Figure 5.1c was recorded at 0.2 ML coverage and may be directly compared with Figure 5.1b with the same coverage but without CO. FeTMTAA molecules in fcc areas are no longer isolated but have aggregated into small supramolecular assemblies, the main building block being a chiral trimer [288, 330–332]. In addition, the intramolecular contrast is modified (Fig. 5.2b). The CO-exposed molecules (denoted CO-FeTMTAA) exhibit a depression at their center. The images of CO-FeTMTAA are voltage dependent in contrast to those of FeTMTAA. The conductance spectrum acquired at the center of the molecules reveals states at -0.9 and -1.3 V, which are close to those of NiTMTAA (Fig. 5.3).

The observed CO-induced changes in STM images and $\mathrm{d}I/\mathrm{d}V$ spectra strongly suggest that CO is binding to FeTMTAA on Au(111). Below, we argue that CO attaches axially to the Fe center on the vacuum (rather than substrate) side of the molecule. The additional ligand apparently modifies the intermolecular interaction from repulsive in the FeTMTAA case to attractive for CO-FeTMTAA.

The influence of the CO ligand on the intermolecular interactions is also obvious on a larger scale and at higher coverages. Figures 5.2c–f present images of FeTMTAA and CO-FeTMTAA, each at 0.5 ML coverage. The favorable fcc areas are almost entirely covered with molecules. Pristine FeTMTAA forms double rows with neighboring molecules rotated by 60° with respect to each other (Fig. 5.2c,e). CO-FeTMTAA, by contrast, forms zigzag chains (Fig. 5.2d,f), whose building blocks again are trimers (Fig. 5.2b). The zigzag chains are in fact porous, honeycomb-like networks [333], which closely resemble the pattern observed from NiTMTAA [319] (Fig. 5.1d).

Our DFT calculations for CO-FeTMTAA in gas phase led to an optimized geometry where CO binds axially to FeTMTAA (Fig. 5.1c). CO-FeTMTAA being a closed-shell system, this result is reproduced in calculations for CO-FeTMTAA on the inert Au(111) surface. Moreover, an axial coordination of CO to FeTMTAA in crystals was previously found with X-ray diffraction [334]. A slight displacement of the Fe atom from the plane of the N atoms leads to nonequivalent axial ligand sites and a preference for coordination at the side of the phenyl benzenoid rings [325, 335]. Because of the orientation of FeTMTAA on Au(111), however, this site is located at the substrate side of the molecule, which is not favorable energetically due to the steric hindrance between surface and molecule.

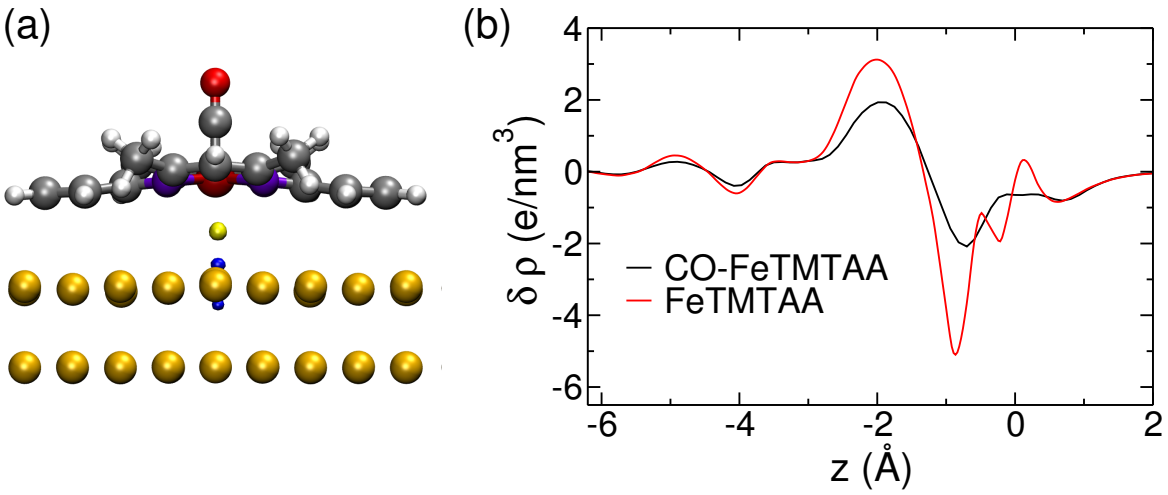

FIGURE 5.6: (a) Induced density between a CO-FeTMTAA molecule and the Au(111) substrate. Goldish, light gray, dark gray, violet, dark red and light red spheres indicate Au, H, C, N, Fe, and O atoms, respectively. The isosurfaces are taken for the same values as in Figure 5.4, showing the large difference in charge transfer between molecule and substrate depending on adding an extra carbon monoxide molecule. (b) Planar average of the induced charge for the CO-FeTMTAA complex (black) and the FeTMTAA molecule (red). The Fe atom of the molecule is the origin of coordinates. Positive values of z correspond to the vacuum side. This graph reveals the surface dipole of the rearranged charges due to the interaction between molecular complex and substrate. At the isovalue of panel a, the planar average shows zero induced density for the CO-FeTMTAA molecule, in agreement with the very localized distribution of panel a.

Carbon monoxide easily binds to the free FeTMTAA molecule. As for the heme group of porphyrin molecules, the adsorption of CO is made possible by a charge transfer into the 2π-orbital of carbon monoxide. The adsorption of CO on FeTMTAA molecules is qualitatively similar to the adsorption of CO on porphyrins although the amount of charge transfer to the CO molecule is larger signaling more chemical activity from the FeTMTAA molecule than from porphyrins [336].

When the combined CO-FeTMTAA molecule is adsorbed on Au(111) no charge transfer from Fe to the Au substrate takes place, in contrast to the case of pristine FeTMTAA. This is clearly seen in the almost identical Bader charge distributions before and after CO-FeTMTAA adsorption on Au(111). Figure 5.6a shows the value of the induced electron density (Eq. 5.1) for the same isovalue as Figure 5.4. The charge is very reduced, showing the small transfer of charge between molecular complex and surface. Figure 5.6b is the induced charge averaged over planes parallel to the surface in the unit cell of the calculation. The Fe atom loses up to 5 electrons per nm^3 due to the adsorption of FeTMTAA on Au (111), while this value is reduced to 2 electrons per nm^3 when CO-FeTMTAA is considered. This leads to a smaller overall induced dipole when CO is adsorbed on FeTMTAA. From these results, we

conclude that while FeTMTAA becomes positively charged on the Au(111) surface, CO-FeTMTAA is largely neutral. This is further corroborated by the experimental observation that isolated CO-FeTMTAA molecules on the surface were stable at elevated sample voltages. Otherwise, the electrical field from the tip would have likely influenced the molecule.

The magnetic moment of the new system is zero. This is due to the rearrangement of the *d*-shell of the Fe(II) ion. Indeed, the valency Fe(II) is compatible [328] with molecular spins of 0, 1, and 2, as we have found here.

Adsorption to the fcc site is 110 meV more stable than the bridge configuration and 1.7 eV more stable than the top site adsorption. The adsorption of CO-FeTMTAA is qualitatively different from the case of FeTMTAA. This is due to the partial passivation of the Fe center when CO is directly attached to it. The adsorption of CO-FeTMTAA is directed by the interaction of the nitrogen atoms with the substrate. The hollow site enables a close interaction of two nitrogen atoms with two gold atoms, stabilizing the molecule. In the absence of CO, the Fe ion binding activity increases, changing the adsorption site preference. Nevertheless, the chemisorption energies of CO-FeTMTAA (-2.83 eV) and FeTMTAA (-2.35 eV) are of similar magnitude despite the qualitative differences in the bonding.

The diminished reactivity of the Fe ion leads to an increased Fe$-$surface distance. For the fcc adsorption site, this distance is 3.5 Å, i. e. 0.6 Å more than for the FeTMTAA molecule. At first glance it may seem surprising that the CO-FeTMTAA molecule appears lower than FeTMTAA in STM images because some small ligands at transition metal complexes were previously imaged as protrusions [18, 308, 309]. However, from our calculations, we find that the low apparent height of CO-FeTMTAA is due to an electronic effect. A distant metallic tip will image the nodal plane of the CO $2\pi^*$ orbital as a depression. This is similar to CO on Cu(111) where the molecule reduces the conductance and leads to a depression in constant-current STM images over a range of bias voltages [84, 85]. Similarly, bonding of H to the Mn center of MnPc was observed to cause a depression in experimental and calculated STM images [20].

5.4 Discussion

The addition of a small molecule as an axial ligand to an adsorbed molecule can destabilize the molecular bond to the surface. Hieringer *et al.* demonstrated this surface *trans* effect for metal-tetraphenylporphyrins and their nitrosyl complexes on a Ag(111) surface [141]. Our observations of CO-induced reorganization of FeTMTAA show that the addition or removal of an axial ligand may additionally modify the interactions with nearest-neighbor molecules in the surface plane. Because these molecules are necessarily located in a *cis* position relative to their CO ligands this change may be viewed as a new form of *cis* effect that occurs on surfaces.

A priori, several factors can be at the origin of the surface *cis* effect. The Au(111) substrate with its herringbone reconstruction may play a role as well as the electronic surface state, which is known to mediate an oscillatory long-range interaction [146, 149, 150, 337–340]. None of these factors, however, is significantly different for FeTMTAA and NiTMTAA, in contrast to the patterns they form. Consequently, the differences between FeTMTAA and NiTMTAA and the similarities between CO-FeTMTAA and NiTMTAA are linked to the molecules themselves and their bonds to the substrate. The effect of CO is threefold as deduced from the above experimental and theoretical analysis.

First, CO changes the geometrical structure of the FeTMTAA molecule. According to our DFT calculations of free molecules, the distance between the outermost C atoms along the long axis of the FeTMTAA molecule (Fig. 5.1a) (963 and 971 pm in spin 0 and 1 states, respectively) is reduced in CO-FeTMTAA (950 pm). The latter value is identical to the distance calculated for NiTMTAA. In other words, the reaction with CO geometrically converts FeTMTAA to NiTMTAA. The same trend is calculated for the adsorbed molecules.

Second, a similar conversion is found at the electronic level, where we see that the adsorbed NiTMTAA presents the same features as the adsorbed CO-FeTMTAA (see Appendix C). In agreement with the calculated results, the experimental spectra of CO-FeTMTAA and NiTMTAA exhibit nearly identical peaks.

Finally, bonding of CO to the Fe center weakens the Fe−Au bond and thus diminishes the charge transfer. As a result, the electrostatic interaction between FeTMTAA molecules is affected. FeTMTAA is positively charged, while CO-FeTMTAA is not leading to net repulsion among FeTMTAA molecules that is absent for CO-FeTMTAA. This affects the actual molecular arrangement. FeTMTAA molecules mutually repel owing to their charge state and tend to form a Wigner crystal. CO-FeTMTAA molecules on the other hand tend to form clusters. Their charge state is modified, the electrostatic interaction is reduced, and consequently their arrangement is dictated by the threefold symmetry of the substrate, the intermolecular van der Waals attraction and the steric forces of the ligand groups. The similarity of the CO-FeTMTAA patterns with those of NiTMTAA indicates that CO substantially reduces the electrostatic repulsion, which is consistent with the results of our DFT calculations.

At large coverages FeTMTAA molecules in fcc areas aggregate. A related observation was reported from the molecular donor tetrathiafulvalene on Au(111) [147, 341]. While it forms a Wigner crystal at low coverage, its charge transfer to the surface is reduced at higher coverages and aggregation occurs. Reduced coupling at high coverage was also found for FePc on Ag(111) [143].

5.5 Conclusions

In summary, low-temperature STM data from FeTMTAA on Au(111) show that exposure to CO drastically changes the molecular pattern. A combined experimental and

theoretical study shows that the CO coordination to the Fe center leads to a modified binding to the substrate. Beyond weakening the Fe−substrate bond, which is typical of a *trans* effect, the CO ligand modifies the lateral interaction between molecules. While the *trans* effect relies on orbital-mediated interaction of ligands, the surface *cis* effect reported here involves a ligand-induced charge redistribution between the molecule and its substrate. The presence of CO axial ligands permits the creation of a supramolecular structure while the absence of the ligands leads to the repulsion of the FeTMTAA molecules on Au(111).

6

Iron terpyridine complexes on Au(111): Toward robust spin-crossover compounds

6.1 Introduction

Single molecule switches, triggered by different stimuli [14], are of great fundamental interest and may play a pivotal role in the design of future molecular electronics [7, 8, 91, 268, 342–345]. A promising molecular class for future applications are metal-organic complexes showing spin-crossover (SCO) [151]. SCO complexes contain a transition metal ion that can be switched between a low-spin (LS) and a high-spin (HS) state upon application of external stimuli such as temperature, pressure, magnetic or electric fields or charge flow [151]. A detailed description of SCO is given in Sec. 1.5. Current research of SCO is focused on the synthesis and analysis of new SCO compounds, ideally with full control on the magnetic switchability [17, 155, 158, 346–349].

For application, SCO complexes may be attached to surfaces or electrodes. However, this can lead to complete loss of the switching behaviour [350] or fragmentation of the SCO compound [19, 139, 140]. Therefore, the structural stability of SCO compounds on metal surfaces is of crucial importance. In contrast, the SCO functionality requires a certain degree of flexibility considering that the transition between the LS and the HS state is accompanied by a change of the molecular geometry.

Within this context, bis-terpyridine (tpy) complexes are particularly attractive. In these compounds a metal ion (M) resides in an environment of approximate octahedral symmetry, through its coordination to six N atoms on the two tpy ligands (Fig. 6.1).

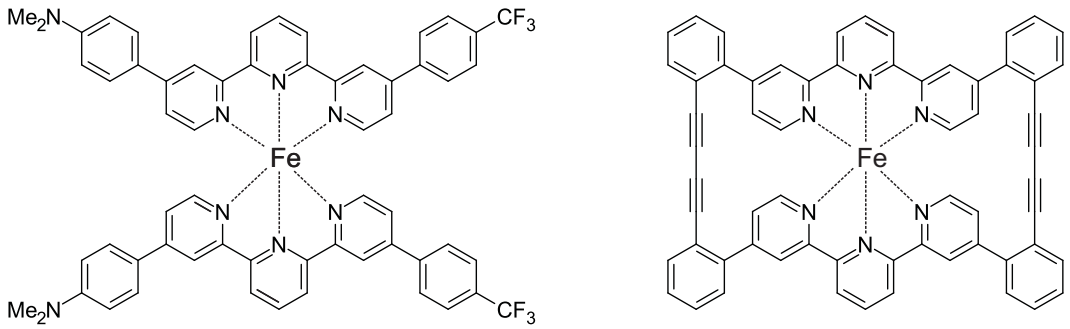

FIGURE 6.1: Schematic representation of the investigated $Fe(tpy)_2$ complexes **1** and **2**.

The presence of two chelate rings[1] per ligand makes the $M(tpy)_2$ motif more stable than the corresponding species with three bipyridine ligands $M(bpy)_3$ [351]. The properties of $M(tpy)_2$ compounds can be tuned by the choice of suitable substituents at the tpy ligands [352]. A distortion of the octahedral coordination environment of the complex is accompanied by a LS−HS transition. The elongation of the Fe−N bonds causes a weakening of the ligand field strength, in turn favoring the HS state (for theoretical details see Section 1.5).

$(tpy)_2$ SCO complexes have been investigated using mechanically controlled break junction (MCBJ) set-ups. Harzmann and co-workers interpreted MCBJ experiments on polar heteroleptic[2] $Fe(tpy)_2$ complexes as electric field induced switching [353]. Moreover, the conductance switching of an homoleptic $Fe(tpy)_2$ complex by mechanical stretching was reported [16]. Tpy ligands were functionalized with anchor groups to ease the contact to the electrodes [16, 353–356]. In other experiments hybrid materials like inorganic-organic radical bifunctional complexes were investigated [357].

Despite the great potential for fundamental SCO research there are only STM investigations on vertically stacked $(tpy)_2$ complex oligomers [358, 359]. STM and atomic force microscopy (AFM) [43, 44] allow a controlled investigation at the single-molecule level. Both methods (alone or combined) may allow to gain further insights into the SCO of single $(tpy)_2$ complexes by measurements of conductance, differential conductance or force [44].

In this chapter, we report on a low-temperature scanning tunneling microscopy and spectroscopy investigation of SCO $Fe(tpy)_2$ complexes deposited on Au(111) by ESI. STM topographs reveal a decomposition of the complexes into single tpy ligands. Three distinct isomeric conformations of the tpy ligand are identified with the help of gas-phase DFT calculations. In order to prevent the fragmentation on the surface, a

[1] A ring-like ligand with two or more separate binding sites to a single central atom is called chelate ring.

[2] A homoleptic chemical compound is a metal compound with all ligands identical. Any metal species which has more than one type of ligand is called heteroleptic.

second SCO complex with additional carbon linkers was synthesized and investigated. It turned out that this approach does not prevent the flattening of the complex, but leads to the formation of interconnected tpy dimers.

6.2 Methods

Experiments were performed with a STM operating in ultrahigh vacuum at 5 K (Chapter 2). Clean Au(111) surfaces were prepared by cycles of Ar^+ sputtering at 1.3 kV and annealing to 500 °C. STM tips were electrochemically etched from a tungsten wire and further prepared in situ by indentation into the substrate. $Fe(tpy)_2(PF_6)_2$ molecules were synthesized by Gero D. Harzmann and Thomas Brandl in the group of Marcel Mayor (University of Basel, Switzerland) following Ref. [352, 360]. The molecules were deposited using the home-built electrospray ionization setup presented in Section 2.2. Stable spray conditions were achieved with $Fe(tpy)_2(PF_6)_2$ molecules solved in acetonitrile. The deposition of $Fe(tpy)_2$ complexes **1** (**2**) was performed by selecting a mass-to-charge ratio of 515 u/e (459 u/e) at a relative kinetic energy of approximately 3 eV (10 eV). The spray voltage was 3.8 kV. During deposition, the pressure in the preparation chamber stayed below 2×10^{-9} mbar and the substrates were kept at room temperature.

Differential conductance spectra were acquired using a lock-in amplifier (sinusoidal modulation voltage of ~ 14 mV_{rms} at 1 kHz.) while the feedback loop was open. All STM topographs were acquired in the constant-current mode.

DFT calculations were carried out using the software Gaussian 09 using the B3LYP functional and the def2TZVP basis set [169, 170, 175, 176].

6.3 Results and Discussion

The molecular structure of $Fe(tpy)_2$ complex **1** is presented in Figure 6.1. Two 2,2′:6′,2″-terpyridine ligands are connected to a central iron atom. The ligands are asymmetric with two different substituents, namely 4-(trifluoromethyl)phenyl and 4-N,N-dimethylaniline. The choice of the different substituents leads to dipolar tpy ligands, which should ease voltage-triggered switching [352, 361].

The gas-phase structure of $Fe(tpy)_2$ **1** was obtained by DFT calculations (Fig. 6.2). The complex has a cruciform appearance with two almost orthogonal near-plane tpy ligands, resulting in a nearly perfect octahedral ligand sphere. The distance between the central iron atom and the nitrogen atoms is in the range $1.9 - 2.0$ Å. The calculated angles and bond length are comparable to that commonly reported for $M(tpy)_2$ complexes [351, 362]. The phenyl groups of the substituents are rotated by $25 - 30°$ with respect to the pyridine units. The length of a single ligand from one substituent to the other is ~ 23 Å.

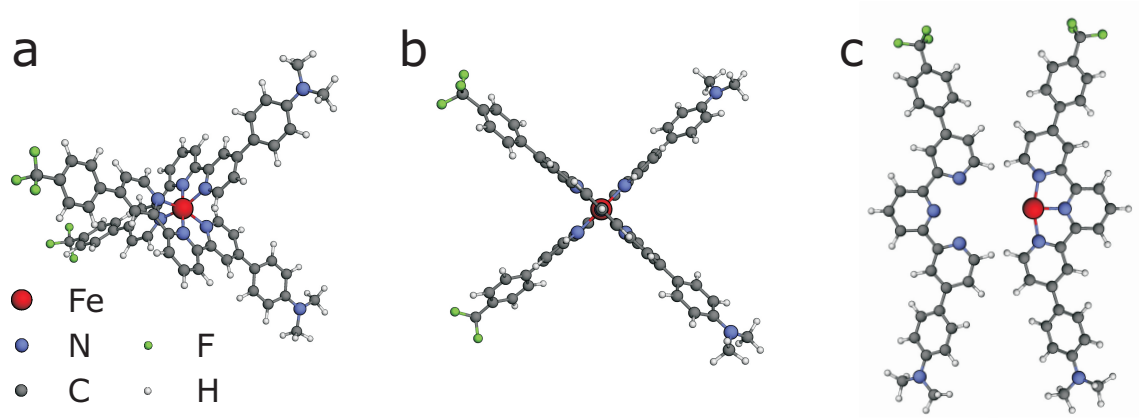

FIGURE 6.2: (a,b) Different views of the calculated gas-phase structure of $Fe(tpy)_2$ **1** in the low spin state. (c) Top view of the separated tpy ligands.

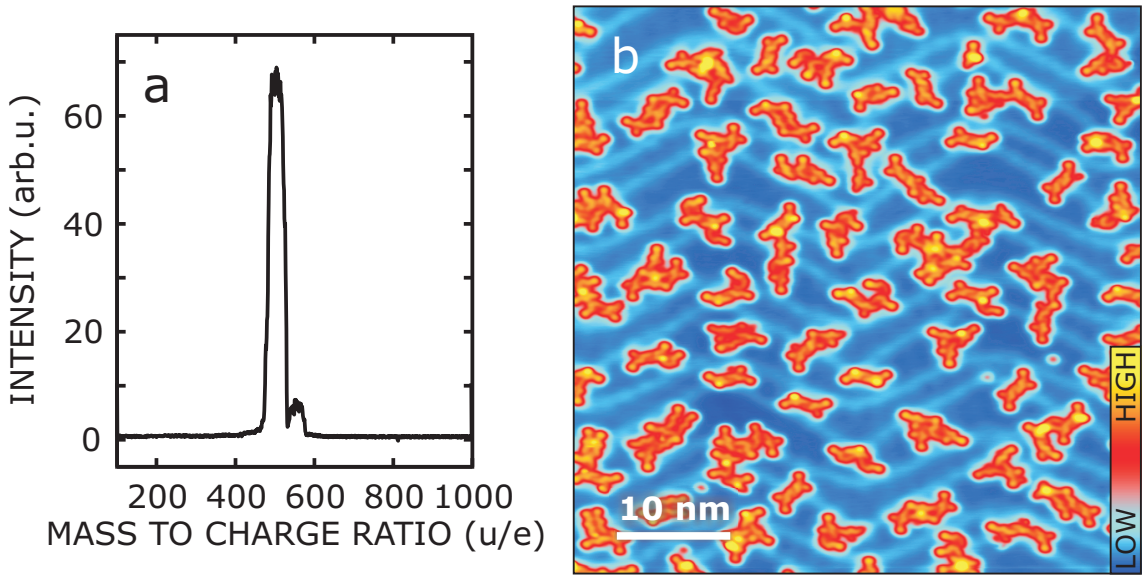

FIGURE 6.3: (a) Typical mass spectrum of electrosprayed $Fe(tpy)_2$ **1** ions. A well-pronounced peak is observed corresponding to intact, doubly charged $Fe(tpy)_2$ **1** molecules (524 u/e). (b) Large-scale STM topograph ($V = 0.1$ V, $I = 75$ pA) upon ESI deposition of $Fe(tpy)_2$ **1** onto Au(111).

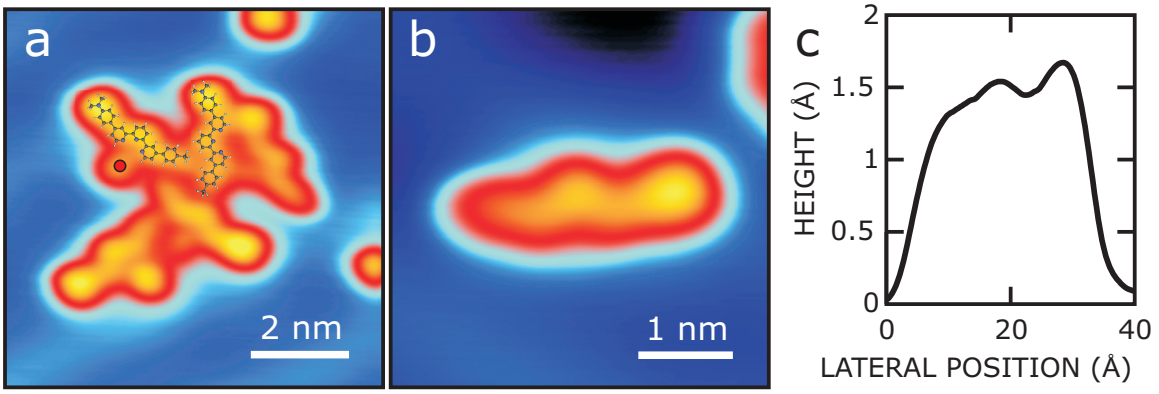

Figure 6.4: (a) STM topograph ($V = -0.1$ V, $I = 10$ pA) of tpy ligands on Au(111) with superimposed scaled molecular models. A red circle indicates the position of an iron atom. (b) STM topograph ($V = 0.1$ V, $I = 20$ pA) of a tpy ligand in the *cis-cis* configuration. (c) Height profile along the long axis of a tpy ligand.

The $Fe(tpy)_2$ complex **1** was deposited on Au(111) using ESI (see Section 2.2). Prior to deposition, the molecular ion beam was analyzed by an in-line quadrupole mass spectrometer. Figure 6.3a shows a typical mass spectrum. A well-pronounced peak is observed corresponding to intact, doubly charged $Fe(tpy)_2$ **1** molecules (524 u/e). The m/z value of this peak was used to deposit the mass-selected $Fe(tpy)_2$ **1** molecules on the surface. An additional small peak may be assigned to single, singly charged tpy ligands attached to an Fe atom (552 u/e). This indicates that a small amount of the complexes (< 10 %) dissociates during the spray process. Since the same resolution setting was used for spectroscopic measurements and mass-filtering during deposition, the ion beam reaching the surface may consist of ions of the left peak mainly. Therefore, most of the molecules are considered to be intact when they reach the surface.

Figure 6.3b shows a typical large-scale STM topograph of a Au(111) sample after the ESI deposition of the $Fe(tpy)_2$ complex **1**. The herringbone reconstruction of the clean Au(111) surface is clearly discernible as bright lines on a blue background. Disordered clusters consisting of different molecular structures are observed. The most common structure has an elongated shape with a length of approximately 3 nm. Structures of different appearance will be addressed later.

In the zoomed STM topograph of Figure 6.4a, we superimposed molecular models of single tpy ligands resulting from gas-phase DFT calculations (Fig. 6.2c). The match between the model ligands and the STM topograph suggests that these longish structures are single, uncoordinated tpy ligands (Fig. 6.4b). Three of the five tpy ligands in the cluster exhibit an additional protrusion at the side. These protrusions may be attributed to single Fe atoms resulting from the fragmentation of the $Fe(tpy)_2$ complex. Further justifications for these attributions will be given below. The tpy ligands have an apparent height of ~ 1.5 Å at $+1.0$ V. This apparent height is comparable to

the height of similar molecules with π orbitals pointing out of the surface [288, 289]. Therefore, we propose a planar adsorption geometry with the cyclic subunits lying flat on the surface.

Figure 6.4b shows a topograph of an isolated tpy ligand (without an Fe atom) recorded at 100 mV. The topograph of the ligand has a bright lobe with an higher apparent height, being located at the right end of the ligand. The line profile along the longitudinal axis reflects this asymmetry (Fig. 6.4c). This is consistent with the fact that the tpy ligand has two different substituents, namely CF_3 and Me_2N.

In the following, the substituents will be identified by a combination of voltage dependent STM topographs, STS and DFT calculations. Figure 6.5a (b) shows a STM topograph of a tpy dimer recorded at -1.4 V ($+1.0$ V). While at -1.4 V there are two bright lobes cleary discernible, at $+1.0$ V the ligands have the same apparent height at both ends. This height difference is illustrated by two line profiles recorded at both voltages (Fig. 6.5c).

In addition, STS was performed at both ends of the tpy ligand (Fig. 6.5d). The tip positions during acquisition are marked in the inset of Fig. 6.5d. The spectrum measured at the right end of the ligand (black) does not exhibit any characteristic molecule-related features and resemble spectra acquired over the bare Au(111). $\mathrm{d}I/\mathrm{d}V$ spectra recorded at the left end of the ligand (grey) show the onset of an intense resonance at sample voltages below -1 V. We attribute this resonance to the highest occupied molecular orbital (HOMO) of the ligand. To assign the position of the HOMO to one of the two substituents, we use gas-phase DFT calculations of a single tpy ligand. To model the ligands of $Fe(tpy)_2$ **1** adsorbed on an Au(111) substrate, the carbon rings of the tpy ligands were forced to adopt a planar geometry. Figure 6.5e shows top views of calculated isosurfaces of the HOMO and the LUMO. The HOMO is mainly located at the dimethylaniline group and the adjacent pyridine ring. In contrast, the LUMO is spatially extended over the side of the ligand with the CF_3 group. This spatial distribution of HOMO and LUMO is qualitatively the same for the unrestricted ligand. Summarizing the above findings, we can ascribe the bright lobe in STM topographs at voltages below -1 V to the dimethyl group of the tpy ligand.

The protrusions lateral to the tpy ligands (Figs. 6.4a and 6.5a,b) are attributed to Fe atoms considering that (i) the protrusions have an apparent height between 1.3 and 1.6 Å at V = 100 mV. A similar height was reported for single Fe atoms, which were deposited on Au(111) using electron beam evaporation [67]; (ii) STS on the Fe atoms show no Kondo feature, as expected from previous investigations. Indeed, some transition-metals (e. g., Ti, Co and Ni) adsorbed on Au(111) can be identified by characteristic Kondo features near the Fermi energy [97, 133]. Other elements (V, Cr, Mn and most notably Fe) display a featureless electronic structure in this range [133]; (iii) a statistical evaluation of Fe atoms and tpy ligands yields a ratio of 1:2.04. This is very close to the expected ratio of 1:2, assuming that the adsorption leads to the dissociation of the complex into one Fe atom and two tpy ligands. The Fe atoms lie close to the coordination site of the three nitrogen atoms

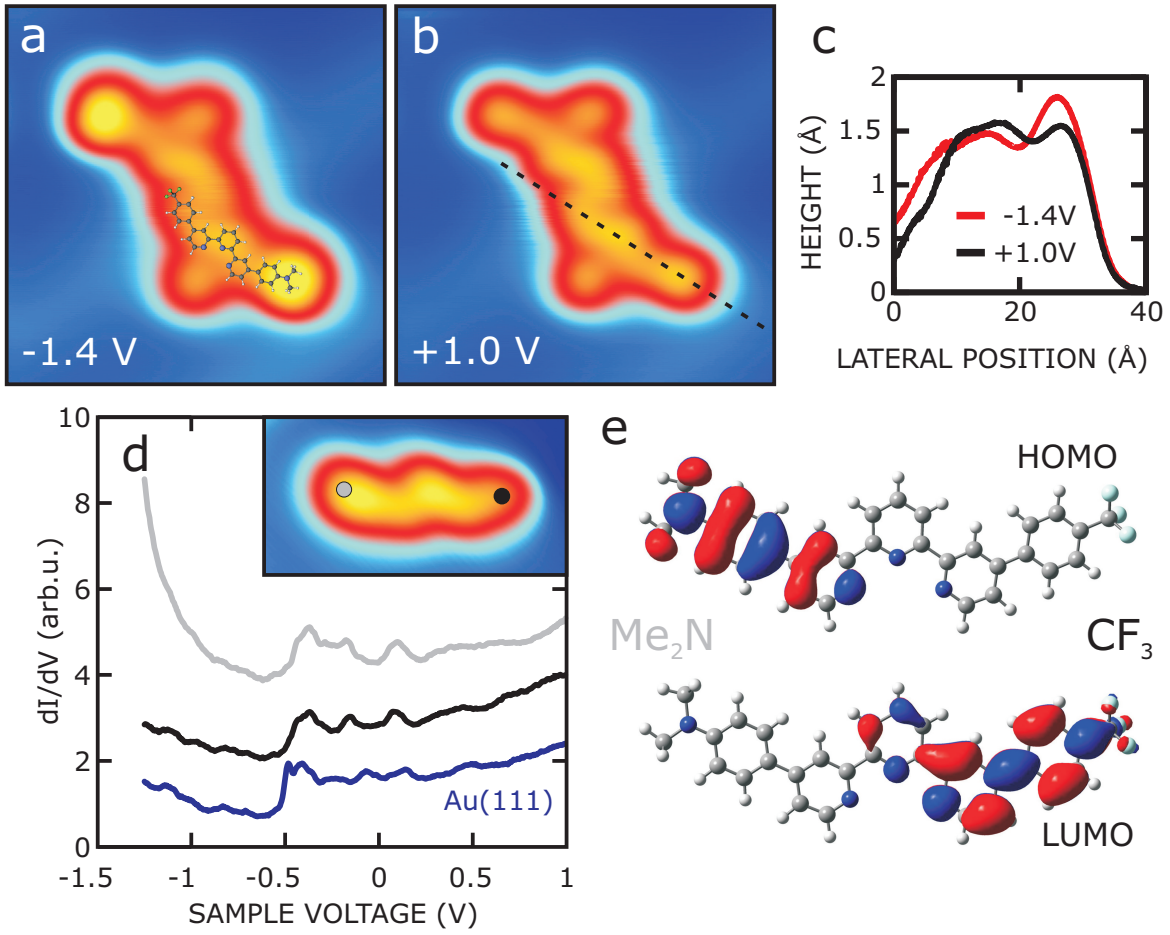

Figure 6.5: (a,b) STM topographs of two tpy ligands each on Au(111) with a superimposed scaled molecular model. Tunneling parameters: $I = 100$ pA, (a) $V = -1.4$ V, (b) $V = +1.0$ V. (c) Height profiles of a tpy ligand. The profiles are taken along the dashed line indicated in (b). (d) $\mathrm{d}I/\mathrm{d}V$ spectra of a tpy ligand on Au(111). The spectra were acquired at both ends of the ligand and on bare Au(111). The spectra are vertically shifted for clarity. The feedback loop was opened at $V = 1$ V, $I = 100$ pA. The inset ($V = 0.1$ V, $I = 20$ pA) shows the positions used for spectroscopy. (e) Calculated wave functions of the tpy ligand HOMO and LUMO (isocontour representation).

of the tpy ligand. The separation of central nitrogen atom and the iron atom is in the order of 5 Å and therefore significantly larger than expected for a coordinative bond.

In the following different conformations of the tpy ligand will be discussed. Uncoordinated tpy ligands are found in a conformation with the two NC−CN rotamers of the adjacent pyridine units in the N,N-*transoid* form (Fig. 6.6a) both in solvents and solid state [352]. To simplify the discussion below, we introduce the angle α (β). For $\alpha = 0$ ($\beta = 0$) the left (right) bipyridine is in the *cisoid* orientation, for $\alpha = 180$ ($\beta = 180$)

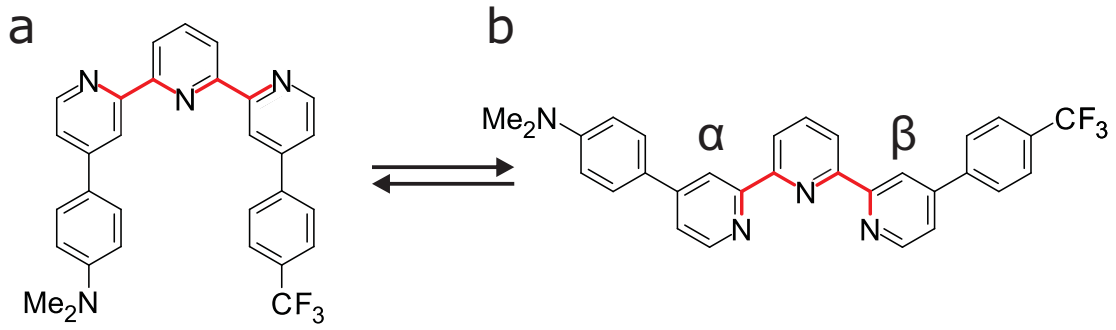

FIGURE 6.6: (a) Conformation of a tpy ligand with both NC−CN rotamers in *trans* form. NC−CN rotamers of the pyridine units are highlighted in red. (b) A tpy ligand in the *cisoid* conformation.

the left (right) bipyridine is in the *transoid* orientation. A detailed definition of α (β) can be found in Appendix D. The coordination to Fe imposes a *cisoid* orientation of the NC−CN rotamers of the ligand (Fig. 6.6b). Thus, being part of the iron complex both ligands are in full *cisoid* orientation. As we have seen above, the fragmentation of the iron complex during the adsorption creates coordinated and uncoordinated tpy ligands. Consequentially, the uncoordinated tpy ligands may be expected to present different conformational isomers on the Au(111) surface.

Indeed, two other structural isomers can be observed besides the *cis-cis* conformer (denoted **CC** below, Fig. 6.7a). Figure 6.7b shows an asymmetric pattern which matches the structural model of a tpy ligand after the rotation of the right NC−CN rotamers (Fig. 6.7e). This *cis-trans* conformation ($\mathbf{C_M T_F}$, M and F denote the different substituents Me_2N and CF_3, respectively) is unsuited to metal coordination. The *trans-trans* form (**TT**, Fig. 6.7f) results in the conformer of Figure 6.7c. In this conformation the opposite substituents appear close to each other forming a ring-like structure. The Me_2N group is clearly discernible for all conformations.

The abundance of the different conformers has been obtained by evaluating large-scale STM images with a total of 1021 ligands (Fig. 6.7g). For the uncoordinated tpy ligands the **CC** conformation is most abundant (32%). The proportion of $\mathbf{C_M T_F}$ and **TT** conformers is considerably lower (15% and 4%, respectively). Interestingly, tpy ligands in the *trans-cis* conformation $\mathbf{T_M C_F}$ were not observed.

In the following, this distribution is compared to DFT calculations of the different isomers. In Table 6.1 the gas-phase total energies of the tpy ligand isomers are given with respect to the energy of the **CC** conformer. The sequence of stability (from most stable to less stable) is $\mathbf{TT} > \mathbf{T_M C_F} > \mathbf{C_M T_F} > \mathbf{CC}$. The total energy of **TT** is lowest because in this configuration the repulsion between the lone pairs on the N atoms of the adjacent pyridine units is avoided [363]. In the gas-phase, the pyridine ligands of all conformers are slightly rotated by up to 43° with respect to the central pyridine unit. To model the geometry on the Au(111) surface, additional calculations have been

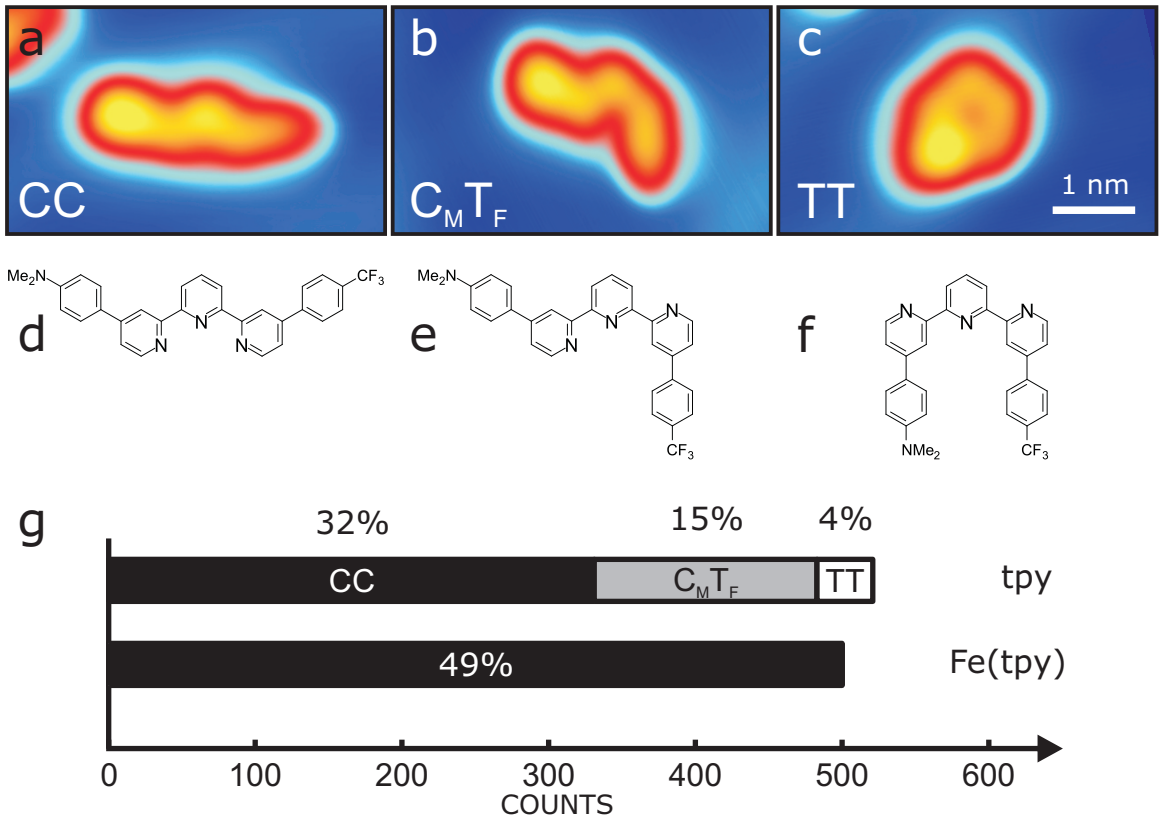

Figure 6.7: (a-c) STM images of three distinct conformers of the tpy ligand on Au(111). Tunneling parameters: $I = 20$ pA, (a,b) $V = 0.1$ V, (c) $V = 0.3$ V. The scale bar is valid for all images. (d-f) Structural models of the tpy ligand in different isomeric forms. (g) Number of ligands in the different conformations on Au(111).

performed with all conformers forced to adopt a planar geometry (Tab. 6.1). This does not change the order of stability.

The abundance of each conformer does not necessarily retrace the stability of the conformers. For instance, the reaction to the most stable conformer may be hindered by a substantial energy barrier. To estimate the energy barrier between the conformers, one-dimensional potential energy surface (PES) scans connecting the different conformations have been performed at the B3LYP/def2SVP level (Fig. 6.8). Consecutively, β and α were stepwise modified starting from the **CC** isomer in a flat conformation. This corresponds to a rotation of the right and the left NC−CN rotamer. The scans were performed with 10° increments of the dihedral angle in 21 and 26 steps, respectively. All other parameters were optimized to their most favorable values. The resulting potential energy profile shows three local minima corresponding to the conformations **CC**, $\mathbf{C_M T_F}$ and **TT**. If first α and subsequently β are modified, the $\mathbf{T_M C_F}$ conformer is included in the energy profile (red line). In contrast, the energy profile includes

	CC	$\mathbf{T_M C_F}$	$\mathbf{C_M T_F}$	**TT**
ΔE (meV)	0	−299	−315	−526
ΔE_{flat} (meV)	0	−399	−431	−662

TABLE 6.1: Gas-phase total energies of the tpy ligand isomers in a free and a flat geometry with respect to the energy of the **CC** conformer. Calculations have been performed at the B3LYP/def2TZVP level.

the $\mathbf{C_M T_F}$ conformer, if first β and then α are swept (black/grey line). Both energy profiles do not significantly differ from each other. In both cases the highest energy barriers in the energy profile between the **CC** conformer and the **TT** conformer in the gas-phase are of the order of 100 meV. Also the energy barriers between **CC** and $\mathbf{C_M T_F}$ and **CC** and $\mathbf{T_M C_F}$ are very similar. Typical adsorption energies are considerably larger (e. g., benzene on Au(111): 0.64 eV [364]). Therefore, the gas-phase calculations are not sufficient to (i) explain the relative abundance of the conformers nor (ii) the apparent absence of the $\mathbf{T_M C_F}$ conformer.

The low abundance of the **TT** conformer may therefore be explained by the influence of the surface. In this context, two possibilities has to be considered: (i) Intact complexes arriving at the surface comprise tpy ligands in the **CC** configuration. During the adsorption, the surface may hinder the rotation of the rotamers. The statistical distribution found on the surface (Fig. 6.7g) may thus reflect that the formation of the **TT** conformer requires rotation of two rotamers while the $\mathbf{C_M T_F}$ conformer is obtained by the rotation of a single rotamer only. (ii) The relative energy of the different conformers on the surface may be totally different than in the gas-phase. This scenario seems possible as the distances between the four nitrogen atoms in conformers $\mathbf{C_M T_F}$ and $\mathbf{T_M C_F}$ are different and must adopt different adsorption sites (see Appendix D for details). DFT calculations of the molecule on Au(111) would allow a comparison of the adsorption energies and may clarify the abundance of the conformers.

These results may be compared to a study by Karan *et al.* [289]. A tetranuclear Co-grid complex incorporating $(tpy)_2$ ligands was electrosprayed onto a Au substrate. Fragmentation of the complex led to $(tpy)_2$ ligands in four different conformations. However, the most abundant conformer was not in the configuration that it has in the intact complex. Furthermore, no cobalt ions of the grid complex were found on the surface. In contrast, we observed the iron atoms of the dissociated $Fe(tpy)_2$ complexes trapped at half of the ligands. This may be due to a different fragmentation mechanism as a result of the more convoluted, grid-type architecture of the Co complex. In contrast, the structure of the Fe complex may allow a direct trapping of the Fe atoms.

Intact SCO complexes were not observed on the surface. The reason for the fragmentation may be the affinity of aromatic cycles to metal substrates [143, 289, 365]. Recent work on $[Fe(bpz)_2(phen)]$ [3] shows that this complex dissociates into $[Fe(bpz)_2]$

[3] bpz=dihydrobis(pyrazolyl)borate, phen = 1,10-phenanthroline.

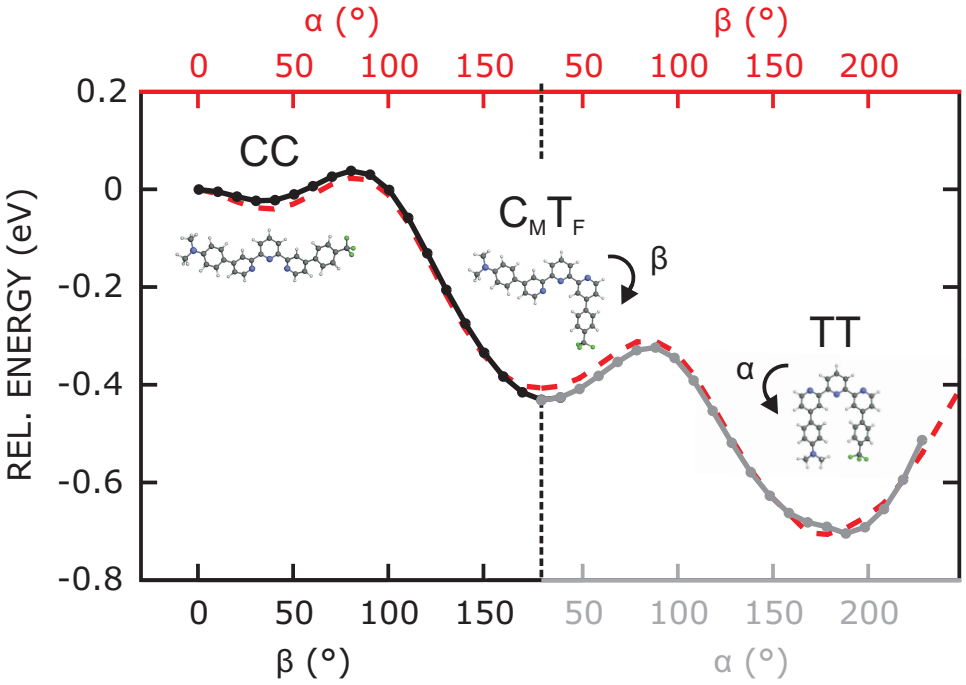

Figure 6.8: Relaxed potential energy scan connecting conformers **CC**, $\mathbf{C_M T_F}$ and **TT**, calculated at the B3LYP/def2SVP level, as function of the dihedral angles β (black) and α (grey). The relative energy is given with respect to the energy of the flat **CC** conformer. For comparison the energy profile connecting conformers **CC**, $\mathbf{T_M C_F}$ and **TT** is shown as a red dashed line. Note that the energies of the conformers should not be compared to that of Table 6.1 as different basis sets were used.

and phen on Au(111) [139]. Phen ligands were found to lie flat on the surface. A dissociation on Au(111) was also reported for the SCO complex $[Fe(H_2B(pz)_2)_2(phenme_4)]$ [140].

Reinforced iron terpyridine complex

The fragmentation of the $Fe(tpy)_2$ SCO complex **1** into single ligands calls for a reinforcement to avoid the dissociation on the surface. The calculated gas-phase structure of the reinforced $Fe(tpy)_2$ complex **2** is shown in Figure 6.9a. In contrast to complex **1**, there are no additional substituents except for the phenyl groups. For reinforcement, the ligands of complex **2** are connected by two additional carbon chains between the outer phenyl rings. Hence, the rotation angle of the phenyl rings with respect to the pyridine units is increased to approximately 55 and 85°, respectively. The octahedral ligand sphere of the iron center and the N atoms is preserved.

The reinforced $Fe(tpy)_2$ complex was deposited on Au(111) using ESI. The molecular ion beam was analyzed by a quadrupole mass spectrometer prior to deposition. Typical mass spectra (Fig. 6.9b) show a clear peak, attributed to intact $Fe(tpy)_2$ **2**

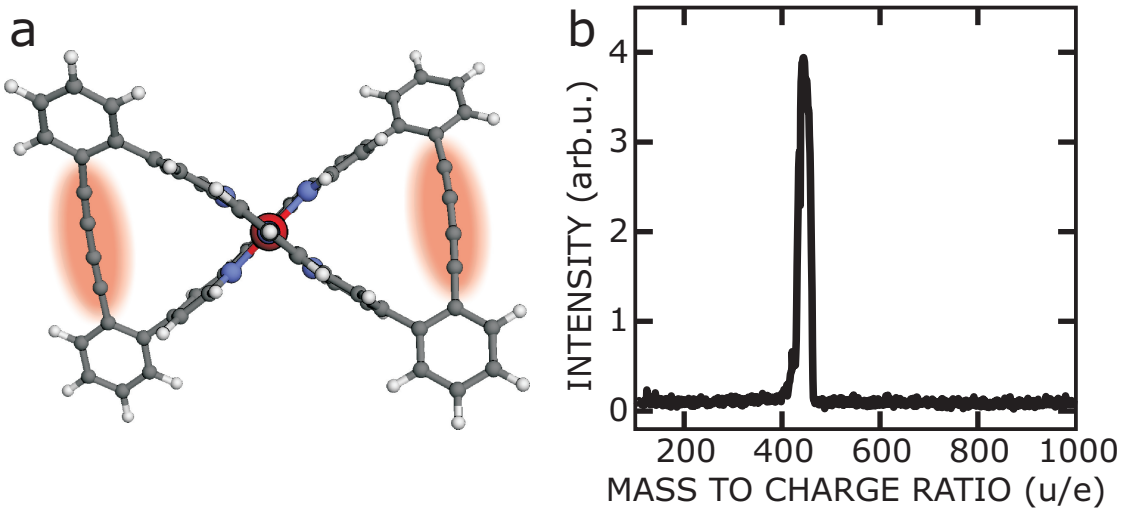

FIGURE 6.9: (a) Calculated gas-phase structure of the $Fe(tpy)_2$ complex **2**. The reinforcement is highlighted in red. (b) Typical mass spectrum of electrosprayed $Fe(tpy)_2$ **2** ions.

molecules (459 u/e). In contrast to the mass spectra of complex **1** (Fig. 6.3a), there is no second peak in the spectra.

Figure 6.10a shows a STM topograph, upon deposition of complex **2**, exhibiting three adsorbates. Each adsorbate consists of two ligands in the *cis-cis* configuration. In contrast to the observations on complex **1**, each ligand has a symmetric shape. This is consistent with the absence of the substituents CF_3 and NMe_2. Similar to complex **1**, tpy ligands take a flat geometry on the Au(111) surface. The calculated geometry of the intact complex **2** would lead to tilted ligands with one or two phenyl groups pointing into vacuum. Therefore, the adsorption of the molecule on the surface might distort the molecule.

Tpy ligands are exclusively observed as dimers in contrast to the observation of individual ligands upon deposition of complex **1**. No other conformers than the *cis-cis* configuration are observed. This indicates that complex **2** does not dissociate completely into two ligands. However, the complex adopt a planar conformation, different from the gas-phase conformation. In the present case, the carbon linker seem to have a double function: They prevent (i) a rotation of the phenyl groups, which would lead to different conformers, and (ii) a desintegration of the dimer structure. Actually, the STM topograph of a dimer matches the molecular model of complex **2** in a flat geometry without the iron atom (Fig. 6.10b). All adsorbates exhibit the same dimer structure. Beyond that, the appearance of the dimers varies especially regarding the center. While the dimer shown in Fig. 6.10b exhibits a depression in the middle, other dimer feature a protrusion at different positions. This may be explained by a loss of the Fe atom during adsorption. In a flat geometry the distance of a possible central

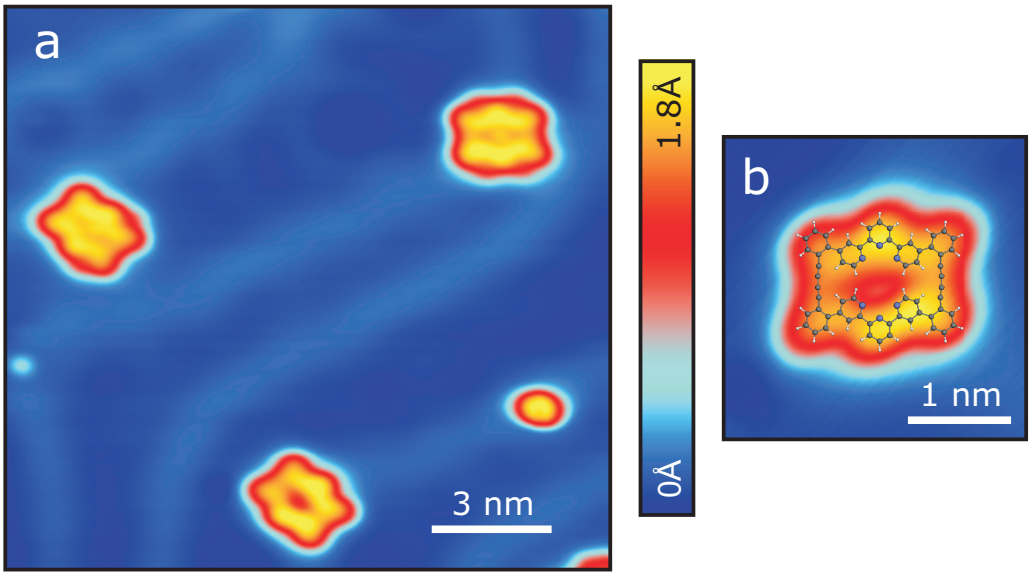

Figure 6.10: (a) STM topograph ($I = 100$ pA, $V = 0.1$ V) of complex **2** on Au(111). (b) STM topograph ($I = 200$ pA, $V = 0.1$ V) of a dimer of tpy ligands. A scaled molecular model in a flat geometry is superimposed.

iron atom to the six N atoms is larger than 3.5 Å and therefore incompatible with coordinative bonds.

6.4 Conclusion

In summary, we reported on the ESI deposition of two $Fe(tpy)_2$ SCO complexes on Au(111). STM investigations show that the $Fe(tpy)_2$ complex **1** dissociates into tpy ligands, which lie flat on the surface. Different substituents of the tpy ligands could be identified. Iron atoms are observed adjacent to half of the tpy ligands. The remaining tpy ligands are found in three different conformations. Mass spectrometric detection indicates that $Fe(tpy)_2$ **1** is intact in the gas-phase. This suggests a surface-induced ligand-dissociation process. Interestingly, DFT calculations show that the most abundant conformer on the Au surface is not energetically favored in gas-phase. Rather, this configuration conforms to the configuration of the ligands in the intact complex. This also supports that the complex dissociates due to the adsorption on the gold surface.

These results may be important for the interpretation of future MCBJ experiments. Molecules are usually deposited from solution on the MCBJ sample, while we used the ESI technique. Nevertheless, it should be considered that fragile molecules may dissociate upon adsorption at the gold electrodes.

To limit the dissociation on Au(111) two carbon linkers were introduced between the tpy ligands. The new complex **2** is found to form interconnected dimers upon deposition on the gold substrate. Apparently, this modification cannot suppress the flattening of this type of SCO complex on Au(111). Nevertheless, the new design prevents the complete dissociation into single ligands.

While the deposition of intact molecules was not successful, the fragmentation allowed investigation and identification of substituents and conformations of the tpy ligand molecules. In contrast, the three dimensional structure of intact SCO complexes makes the correct identification very difficult [19, 139, 366].

The design of robust SCO complexes on metal surfaces remains challenging. However, our observations may be fundamental for the design of new, robust SCO complexes composed of $Fe(tpy)_2$.

Conclusion

In conclusion, this thesis contributes to the fundamental understanding of various physical phenomena at the molecule−metal interface. Different classes of transition metal complexes have been investigated by low-temperature scanning tunneling microscopy at the single-molecule level.

In many studies the Kondo effect is employed as a readout channel of magnetic properties of adsorbed molecules. In this thesis, the spatial extent of Kondo resonances in magnetic sandwich complexes was investigated. We reported the ESI deposition of a trinuclear organometallic complex on Cu(111). Differential conductance spectra revealed two Kondo resonances with different spatial extents and different energies. In contrast to magnetic adatoms, where the orbitals at the origin of Kondo resonances may be degenerate and spatially overlap, here the strong ligand field lifts the orbital degeneracy. Furthermore, thanks to a particular hybridization of the metal and ligand orbitals, the Kondo resonances can be independently studied by selecting adequate areas of investigation over the molecule. These results open promising perspectives for investigating complex Kondo systems composed of several Kondo orbitals.

Sandwich molecules turned out to be an ideal playground for Kondo studies. As a perspective of this work, the impact of different magnetic ions within sandwich molecules on the Kondo physics can be investigated. Moreover, sandwich molecules with a larger size of the aromatic ligands might show interesting effects [367–370].

Interconnected molecular magnetic centers on metallic surfaces present an excellent playground for studying fundamental aspects of magnetic sytems. We demonstrated the deposition of three molecules, NBC, NTC, and BTC, composed of interconnected cobaltocene magnetic centers, on metallic substrates. Although the molecules are composed of the same magnetic center, a Kondo resonance is observed for one complex only, with varying amplitude from molecule to molecule. Different Kondo resonance amplitudes of NBC on Au(111), and the absence of a Kondo resonance for NTC and BTC on Au(111) and Cu(111), respectively, are attributed to particular coupling of the cobaltocene units to the substrate. By comparing the different cases and linkers, factors influencing the coupling are identified. For future molecular-spintronics applications, it appears fundamental to take these factors into account in the design of new molecules composed of interconnected magnetic centers.

As a perspective, it would be interesting to further investigate the influence of different linkers between cobaltocene units. I have already carried out first STM investigations on a 1,3,5-substituted tricationic cobaltocenium benzene complex with elongated linkers between the cobaltocene units and the central benzene ring [190]. Further investigations are necessary to ensure that the molecules are intact on the surface.

Furthermore, the influence of axial ligands on intermolecular interactions on surfaces has been investigated. Low-temperature STM data from FeTMTAA on Au(111) show that exposure to CO drastically changes the molecular pattern. A combined experimental and theoretical study shows that the CO coordination to the Fe center leads to a modified binding to the substrate. Beyond weakening the Fe−substrate bond, which is typical of a trans effect, the CO ligand modifies the lateral interaction between molecules. While the trans effect relies on orbital-mediated interaction of ligands, the surface cis effect reported here involves a ligand-induced charge redistribution between the molecule and its substrate. The presence of CO axial ligands permits the creation of a supramolecular structure, while the absence of the ligands leads to the repulsion of the FeTMTAA molecules on Au(111).

Our findings illustrate how the self-assembly of adsorbed, complexed metal centers results from the interplay between the influences of the surface and the coordinated ligand on this metal center. These results could be taken into account for the development of sensor and catalysis technology using metal complexes.

Dissociation of spin crossover (SCO) molecules on metal surfaces is a serious problem. We carried out a study on the adsorption of two iron terpyridine (tpy) SCO complexes on Au(111). STM topographs show that the first complex dissociates into tpy ligands, which lie flat on the surface. Iron atoms are observed adjacent to half of the tpy ligands. The remaining tpy ligands are found in three different conformations. Interestingly, DFT calculations show that the most abundant conformer on the surface is not energetically favored in gas-phase. Therefore, we assume a surface-induced dissociation process. To suppress the dissociation on Au(111), two carbon linkers were introduced between the tpy ligands. This second complex is found to form interconnected dimers upon deposition to the gold substrate.

The design of robust SCO complexes on metal surfaces remain challenging. On-surface DFT calculations may provide deeper insight into the dissociation process. This may be fundamental for the design of new, robust SCO complexes composed of tpy ligands.

A

Supporting information for: Ligand-Induced Energy Shift and Localization of Kondo Resonances in Trinuclear Cobalt-Based Complexes on Cu(111)

Deposition and mass spectra of TCBB molecules

TCBB molecules (calculated mass of 674 u) are triply charged and are therefore electrically stabilized in bulk form by three hexafluorphosphate anions (PF_6^-, calculated mass of 145 u) per molecule (Fig. A.1b) [253]. A powder composed of TCBB molecules and hexafluorphosphate counter ions was dissolved in nitromethane for deposition on Cu(111) using a home-built *in situ* ultrahigh-vacuum electrospray ionization setup with mass selection [214].

Prior to deposition, the TCBB ion beam was analyzed by an in-line quadrupole mass spectrometer. Figure A.1a shows a typical mass spectrum. A single peak is observed at $\approx$ 218 u/e corresponding to a triply charged TCBB molecule (225 u/e) without the counter ion (PF_6^-). The mass spectrum indicates that these anions are lost during the spraying process. We note that neither SCBB nor DCBB molecules are observed in the mass spectrum. Therefore, the SCBB and DCBB molecules imaged on the Cu(111) surface most likely result from fragmentation of TCBB upon adsorption.

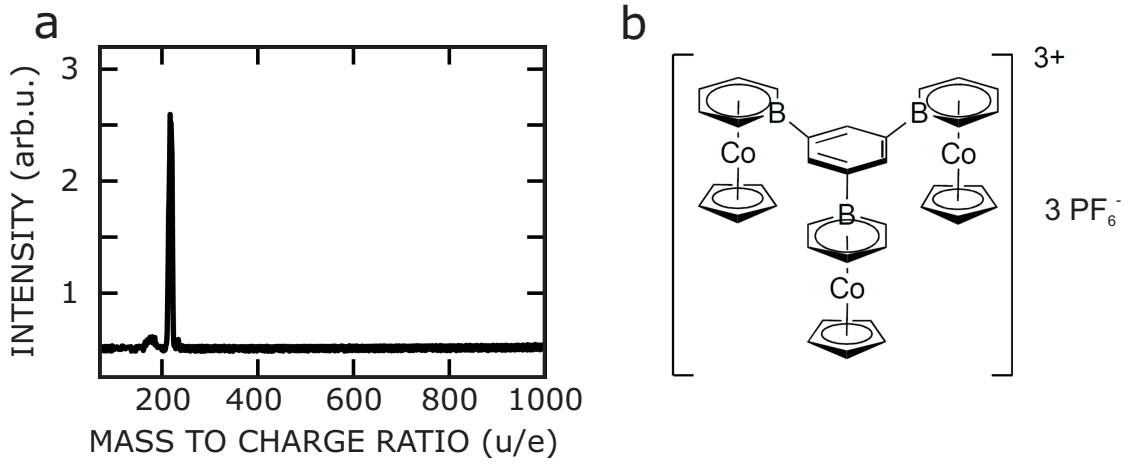

FIGURE A.1: (a) Typical mass spectrum of electrosprayed TCBB ions. (b) Schematic structure of TCBB.

The deposition of TCBB molecules on Cu(111) was performed by selecting a mass-to-charge ratio of 220 u/e at a kinetic energy of 8 eV. During the deposition onto a Cu(111) sample held at room temperature the pressure in the preparation chamber was kept below 2×10^{-9} mbar.

Estimate of the tilt angle of SCBB on Cu(111)

Topographs of SCBB exhibit a depression that is not centered to the image of the molecule, suggesting that the SCBB molecules are tilted. Figure A.2a shows a STM topograph of a SCBB molecule on Cu(111). Its cross-sectional profile (b) exhibits two maxima separated by 4.5 Å with an apparent height difference of 0.6 Å. For a simple estimate, we assume that the height difference is of purely geometrical origin, namely a tilt of the molecule relative to the substrate normal. From the profile we thus infer a tilt angle $\theta = 8°$ ($\tan\theta = 0.6$ Å / 4.5 Å). The resulting geometry is presented in Figure A.2c. Interestingly, our estimated value is very close to the tilt angle of 9° found from DFT calculations (discussed below).

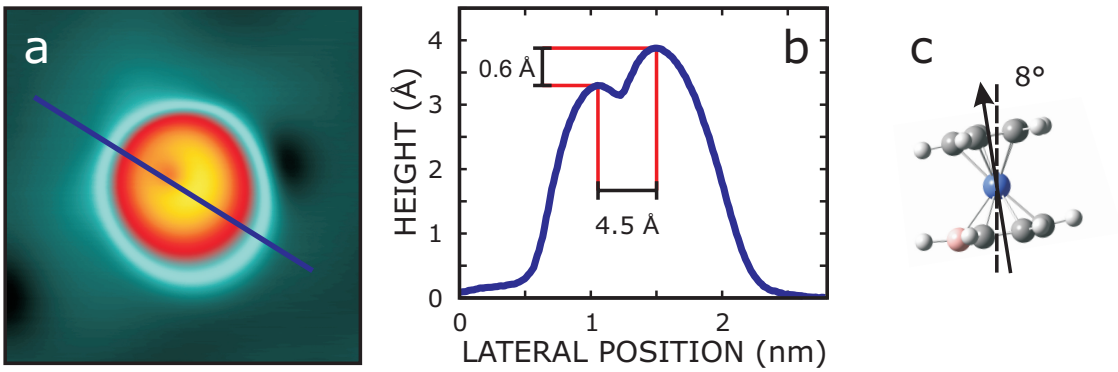

FIGURE A.2: (a) Constant-current STM topograph ($I = 200$ pA, $V = 0.1$ V) of a SCBB molecule on Cu(111). (b) Cross-sectional profile along the blue line in (a). (c) Side view of a SCBB molecule illustrating the tilt. Solid and dashed lines show the molecular axis and the substrate normal, respectively.

Tip-induced manipulation of TCBB on Au(111)

Figure A.3 shows a sequence of three topographs illustrating the tip-induced displacement of a TCBB molecule on Au(111). While scanning over the molecule of interest, for given tunneling parameters, a "dislocation" line can appear in the topograph. This is shown in Figure A.3b where such an horizontal line is visible while scanning over the lower CBB unit. As shown in Figure A.3c, this resulted in the displacement/rotation of the entire TCBB molecule. This manipulation indicates that STM images most likely show molecules that are chemically bonded rather than three CBB units that happened to arrange themselves in a triangular pattern.

As discussed in the previous section, CBB units exhibit an off-center depression, whose lateral position depends on the tilt of the unit relative to the surface. For a TCBB molecule, the depression of the three CBB units are initially toward the middle (e. g., Fig. A.4a). This indicates a tilt of the CBB units towards the center, i. e. the distance between the CBB units is fixed at the surface (by the benzene group) and the distance is reduced at the apex of the molecule. Figure A.4 shows a voltage-induced manipulation of the tilt of the lower CBB unit.

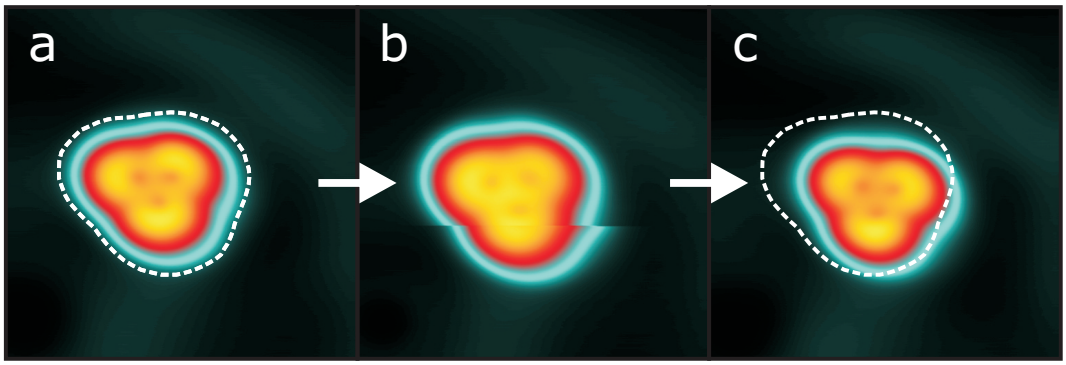

FIGURE A.3: Topographs of a TCBB molecule on Au(111) (a) before, (b) during and (c) after tip-induced manipulation. The initial position of the molecule is indicated by a dashed contour. The scans started at the top-left edge and ended at the bottom-right edge of the topographs. The tunneling parameters are $I = 100$ pA and (a) $V = 0.2$ V, (b) $V = 1.4$ V and (c) $V = 0.1$ V.

Scanning Tunneling Spectra

dI/dV spectra of TCBB on Cu(111) and on Au(111) over a bias range of 3 V are displayed in Figure A.5. The dI/dV spectrum acquired on TCBB/Cu(111) shows a sharp Kondo resonance close to the Fermi level along with a very broad feature at its right side. This broad feature may possibly correspond to the d_{xz} state expected for TCBB on Cu(111). For TCBB on Au(111) no spectroscopic features are observed around zero bias but a clear and broad resonance at ≈ 0.9 eV with a broadening of ≈ 1.3 eV.

Figure A.6a shows six typical dI/dV spectra of TCBB on Cu(111). The tip positions for data acquisition are marked in the constant-height STM topograph shown in Figure A.6b. Two spectra are displayed for each CBB subunit. On SCBB, two Kondo resonances at different energies were observed in and off the symmetry axis of the molecule. In Figure A.6a, we find that the spectra measured at positions I, II and III (and separately at positions IV, V and VI) are equivalent. Like in the case of SCBB, the energy of the Kondo resonance is lower (higher) for the spectra acquired off (on) the symmetry axes of the CBB subunits.

The two Kondo resonances are localized to different areas of the molecules. At their boundaries the resonances overlap. Figure A.7a illustrates this effect. dI/dV spectra acquired at I and III exhibit the typical line shapes discussed in the article. The line shape at position II is different. The red dashed line in Figure A.7a shows a linear combination of spectra I and III (0.4·I + 0.63·III). It matches well with the data from position II.

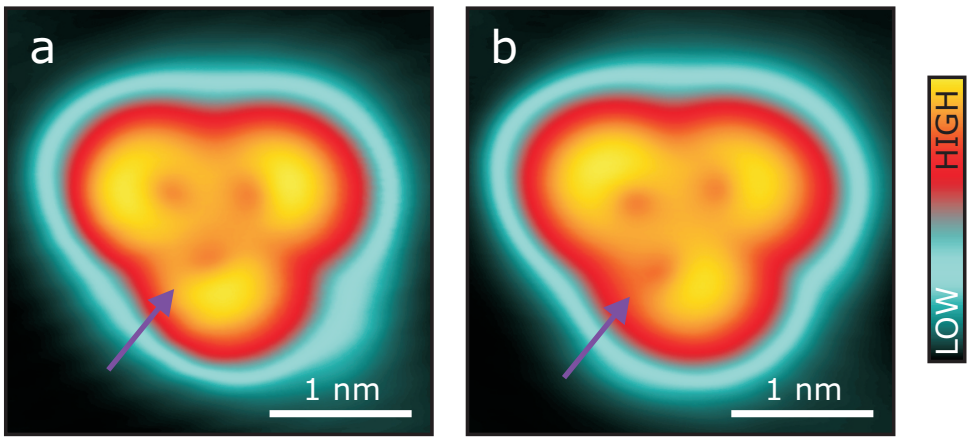

FIGURE A.4: Tilt change of a CBB unit in a single TCBB molecule on Au(111) (a) before and (b) after the corresponding manipulation. The tilt of the CBB unit is inferred from the lateral position of the depression. The manipulation was performed by sweeping the sample voltage from 2 V to −1.5 V (feedback turned off at 2 V and 100 pA).

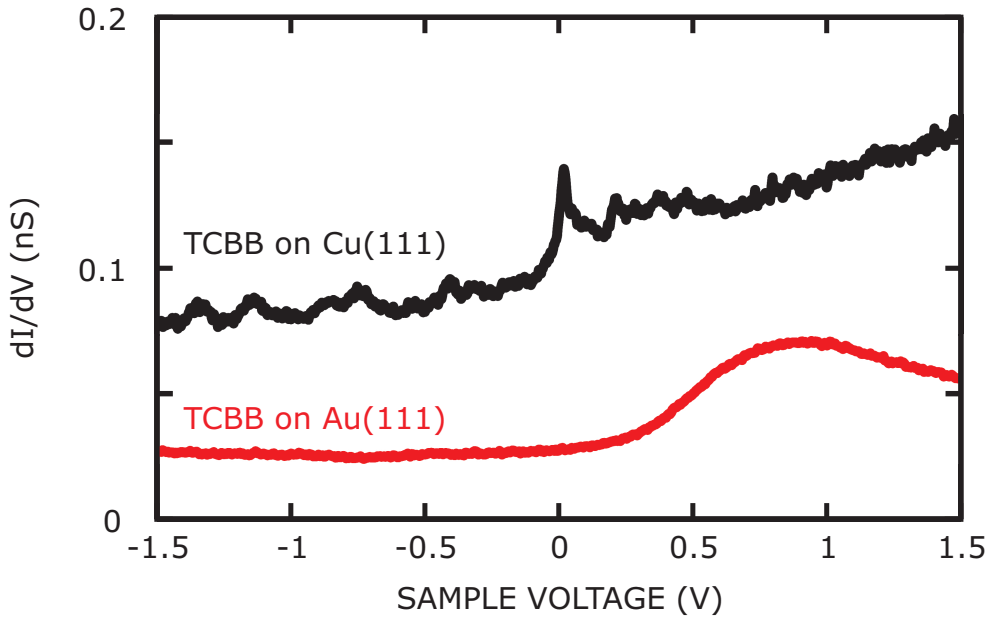

FIGURE A.5: $\mathrm{d}I/\mathrm{d}V$ spectra of TCBB on Cu(111) and TCBB on Au(111). The spectra were acquired above the center of one of the three CBB units using a modulation voltage of 7 mV and 14 mV, respectively. Constant current feedback was opened at $V = 1.5$ V, $I = 100$ pA on Cu(111) and $V = 2.5$ V, $I = 100$ pA on Au(111). The spectra have been vertically shifted by 0.01 and 0.06 nS, respectively.

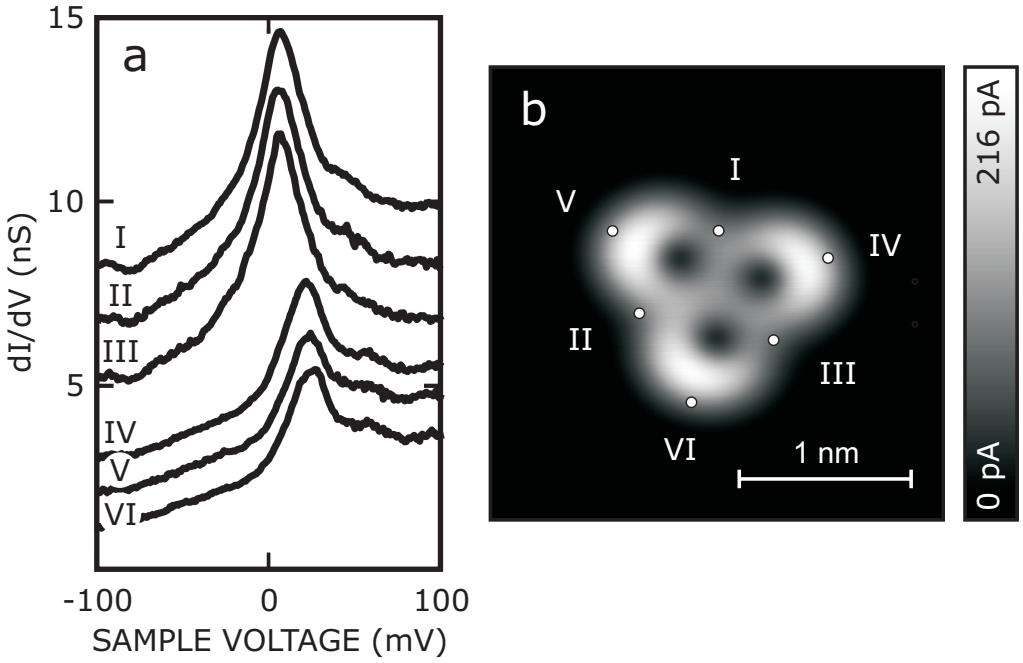

FIGURE A.6: (a) dI/dV spectra of a TCBB molecule on Cu(111) acquired over the TCBB at positions I – VI. Positions IV – VI lie on the symmetry axis of the CBB subunits. Current feedback was disabled at $V = 100$ mV, $I = 400$ pA. The spectra are vertically shifted for clarity. (b) Constant-height STM topograph showing positions of spectroscopic measurements. The topograph was acquired at $V = 100$ mV.

In Chapter 3, the fitting of the Kondo resonance is performed with a Fano function. However, in some cases, a better fit to the experimental data may be realized using a Frota function [118, 122], which has the following expression:

$$\frac{dI}{dV} \approx A \cdot \mathrm{Im}\left[ie^{i\Phi}\sqrt{\frac{i\Gamma}{eV - E_K + i\Gamma}}\right] + B. \tag{A.1}$$

Figure A.8 shows differential-conductance spectra acquired along and off the symmetry axis of a CBB unit, together with fits of Fano and Frota functions. In the present case, the fits of the dI/dV spectra to a Fano function appear qualitatively better than to a Frota function.

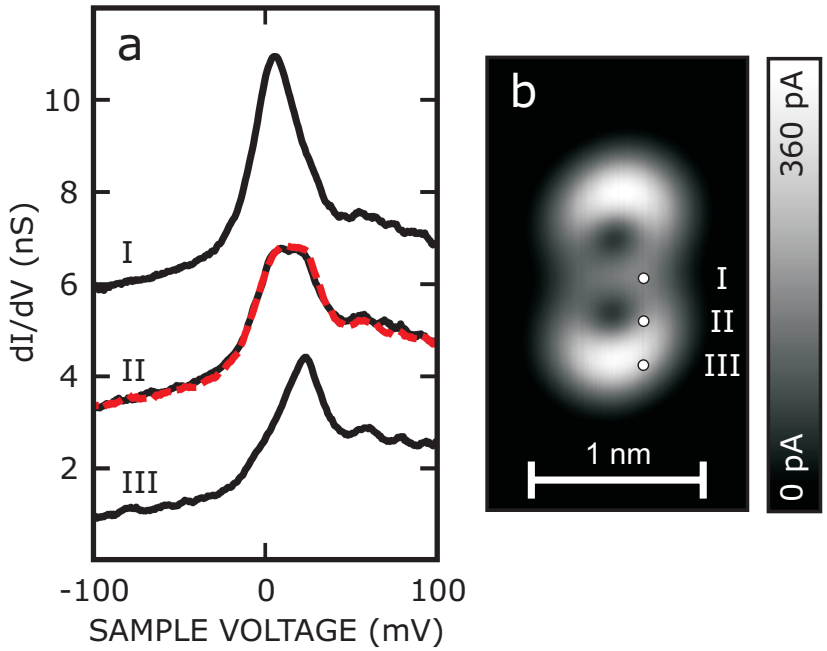

FIGURE A.7: (a) dI/dV spectra over DCBB on Cu(111). The spectra were acquired at three positions over the DCBB (I, II, III). They are vertically shifted for clarity. A linear combination of I and III is shown as a dashed red line. (b) Constant-height STM topograph of a DCBB molecule showing the positions where spectra were recorded. The STM current feedback was disabled at $V = 100$ mV, $I = 300$ pA.

Gas-phase DFT calculations

The gas-phase calculations of TCBB and SCBB molecules were performed using DFT as implemented in Gaussian 09 [175]. Various functionals and the def2TZVP basis set [176] were used and compared. Figure A.9 shows the electronic structure of gas-phase SCBB calculated with four different functionals, namely BP86 [167, 168], B3LYP, [169, 170], PBE [166], and TPSSh [171, 172]. Although the orbital energies vary with the functional, their sequence and their filling are identical for all functionals. In addition, the spatial distributions of the orbitals found with the different functionals coincide. In other words, the functionals lead to identical results for the properties used in our analysis.

Figure A.10a shows the spin-resolved electronic structure of the gas-phase TCBB. There are three degenerate singly-occupied molecular orbitals with a d_{yz} contribution and three degenerate unoccupied orbitals with d_{xz} contribution. The frontier orbitals of TCBB essentially reproduce the orbitals of SCBB three times. This picture is supported by the spatial extension of these orbitals: Figures A.10b and c show top and side views of the calculated isosurfaces of the SOMO and the LUMO, respectively. These orbitals

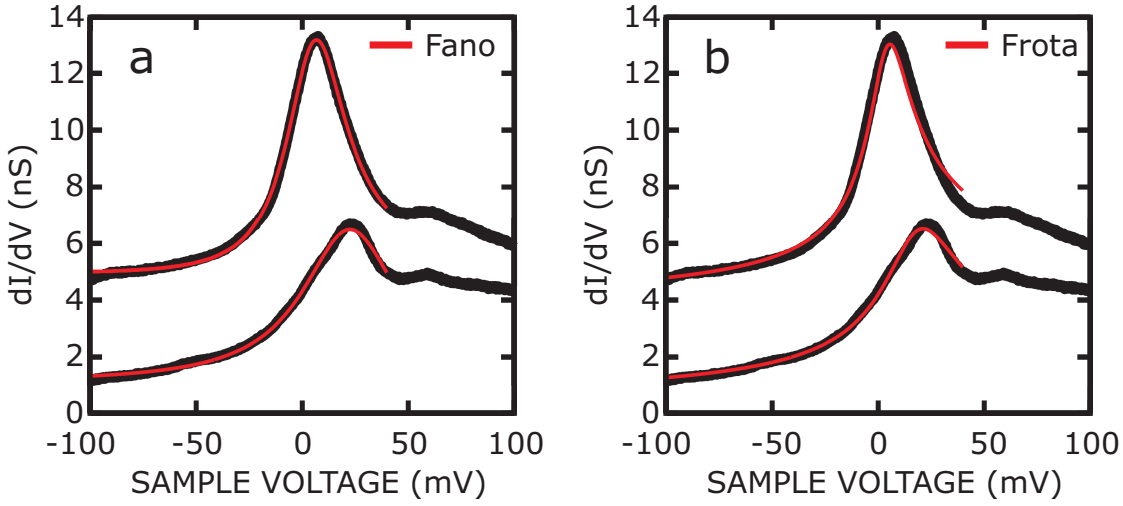

FIGURE A.8: Differential-conductance spectra acquired off (upper curve) and along (lower curve) the symmetry axis of a CBB unit. The red curve corresponds to the best fit using a (a) Fano and (b) Frota function. The resulting fit parameters for the upper (lower) curve are: (a) $T_K = 201$ K ($T_K = 320$ K), $E_K = 5.1$ meV ($E_K = 22.2$ meV), $q = 11$ ($q = 85$) and (b) $\Gamma = 9.4$ meV ($\Gamma = 17.0$ meV), $E_K = 3.8$ meV ($E_K = 17.5$ meV), $\Phi = 0.9$ ($\Phi = 0.9$).

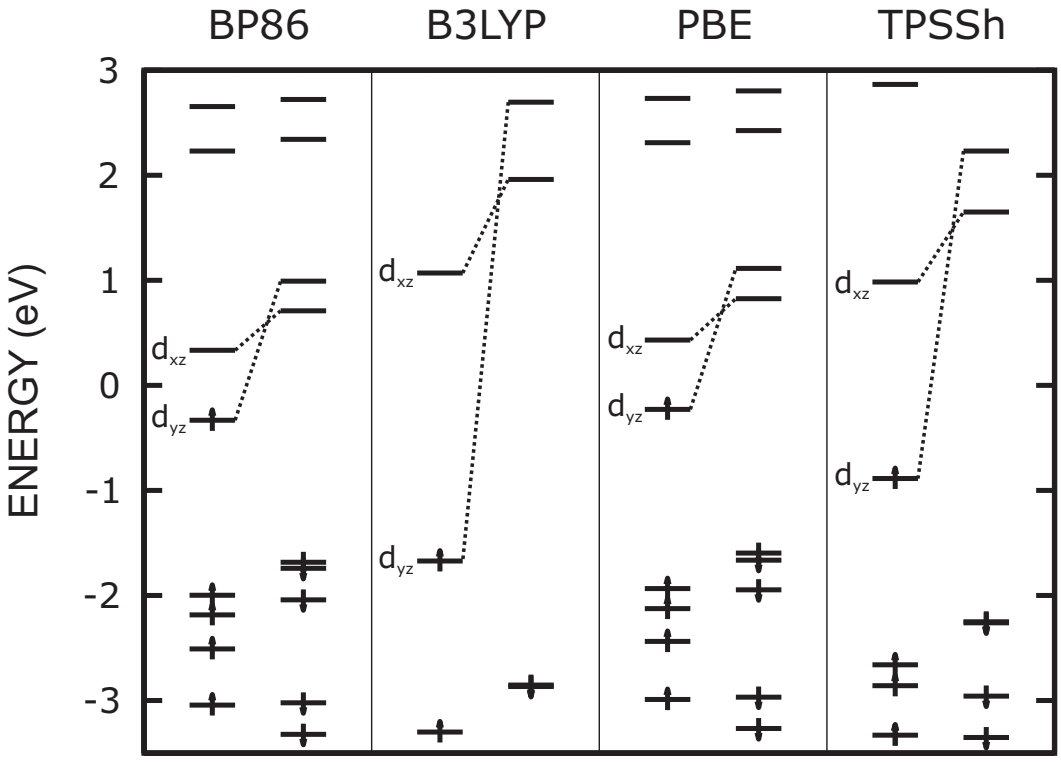

FIGURE A.9: Electronic structure of gas-phase SCBB calculated with four different functionals.

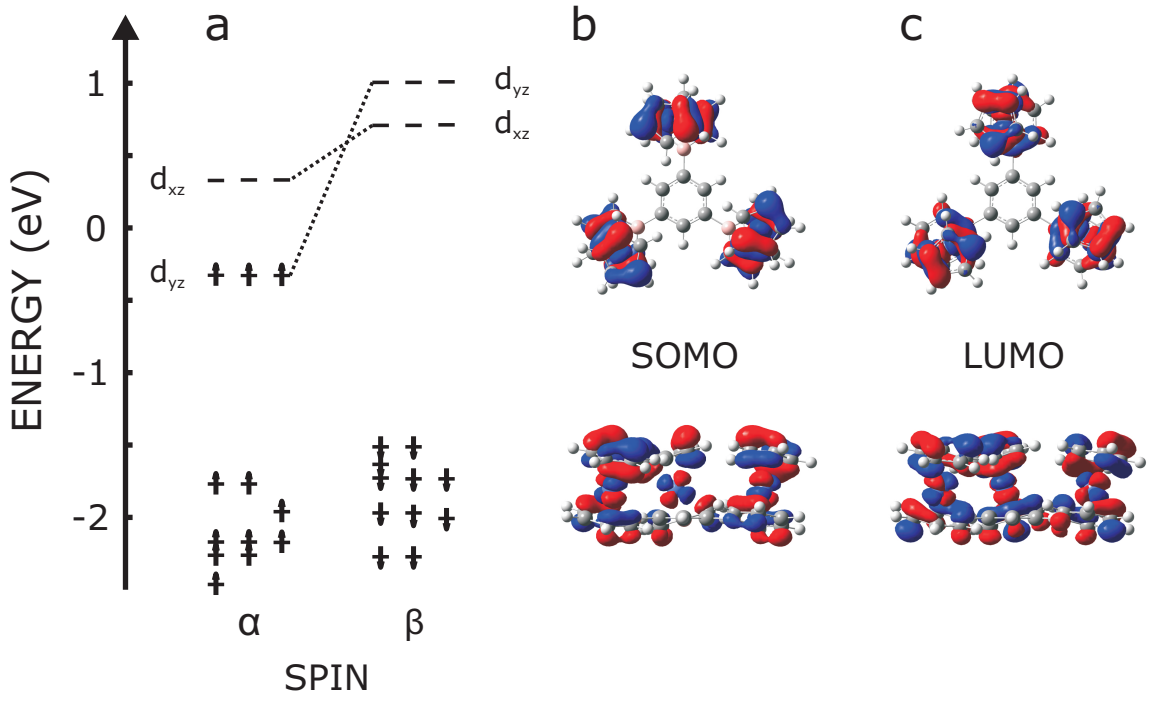

FIGURE A.10: (a) Calculated electronic structure of gas-phase TCBB. Molecular orbitals are labeled according to their *d*-character. (b,c) Top and side view of the calculated wave-function extension of TCBB SOMO and LUMO.

are localized to the CBB units and resemble those calculated for SCBB. Interestingly, the orbitals of the central benzene ring do not contribute to the frontier orbitals of TCBB. This is in line with the picture of TCBB consisting of three decoupled CBB units.

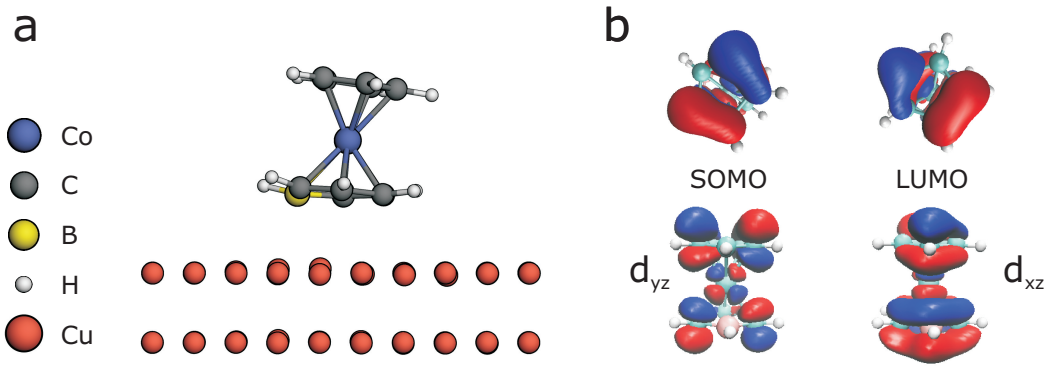

FIGURE A.11: (a) Relaxed geometry of SCBB on Cu(111) obtained from DFT+U calculations. (b) Top and side view of the SOMO and LUMO resulting from gas-phase calculations of the geometry shown in (a).

DFT calculations of SCBB on Cu(111)

DFT + U calculations were performed on SCBB/Cu(111). Two configurations were initially considered: with the borabenzene towards or away from the surface. The configuration with the borabenzene towards the surface (Fig. A.11a) is more stable by approximately 0.2 eV. Therefore, in the following, only this configuration is considered.

The calculations reveal a molecule that is slightly distorted upon adsorption (Fig. A.11a), hereafter referred to as the relaxed molecule, relative to the gas-phase molecule. Interestingly, the upper ring is titled by about 9° relative to the Cu(111) surface, very close to the 8° deduced from the STM topograph. The electronic structure resulting from the calculations extends over the entire system and is rather complex. To extract relevant information from the electronic structure, we project it onto molecular orbitals, in particular to the SOMO and LUMO. However, as a change of geometry may affect the electronic structure, it is important to consider the SOMO and LUMO of the relaxed structure rather than the gas-phase geometry. For this purpose, the relaxed geometry of the molecule (Fig. A.11a) is used as an input geometry of gas-phase calculations, which in turn lead to the SOMO and LUMO presented in Fig. A.11b. The SOMO and LUMO of the relaxed SCBB molecule are very similar to those of the gas-phase SCBB molecule (Fig. 3.3a). In particular, the nodal planes of the orbitals are preserved.

In order to capture the impact of the molecule's adsorption on Cu(111) on the SOMO and LUMO, the electronic structure of SCBB/Cu(111) is separately projected onto the SOMO and LUMO (Fig. A.12). Three main outcomes result from these PDOS. First, upon adsorption, the SOMO and LUMO are spread over a large energy range. This indicates a strong hybridization of the molecular orbitals with those of the substrate. Second, the LUMO, initially unoccupied in the gas-phase, becomes occupied

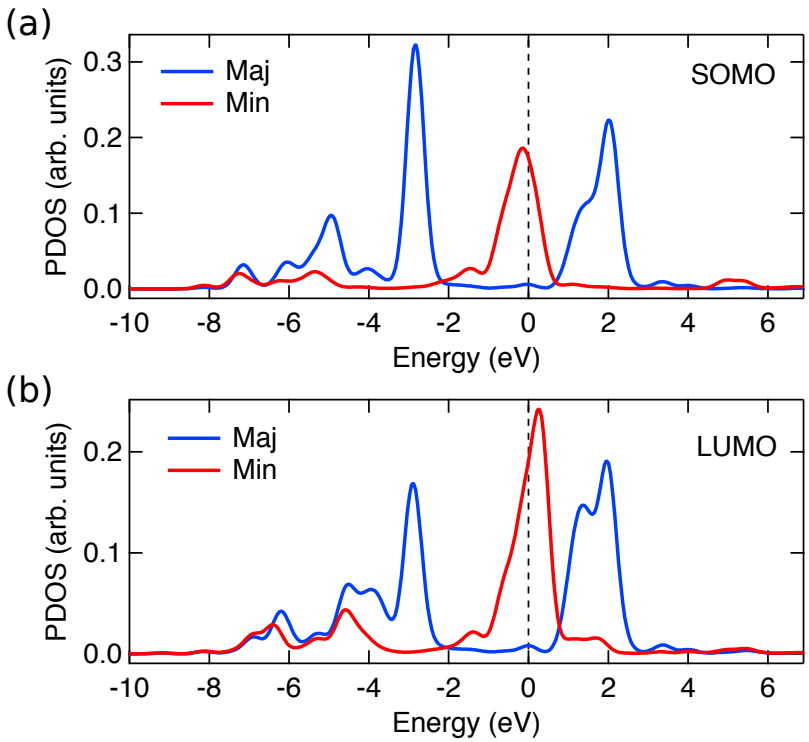

FIGURE A.12: Density of states of SCBB/Cu(111) projected onto the (a) SOMO and (b) LUMO. In addition to the projection, the curves are convoluted with a gaussian function with a width of 0.3 eV.

by approximately one electron. Third, the SOMO and LUMO are both magnetic. In summary, the calculations of SCBB/Cu(111) are consistent with the observation of two Kondo resonances as described in Chapter 3.

B

Supporting information for: Interconnected cobaltocene complexes on metal surfaces

Structure of 1,8-bis(cobaltocenyl)naphthalene

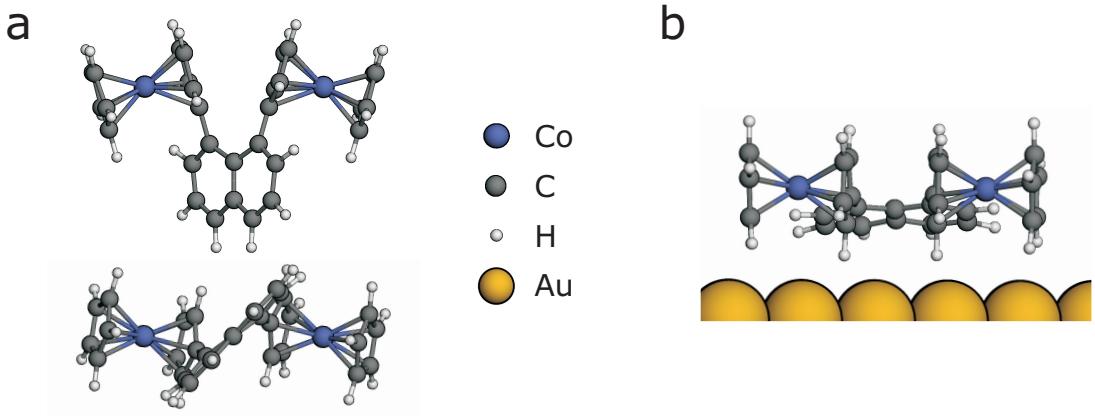

FIGURE B.1: (a) Different views of the calculated gas-phase structure of NBC. (b) Side view of NBC adsorbed on Au(111). The planar adsorption of the naphthalene induces an horizontal orientation of the cobaltocene units.

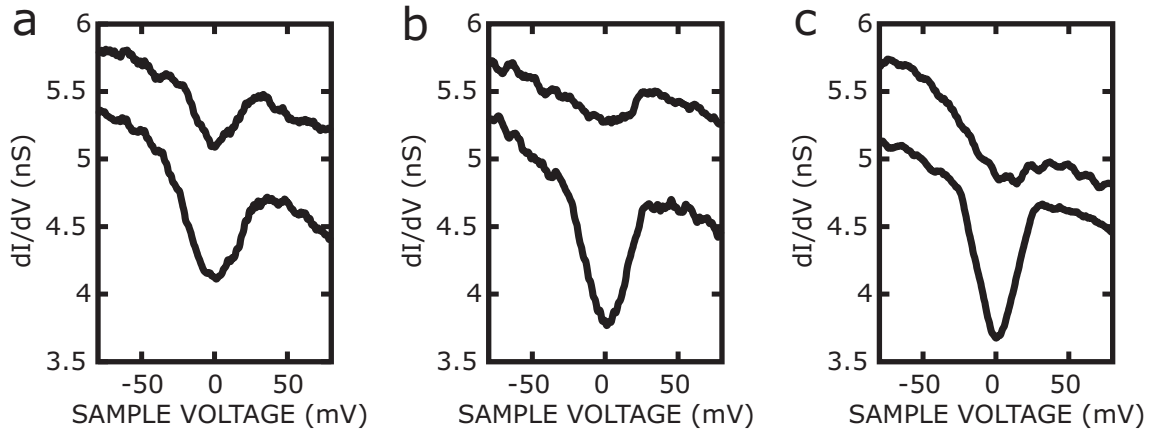

FIGURE B.2: (a–c) $\mathrm{d}I/\mathrm{d}V$ spectra of three NBC molecules on Au(111). Each panel shows two spectra acquired over the two cobaltocene units of a single NBC molecule. The STM current feedback was disabled at $V = -100$ mV and $I = 1$ nA. The spectra are vertically shifted for clarity.

Figure B.1a shows the gas-phase structure of 1,8-bis(cobaltocenyl)naphthalene (NBC) calculated within DFT. NBC molecules are composed of two cobaltocene units connected by a naphthalene clamp. The naphthalene causes a head-to-head arrangement of the metallocene subunits. The calculations reproduce the molecular structure inferred from X-ray diffraction data [173, 286].

According to our scanning tunneling microscopy data, the NBC molecules adopt a different structure on Au(111). The naphthalene plane appears to be parallel to the surface, and in turn parallel to the cobaltocene units. Figure B.1b illustrates this geometry by a schematic side view of NBC on Au(111).

Scanning tunneling spectra of NBC on Au(111)

Figure B.2 shows typical differential-conductance spectra of three NBC molecules within a molecular chain. The spectra were acquired atop the expected cobaltocene positions. The two cobaltocene units belonging to the same NBC molecule exhibit dips (pressumed to be Kondo resonances) with different amplitudes.

Deposition and mass spectra of 1,3,5-tris(cobaltocenyl)benzene

For the deposition of 1,3,5-tris(cobaltocenyl)benzene (BTC) molecules (calculated mass 639 u, Fig. B.3a) on Cu(111) an *in situ* ultrahigh-vacuum electrospray ionization setup with mass selection was used [214]. Stable spray conditions were achieved with $\mathrm{BTC}(\mathrm{BF}_4)_3$ molecules dissolved in nitromethane. Prior to deposition, the BTC ion beam was analyzed by an in-line quadrupole mass spectrometer. Figure B.3b shows

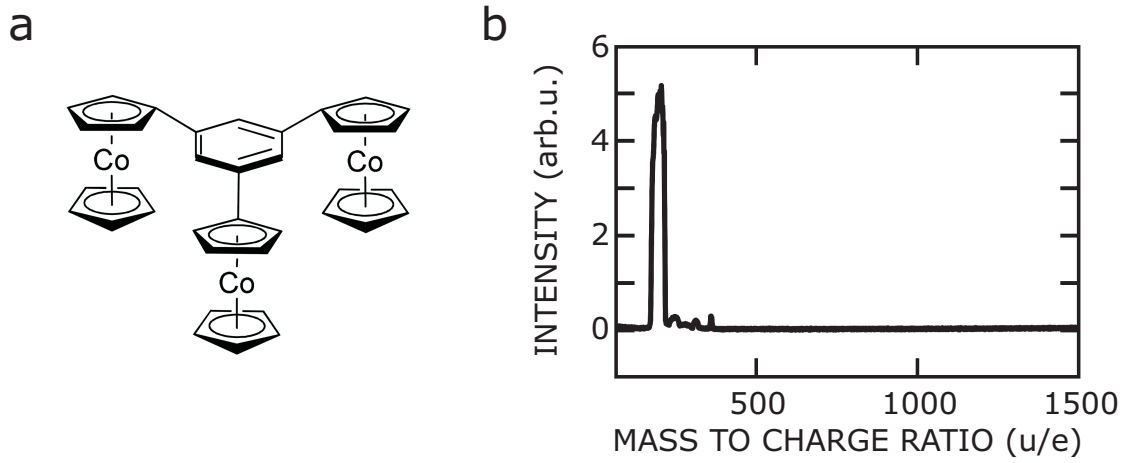

FIGURE B.3: (a) Schematic structure of BTC. (b) Mass spectrum of electrosprayed BTC ions.

a typical mass spectrum. A single peak corresponding to intact triply charged BTC molecules (213 u/e) is observed. The deposition of BTC molecules on Cu(111) was performed by selecting a mass-to-charge ratio of 213 u/e at a kinetic energy of 9 eV. The ion current at the sample was used to monitor the deposited amount of BTC. During the deposition onto a Cu(111) surface held at room temperature the pressure was kept below 2×10^{-9} mbar.

Molecular orbitals

Figure B.4 shows the structure, HOMO, and LUMO of the NBC, NTC and BTC complexes. The HOMO and LUMO are mostly localized on the cobaltocene units.

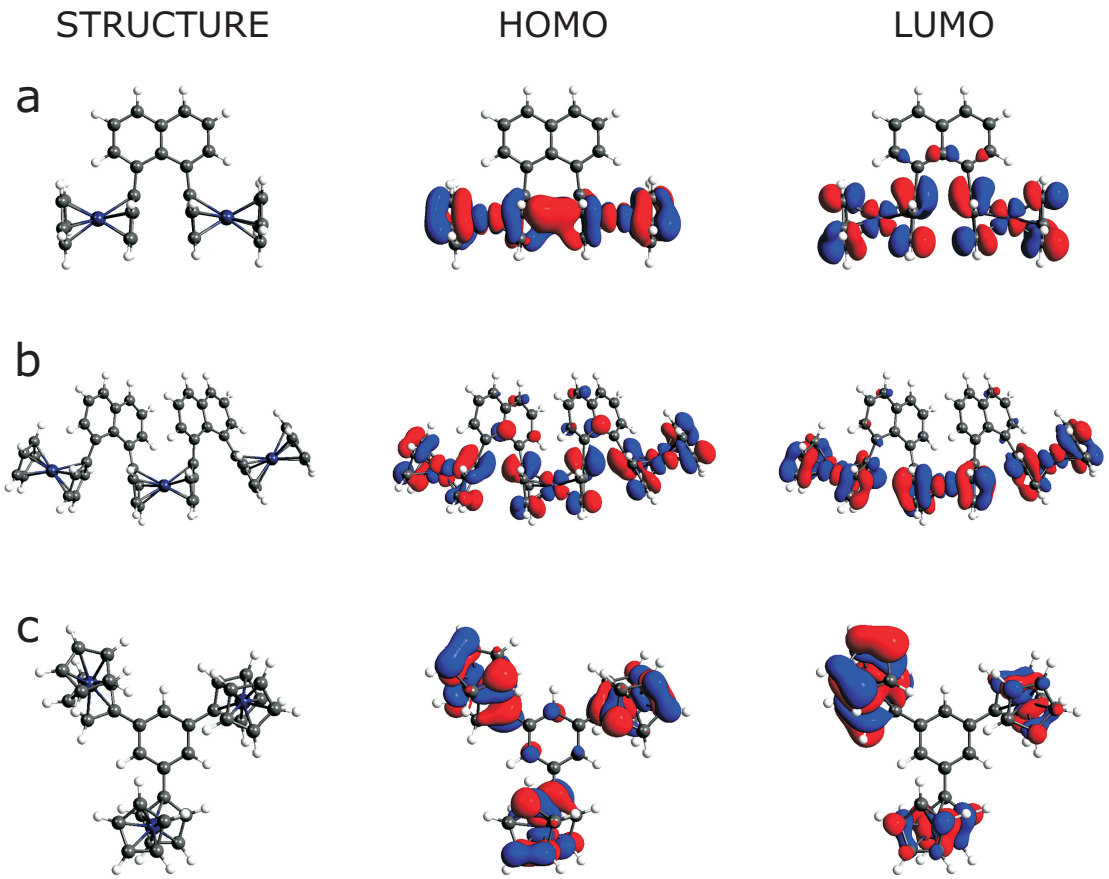

FIGURE B.4: (a) Schematic structure, HOMO and LUMO of the (a) NBC, (b) NTC and (c) BTC complexes.

C

Supporting information for: Surface cis effect: Influence of an Axial Ligand on Molecular Self-Assembly

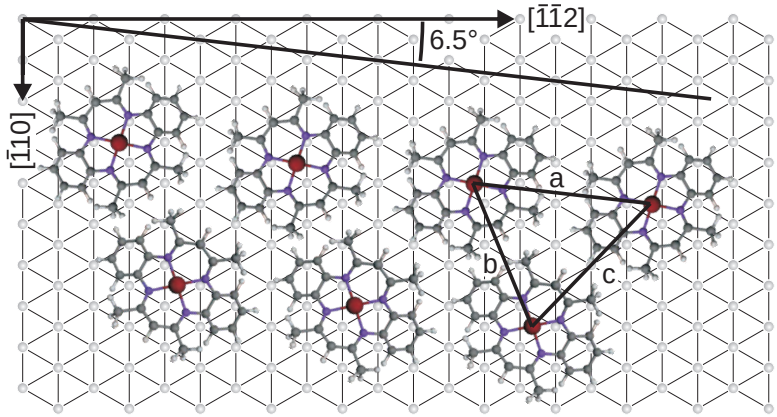

FIGURE C.1: Model of FeTMTAA chain.

Model of FeTMTAA chain at elevated coverage

From an analysis of many STM images, the following geometrical parameters were determined: Intermolecular distances $a = 12.3 \pm 0.5$ Å, $b = 10.9 \pm 0.5$ Å, and

$c = 12.2 \pm 0.5$ Å; the angle $\phi = 6 \pm 1°$ between the chain direction and $\langle 112 \rangle$ directions of the substrate; the alignment of the long axis of the molecules along $\langle 110 \rangle$ directions of the Au(111) surface. In Figure C.1, we propose a model of the observed pattern that takes these parameters into account. In the model, we find $a = 12.6$ Å, $b = 10.9$ Å, $c = 12.0$ Å, and $\phi = 6.5°$.

Model of CO-FeTMTAA chain at elevated coverage

From an analysis of many STM images, the following geometrical parameters were determined: Intermolecular distance $a = 11.0 \pm 0.5$ Å; the angle $\phi = 4 \pm 1°$ between the chain direction and $\langle 112 \rangle$ directions; the alignment of the long axis of the molecules along $\langle 110 \rangle$ directions of the Au(111) surface. In Figure C.2, we propose a model of the observed pattern that takes these parameters into account. In the model, we find $a = 11.3$ Å, and $\phi = 3.6°$. In this arrangement, steric repulsion is reduced by maximizing the distance between hydrogen atoms of methyl and phenyl functionalities.

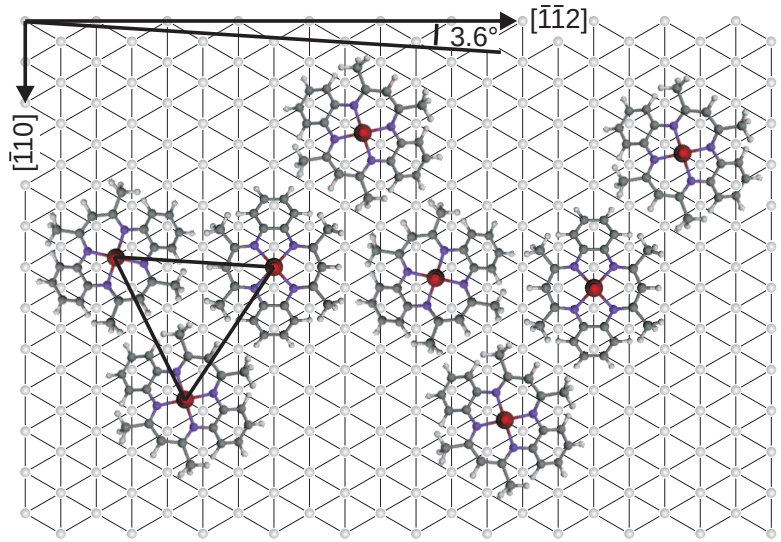

FIGURE C.2: Model of CO-FeTMTAA chain.

STM image of complete monolayer of FeTMTAA

Figure C.3 shows a constant-current image of the highest density structure of a FeTMTAA monolayer we observed. Single molecules are indicated by elongated hexagons. We use this structure to define 1 monolayer as a density of 1 nm^{-2}.

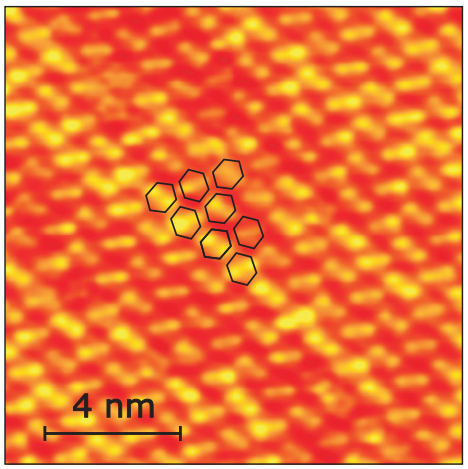

FIGURE C.3: Complete monolayer of FeTMTAA.

Calculated frontier orbitals in the gas-phase

Figure C.4 shows the spin-resolved electronic structure of FeTMTAA, NiTMTAA, and CO-FeTMTAA. The *d*-orbitals of the metal centers mix with the frontier orbitals of the ligands. We nevertheless labelled five molecular orbitals with large *d*-character. The FeTMTAA molecule has a spin state $S = 1$ with unpaired electrons in the d_{z^2} and d_{yz} orbitals. These half-filled orbitals are expected to mediate bonding to the Au surface. Upon coordination with CO the d_{z^2} orbital is pushed higher in energy and becomes unoccupied. Because the d_{yz} orbital is twofold occupied, CO-FeTMTAA is in a $S = 0$ spin state, similar to NiTMTAA.

The results shown were obtained using Gaussian 09 using a BP86 functional and a def2TZVP basis set. However, qualitatively similar results were obtained with a range of functionals, namely B3LYP, TPSSh, and PBE, which cover varying degrees of Hartree-Fock exchange. In particular, all calculations predict the same occupancies of *d*-orbitals.

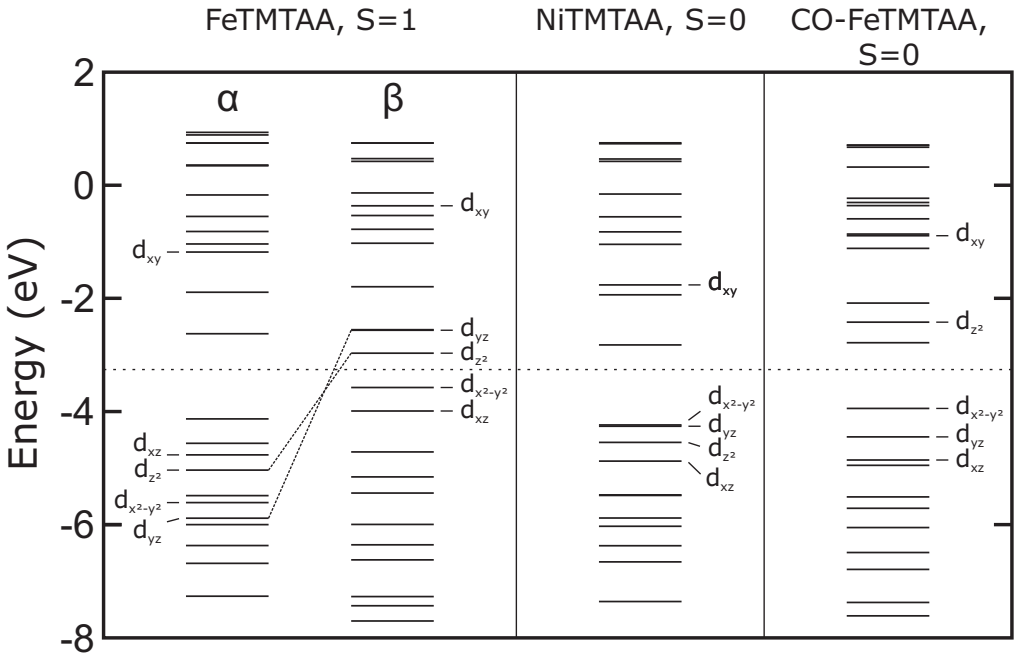

FIGURE C.4: Calculated electronic structure of gas-phase FeTMTAA, NiTMTAA, and CO-FeTMTAA.

Density of states of CO-FeTMTAA

PDOS on the *d*-manifold of Fe in the CO-FeTMTAA molecules is depicted in Figure C.5a. The *d*-manifold of Fe plays an important role in the frontier-orbital composition. By studying the electronic structure projected on the *d*-orbitals of Fe, direct information on the adsorption of the molecule can be obtained. Upon adsorption of a CO molecule, the spin of the molecule disappears and no difference between the electronic structure for both spins is found. The adsorption on the surface leads to some broadening of the density of states as can be seen in the figure by comparing the PDOS on the gas-phase molecule (free) and the adsorbed one. The addition of CO shifts the occupied levels to the Fermi energy, in good agreement with the measured shift of the negative-energy electronic structure in the $\mathrm{d}I/\mathrm{d}V$ spectra of Figure 5.3.

Electronic structure of NiTMTAA

Ni(II) in NiTMTAA has no spin due to its d^8 configuration in the ligand field of the molecule (Fig. C.5b). The density of states projected on the *d*-manifold of Ni shows clearly this because there is no difference between both spins in the electronic structure. Most astonishing is the resemblance of the PDOS of NiTMTAA adsorbed on Au(111) with the one obtained for CO-FeTMTAA, as displayed in Fig. C.5a. At first sight the electronic structures are very much similar, showing that the correspondence

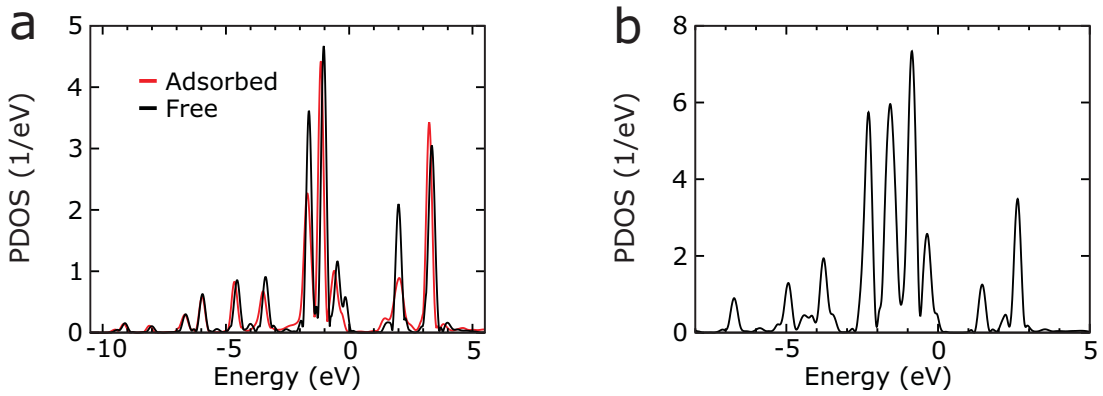

FIGURE C.5: (a) Projected DOS on the *d*-manifold of Fe in the CO-FeTMTAA. (b) Projected density of states on the *d*-manifold of Ni in NiTMTAA.

between both molecules is not fortuitous and in good agreement with the experimental measurements of Figure 5.3.

D

Supporting information for: Iron terpyridine complexes on Au(111)

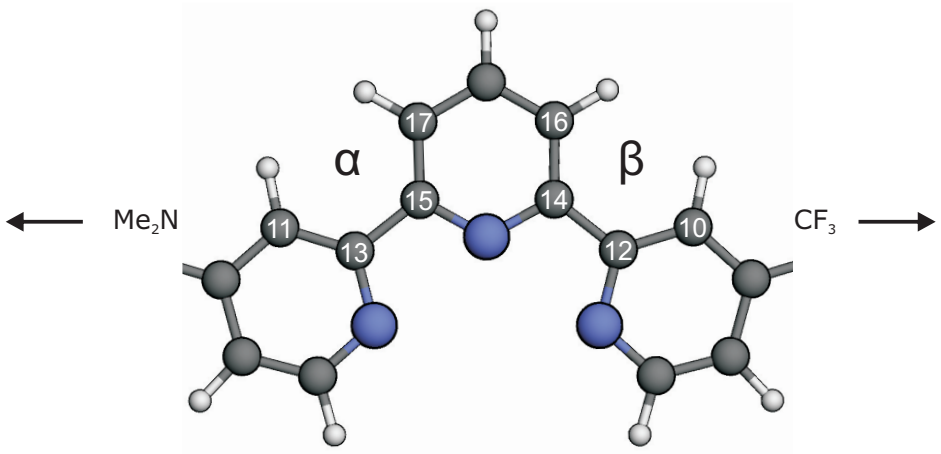

FIGURE D.1: The rotation angles between the adjacent pyridine units, α and β, are defined as the dihedral angles of the carbon atoms 11, 13, 15, 17 and 10, 12, 14, 16, respectively.

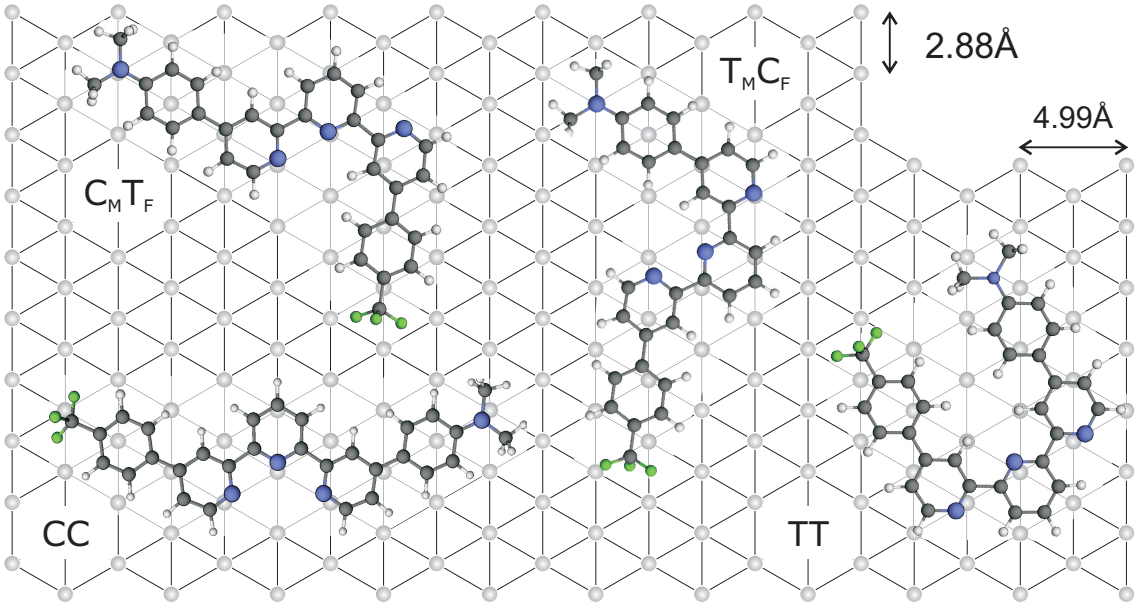

FIGURE D.2: Possible adsorption geometries of tpy ligands in different conformations on Au(111). For this arrangement, calculated gas-phase structures of the tpy ligand were placed on a model of the Au(111) surface.

List of Abbreviations

AFM	Atomic Force Microscope / Microscopy
BPY	Bipyridine
BPZ	Dihydrobis(pyrazolyl)borate
CBB	η^6-borabenzene-η^5-cyclopentadienylcobalt
$CoCp_2$	Cobaltocene
Cp	Cyclopentadienyl
DC	Direct Current
DFT	Density Functional Theory
DOS	Density of States
ESI	Electrospray Ionization
FCC	Face-Centered Cubic
FWHM	Full-Width at Half-Maximum
GGA	Generalized Gradient Approximation
HCP	Hexagonal Close-Packed
HOMO	Highest Occupied Molecular Orbital
HOPG	Highly Oriented Pyrolytic Graphite
HS	High-Spin
HWHM	Half-Width at Half-Maximum
LDA	Local Density Approximation
LDOS	Local Density of States
LS	Low-Spin
LT	Low-Temperature
LUMO	Lowest Occupied Molecular Orbital
MCBJ	Mechanically Controlled Break Junction
ML	Monolayer
NRG	Numerical-Normalization Group
PAW	Projected Augmented Wave
PDOS	Projected Density of States
PES	Potential Energy Surface
PHEN	1,10-phenanthroline
RF	Radio Frequency
RT	Room Temperature
SCO	Spin-Crossover
SOMO	Singly Occupied Molecular Orbital

SP ..... Spin-Polarized
STM ..... Scanning Tunneling Microscope / Microscopy
STS ..... Scanning Tunneling Spectroscopy
TMTAA ..... Tetramethyl-Tetraazaannulene
TPY ..... Terpyridine
UHV ..... Ultrahigh Vacuum
WKB ..... Wentzel-Kramers-Brillouin

Bibliography

[1] A. Aviram and M. A. Ratner. *Molecular rectifiers.* Chem. Phys. Lett. **29**, 277 (1974).

[2] C. Joachim, J. K. Gimzewski, and A. Aviram. *Electronics using hybrid-molecular and mono-molecular devices.* Nature **408**, 541 (2000).

[3] S. V. Aradhya and L. Venkataraman. *Single-molecule junctions beyond electronic transport.* Nat. Nanotechnol. **8**, 399 (2013).

[4] Editorial. *Does molecular electronics compute?* Nat. Nanotechnol. **8**, 377 (2013).

[5] E. Lörtscher. *Wiring molecules into circuits.* Nat. Nanotechnol. **8**, 381 (2013).

[6] R. M. Metzger. *Unimolecular Electronics.* Chem. Rev. **115**, 5056 (2015).

[7] D. Xiang, X. Wang, C. Jia, T. Lee, and X. Guo. *Molecular-Scale Electronics: From Concept to Function.* Chem. Rev. **116**, 4318 (2016).

[8] H. Jeong, D. Kim, D. Xiang, and T. Lee. *High-Yield Functional Molecular Electronic Devices.* ACS Nano **11**, 6511 (2017).

[9] J. C. Cuevas and E. Scheer. *Molecular Electronics. An Introduction to Theory and Experiment.* (World Scientific Publishing Co. Pte. Ltd., London, 2010).

[10] S. J. Higgins, R. J. Nichols, S. Martin, P. Cea, H. S. J. van der Zant, M. M. Richter, and P. J. Low. *Looking Ahead: Challenges and Opportunities in Organometallic Chemistry.* Organometallics **30**, 7 (2011).

[11] J. M. Tour. *Molecular Electronics. Commercial Insights, Chemistry, Devices, Architecture and Programming.* (World Scientific Publishing Co. Pte. Ltd., London, 2003).

[12] P. Liljeroth, J. Repp, and G. Meyer. *Current-Induced Hydrogen Tautomerization and Conductance Switching of Naphthalocyanine Molecules.* Science **317**, 1203 (2007).

[13] S. Y. Quek, M. Kamenetska, M. L. Steigerwald, H. J. Choi, S. G. Louie, M. S. Hybertsen, J. B. Neaton, and L. Venkataraman. *Mechanically controlled binary conductance switching of a single-molecule junction.* Nat. Nanotechnol. **4**, 230 (2009).

[14] S. Jan van der Molen and P. Liljeroth. *Charge Transport through Molecular Switches.* J. Phys.: Condens. Matter **22**, 133001 (2010).

[15] W. Auwärter, K. Seufert, F. Bischoff, D. Ecija, S. Vijayaraghavan, S. Joshi, F. Klappenberger, N. Samudrala, and J. V. Barth. *A surface-anchored molecular four-level conductance switch based on single proton transfer.* Nat. Nanotechnol. **7**, 41 (2011).

[16] R. Frisenda, G. D. Harzmann, J. A. Celis Gil, J. M. Thijssen, M. Mayor, and H. S. J. van der Zant. *Stretching-Induced Conductance Increase in a Spin-Crossover Molecule.* Nano Lett. **16**, 4733 (2016).

[17] T. Miyamachi, M. Gruber, V. Davesne, M. Bowen, S. Boukari, L. Joly, F. Scheurer, G. Rogez, T. K. Yamada, P. Ohresser, E. Beaurepaire, and W. Wulfhekel. *Robust Spin Crossover and Memristance Across a Single Molecule.* Nat. Commun. **3**, 938 (2012).

[18] A. Stróżecka, M. Soriano, J. I. Pascual, and J. J. Palacios. *Reversible Change of the Spin State in a Manganese Phthalocyanine by Coordination of CO Molecule.* Phys. Rev. Lett. **109**, 147202 (2012).

[19] T. G. Gopakumar, F. Matino, H. Naggert, A. Bannwarth, F. Tuczek, and R. Berndt. *Electron-Induced Spin Crossover of Single Molecules in a Bilayer on Gold.* Angew. Chem., Int. Ed. **51**, 6262 (2012).

[20] L. Liu, K. Yang, Y. Jiang, B. Song, W. Xiao, L. Li, H. Zhou, Y. Wang, S. Du, M. Ouyang, W. A. Hofer, A. H. Castro Neto, and H.-J. Gao. *Reversible Single Spin Control of Individual Magnetic Molecule by Hydrogen Atom Adsorption.* Sci. Rep. **3**, 1210 (2013).

[21] A. Batra, P. Darancet, Q. Chen, J. S. Meisner, J. R. Widawsky, J. B. Neaton, C. Nuckolls, and L. Venkataraman. *Tuning Rectification in Single-Molecular Diodes.* Nano Lett. **13**, 6233 (2013).

[22] B. Capozzi, J. Xia, O. Adak, E. J. Dell, Z.-F. Liu, J. C. Taylor, J. B. Neaton, L. M. Campos, and L. Venkataraman. *Single-molecule diodes with high rectification ratios through environmental control.* Nat. Nanotechnol. **10**, 522 (2015).

[23] Q. v. Nguyen, P. Martin, D. Frath, M. L. Della Rocca, F. Lafolet, C. Barraud, P. Lafarge, V. Mukundan, D. James, R. L. McCreery, and J.-C. Lacroix. *Control of Rectification in Molecular Junctions: Contact Effects and Molecular Signature.* J. Am. Chem. Soc. **139**, 11913 (2017).

[24] X. H. Qiu, G. V. Nazin, and W. Ho. *Vibrationally Resolved Fluorescence Excited with Submolecular Precision.* Science **299**, 542 (2003).

[25] Z.-C. Dong, X.-L. Guo, A. S. Trifonov, P. S. Dorozhkin, K. Miki, K. Kimura, S. Yokoyama, and S. Mashiko. *Vibrationally Resolved Fluorescence from Organic Molecules near Metal Surfaces in a Scanning Tunneling Microscope.* Phys. Rev. Lett. **92**, 086801 (2004).

[26] S. Mühlenberend, N. L. Schneider, M. Gruyters, and R. Berndt. *Plasmon-induced fluorescence and electroluminescence from porphine molecules on GaAs(110) in a scanning tunneling microscope.* Appl. Phys. Lett. **101**, 203107 (2012).

[27] M. C. Chong, G. Reecht, H. Bulou, A. Boeglin, F. Scheurer, F. Mathevet, and G. Schull. *Narrow-Line Single-Molecule Transducer between Electronic Circuits and Surface Plasmons.* Phys. Rev. Lett. **116**, 036802 (2016).

[28] K. Kuhnke, C. Große, P. Merino, and K. Kern. *Atomic-Scale Imaging and Spectroscopy of Electroluminescence at Molecular Interfaces.* Chem. Rev. **117**, 5174 (2017).

[29] B. Doppagne, M. C. Chong, E. Lorchat, S. Berciaud, M. Romeo, H. Bulou, A. Boeglin, F. Scheurer, and G. Schull. *Vibronic Spectroscopy with Submolecular Resolution from STM-Induced Electroluminescence.* Phys. Rev. Lett. **118**, 127401 (2017).

[30] C. Chen. *Introduction to Scanning Tunneling Microscopy* (Oxford University Press, New York, 2nd edition, 2008).

[31] D. Bonnell. *Scanning Probe Microscopy and Spectroscopy. Theory, Techniques, and Applications.* (Wiley-VCH, New York, United States, 2nd edition, 2001).

[32] R. Wiesendanger. *Scanning Probe Microscopy and Spectroscopy. Methods and Applications* (Cambridge University Press, Cambridge, United Kingdom, 1994).

[33] E. Meyer, H. J. Hug, and R. Bennewitz. *Scanning Probe Microscopy. The Lab on a Tip.* (Springer-Verlag, Heidelberg, 2004).

[34] E. L. Wolf. *Principles of Electron Tunneling Spectroscopy* (Oxford University Press, New York, 2nd edition, 2012).

[35] B. Voigtländer. *Scanning Probe Microscopy. Atomic Force Microscopy and Scanning Tunneling Microscopy.* (Springer-Verlag, Heidelberg, 2015).

[36] R. H. Crabtree. *The Organometallic Chemistry of the Transition Metals* (John Wiley & Sons, Inc., 1988).

[37] R. Schuhmann. *Scanning probe microscopy: From sublime to ubiquitous.* `https://journals.aps.org/prl/scanning-probe-microscopy` (2016).

[38] *Press release: The Nobel prize in Physics 1986*. http://www.nobelprize.org/nobel_prizes/physics/laureates/1986/press.html. 15. October 1986.

[39] G. Binnig, H. Rohrer, C. Gerber, and E. Weibel. *Surface Studies by Scanning Tunneling Microscopy*. Phys. Rev. Lett **49**, 57 (1982).

[40] G. Binnig, H. Rohrer, C. Gerber, and E. Weibel. *Tunneling through a controllable vacuum gap*. Appl. Phys. Lett. **40**, 178 (1982).

[41] S. Chiang. *Scanning tunneling microscopy imaging of small adsorbed molecules on metal surfaces in an ultrahigh vacuum environment*. Chem. Rev. **97**, 1083 (1997).

[42] J. K. Gimzewski and C. Joachim. *Nanoscale science of single molecules using local probes*. Science **283**, 1683 (1999).

[43] G. Binnig, C. F. Quate, and C. Gerber. *Atomic force microscope*. Phys. Rev. Lett. **56**, 930 (1986).

[44] F. J. Giessibl. *Advances in atomic force microscopy*. Rev. Mod. Phys. **75**, 949 (2003).

[45] L. Gross, F. Mohn, N. Moll, P. Liljeroth, and G. Meyer. *The Chemical Structure of a Molecule Resolved by Atomic Force Microscopy*. Science **325**, 1110 (2009).

[46] L. Gross, F. Mohn, N. Moll, G. Meyer, R. Ebel, W. M. Abdel-Mageed, and M. Jaspars. *Organic structure determination using atomic-resolution scanning probe microscopy*. Nat. Chem. **2**, 821 (2010).

[47] K. Ø. Hanssen, B. Schuler, A. J. Williams, T. B. Demissie, E. Hansen, J. H. Andersen, J. Svenson, K. Blinov, M. Repisky, F. Mohn, G. Meyer, J.-S. Svendsen, K. Ruud, M. Elyashberg, L. Gross, M. Jaspars, and J. Isaksson. *A Combined Atomic Force Microscopy and Computational Approach for the Structural Elucidation of Breitfussin A and B: Highly Modified Halogenated Dipeptides from Thuiaria breitfussi*. Angew. Chem. Int. Ed. **51**, 12238 (2012).

[48] B. Schuler, G. Meyer, D. Peña, O. C. Mullins, and L. Gross. *Unraveling the Molecular Structures of Asphaltenes by Atomic Force Microscopy*. J. Am. Chem. Soc. **137**, 9870 (2015).

[49] P. Jelínek. *High resolution SPM imaging of organic molecules with functionalized tips*. J. Phys.: Condens. Matter **29**, 343002 (2017).

[50] B. de la Torre, M. Švec, G. Foti, O. Krejčí, P. Hapala, A. Garcia-Lekue, T. Frederiksen, R. Zbořil, A. Arnau, H. Vázquez, and P. Jelínek. *Submolecular Resolution by Variation of the Inelastic Electron Tunneling Spectroscopy Amplitude and its Relation to the AFM/STM Signal*. Phys. Rev. Lett. **119**, 166001 (2017).

[51] J. Repp, G. Meyer, S. M. Stojković, A. Gourdon, and C. Joachim. *Molecules on Insulating Films: Scanning-Tunneling Microscopy Imaging of Individual Molecular Orbitals.* Phys. Rev. Lett. **94** (2005).

[52] T. L. Cocker, D. Peller, P. Yu, J. Repp, and R. Huber. *Tracking the ultrafast motion of a single molecule by femtosecond orbital imaging.* Nature **539**, 263 (2016).

[53] C. Iacovita, M. Rastei, B. Heinrich, T. Brumme, J. Kortus, L. Limot, and J. Bucher. *Visualizing the Spin of Individual Cobalt-Phthalocyanine Molecules.* Phys. Rev. Lett. **101**, 116602 (2008).

[54] A. Zhao, Q. Li, L. Chen, H. Xiang, W. Wang, S. Pan, B. Wang, X. Xiao, J. Yang, J. G. Hou, and Q. Zhu. *Controlling the Kondo Effect of an Adsorbed Magnetic Ion Through Its Chemical Bonding.* Science **309**, 1542 (2005).

[55] J. Brede and R. Wiesendanger. *Spin-resolved imaging and spectroscopy of individual molecules with sub-molecular spatial resolution.* MRS Bull. **39**, 608 (2014).

[56] D. M. Eigler and E. K. Schweizer. *Positioning single atoms with a scanning tunnelling microscope.* Nature **344**, 524 (1990).

[57] Y. Zhang, Y. Wang, J.-T. Lü, M. Brandbyge, and R. Berndt. *Mechanochemistry Induced Using Force Exerted by a Functionalized Microscope Tip.* Angew. Chem. Int. Ed. **56**, 11769 (2017).

[58] N. Ballav, C. Wäckerlin, D. Siewert, P. M. Oppeneer, and T. A. Jung. *Emergence of On-Surface Magnetochemistry.* J. Phys. Chem. Lett. **4**, 2303 (2013).

[59] B. Schuler, S. Collazos, L. Gross, G. Meyer, D. Pérez, E. Guitián, and D. Peña. *From Perylene to a 22-Ring Aromatic Hydrocarbon in One-Pot.* Angew. Chem. Int. Ed. **53**, 9004 (2014).

[60] J. M. Gottfried. *Surface chemistry of porphyrins and phthalocyanines.* Surf. Sci. Rep. **70**, 259 (2015).

[61] Q. Shen, H.-Y. Gao, and H. Fuchs. *Frontiers of on-surface synthesis: From principles to applications.* Nano Today **13**, 77 (2017).

[62] B. C. Stipe, M. A. Rezaei, and W. Ho. *Single-Molecule Vibrational Spectroscopy and Microscopy.* Science **280**, 1732 (1998).

[63] E. Ćavar, M.-C. Blüm, M. Pivetta, F. Patthey, M. Chergui, and W.-D. Schneider. *Fluorescence and Phosphorescence from Individual C_{60} Molecules Excited by Local Electron Tunneling.* Phys. Rev. Lett. **95**, 196102 (2005).

[64] F. Mohn, L. Gross, N. Moll, and G. Meyer. *Imaging the charge distribution within a single molecule.* Nat. Nanotechnol. **7**, 227 (2012).

[65] V. Balzani, A. Credi, and M. Venturi. *Molecular Devices and Machines* (Wiley-VCH Verlag, Weinheim, 2003).

[66] S. Erbas-Cakmak, D. A. Leigh, C. T. McTernan, and A. L. Nussbaumer. *Artificial Molecular Machines.* Chem. Rev. **115**, 10081 (2015).

[67] A. Burtzlaff, A. Weismann, M. Brandbyge, and R. Berndt. *Shot Noise as a Probe of Spin-Polarized Transport through Single Atoms.* Phys. Rev. Lett. **114**, 016602 (2015).

[68] S. Baumann, W. Paul, T. Choi, C. P. Lutz, A. Ardavan, and A. J. Heinrich. *Electron paramagnetic resonance of individual atoms on a surface.* Science **350**, 417 (2015).

[69] W. Paul, S. Baumann, C. P. Lutz, and A. J. Heinrich. *Generation of constant-amplitude radio-frequency sweeps at a tunnel junction for spin resonance STM.* Rev. Sci. Instrum. **87**, 074703 (2016).

[70] J. G. Simmons. *Generalized Formula for the Electric Tunnel Effect between Similar Electrodes Separated by a Thin Insulating Film.* J. Appl. Phys. **34**, 1793 (1963).

[71] J. G. Simmons. *Electric Tunnel Effect between Dissimilar Electrodes Separated by a Thin Insulating Film.* J. Appl. Phys. **34**, 2581 (1963).

[72] W. Nolting. *Grundkurs Theoretische Physik 5/2. Quantenmechanik - Methoden und Anwendungen.* (Springer-Verlag, Berlin, 2015).

[73] A. Selloni, P. Carnevali, E. Tosatti, and C. D. Chen. *Voltage-dependent scanning-tunneling microscopy of a crystal surface: Graphite.* Phys. Rev. B **31**, 2602 (1985).

[74] J. Tersoff and D. R. Hamann. *Theory and Application for the Scanning Tunneling Microscope.* Phys. Rev. Lett. **50**, 1998 (1983).

[75] J. Tersoff and D. R. Hamann. *Theory of the scanning tunneling microscope.* Phys. Rev. B **31**, 805 (1985).

[76] N. D. Lang. *Vacuum tunneling current from an adsorbed atom.* Phys. Rev. Lett. **55**, 230 (1985).

[77] N. D. Lang. *Theory of Single-Atom Imaging in the Scanning Tunneling Microscope.* Phys. Rev. Lett. **56**, 1164 (1986).

[78] N. D. Lang. *Spectroscopy of single atoms in the scanning tunneling microscope.* Phys. Rev. B **34**, 5947 (1986).

[79] B. N. J. Persson and A. Baratoff. *Inelastic electron tunneling from a metal tip: The contribution from resonant processes.* Phys. Rev. Lett. **59**, 339 (1987).

[80] C. J. Chen. *Theory of scanning tunneling spectroscopy.* J. Vac. Sci. Technol. **6**, 319 (1988).

[81] M. Ziegler, N. Néel, A. Sperl, J. Kröger, and R. Berndt. *Local density of states from constant-current tunneling spectra.* Phys. Rev. B **80** (2009).

[82] G. V. Nazin, S. W. Wu, and W. Ho. *Tunneling rates in electron transport through double-barrier molecular junctions in a scanning tunneling microscope.* Proc. Natl. Acad. Sci. U. S. A. **102**, 8832 (2005).

[83] S. Karan, D. Jacob, M. Karolak, C. Hamann, Y. Wang, A. Weismann, A. I. Lichtenstein, and R. Berndt. *Shifting the Voltage Drop in Electron Transport Through a Single Molecule.* Phys. Rev. Lett. **115**, 016802 (2015).

[84] L. Bartels, G. Meyer, and K.-H. Rieder. *Controlled vertical manipulation of single CO molecules with the scanning tunneling microscope: A route to chemical contrast.* Appl. Phys. Lett. **71**, 213 (1997).

[85] R. K. Tiwari, D. M. Otálvaro, C. Joachim, and M. Saeys. *Origin of the contrast inversion in the STM image of CO on Cu(111).* Surf. Sci. **603**, 3286 (2009).

[86] J. A. Stroscio, R. M. Feenstra, and A. P. Fein. *Electronic Structure of the Si(111)2×1 Surface by Scanning-Tunneling Microscopy.* Phys. Rev. Lett. **57**, 2579 (1986).

[87] B. Koslowski, C. Dietrich, A. Tschetschetkin, and P. Ziemann. *Evaluation of scanning tunneling spectroscopy data: Approaching a quantitative determination of the electronic density of states.* Phys. Rev. B **75**, 035421 (2007).

[88] J. Lambe and R. C. Jaklevic. *Molecular Vibration Spectra by Inelastic Electron Tunneling.* Phys. Rev. **165**, 821 (1968).

[89] S. Kahle. *Magnetic properties of Individual Molecules Studied by Scanning Tunneling Microscopy.* Ph.D. thesis, Universität Konstanz (2013).

[90] J. Klein, A. Léger, M. Belin, D. Défourneau, and M. J. L. Sangster. *Inelastic-Electron-Tunneling Spectroscopy of Metal-Insulator-Metal Junctions.* Phys. Rev. B **7**, 2336 (1973).

[91] A. Cornia and P. Seneor. *Spintronics: The Molecular Way.* Nat. Mater. **16**, 505 (2017).

[92] J. Kondo. *Resistance Minimum in Dilute Magnetic Alloys.* Progr. Theoret. Phys. **32**, 37 (1964).

[93] J. Kondo. *Effect of ordinary scattering on exchange scattering from magnetic impurity in metals.* Phys. Rev. **169**, 437 (1968).

[94] W. Meissner and B. Voigt. *Messungen mit Hilfe von flüssigem Helium XI Widerstand der reinen Metalle in tiefen Temperaturen.* Ann. Phys. **399**, 892 (1930).

[95] W. de Haas, J. de Boer, and G. van den Berg. *The electrical resistance of gold, copper and lead at low temperatures.* Physica **1**, 1115 (1934).

[96] M. Ternes, A. J. Heinrich, and W.-D. Schneider. *Spectroscopic manifestations of the Kondo effect on single adatoms.* J. Phys.: Condens. Matter **21**, 053001 (2009).

[97] V. Madhavan, W. Chen, T. Jamneala, M. F. Crommie, and N. S. Wingreen. *Tunneling into a Single Magnetic Atom: Spectroscopic Evidence of the Kondo Resonance.* Science **280**, 567 (1998).

[98] J. Li, W.-D. Schneider, R. Berndt, and B. Delley. *Kondo Scattering Observed at a Single Magnetic Impurity.* Phys. Rev. Lett. **80**, 2893 (1998).

[99] P. Wahl, L. Diekhöner, G. Wittich, L. Vitali, M. A. Schneider, and K. Kern. *Kondo Effect of Molecular Complexes at Surfaces: Ligand Control of the Local Spin Coupling.* Phys. Rev. Lett. **95**, 166601 (2005).

[100] Z. Huang, Y. Zhang, Y. He, H. Song, C. Yin, and K. Wu. *A chemist's overview of surface electron spins.* Chem. Soc. Rev. **46**, 1955 (2017).

[101] M. Ternes. *Probing magnetic excitations and correlations in single and coupled spin systems with scanning tunneling spectroscopy.* Prog. Surf. Sci. **92**, 83 (2017).

[102] I. Fernández-Torrente, K. J. Franke, and J. I. Pascual. *Vibrational Kondo Effect in Pure Organic Charge-Transfer Assemblies.* Phys. Rev. Lett. **101**, 217203 (2008).

[103] M. Garnica, D. Stradi, F. Calleja, S. Barja, C. Díaz, M. Alcamí, A. Arnau, A. L. Vázquez de Parga, F. Martín, and R. Miranda. *Probing the Site-Dependent Kondo Response of Nanostructured Graphene with Organic Molecules.* Nano Lett. **14**, 4560 (2014).

[104] S. Karan, N. Li, Y. Zhang, Y. He, I.-P. Hong, H. Song, J.-T. Lü, Y. Wang, L. Peng, K. Wu, G. S. Michelitsch, R. J. Maurer, K. Diller, K. Reuter, A. Weismann, and R. Berndt. *Spin Manipulation by Creation of Single-Molecule Radical Cations.* Phys. Rev. Lett. **116**, 027201 (2016).

[105] P. W. Anderson. *Localized magnetic states in metals.* Phys. Rev. **124**, 41 (1961).

[106] J. R. Schrieffer and P. A. Wolff. *Relation between the Anderson and Kondo Hamiltonians.* Phys. Rev. **149**, 491 (1966).

[107] M. Plihal and J. W. Gadzuk. *Nonequilibrium theory of scanning tunneling spectroscopy via adsorbate resonances: Nonmagnetic and Kondo impurities.* Phys. Rev. B **63**, 085404 (2001).

[108] U. Fano. *Effects of Configuration Interaction on Intensities and Phase Shifts.* Phys. Rev. **124**, 1866 (1961).

[109] N. Néel, J. Kröger, L. Limot, K. Palotas, W. A. Hofer, and R. Berndt. *Conductance and Kondo Effect in a Controlled Single-Atom Contact.* Phys. Rev. Lett. **98**, 016801 (2007).

[110] N. Néel, J. Kröger, R. Berndt, T. Wehling, A. Lichtenstein, and M. Katsnelson. *Controlling the Kondo Effect in $CoCu_n$ Clusters Atom by Atom.* Phys. Rev. Lett. **101**, 266803 (2008).

[111] N. Néel, J. Kröger, and R. Berndt. *Kondo effect of a Co atom on Cu(111) in contact with an iron tip.* Phys. Rev. B **82**, 233401 (2010).

[112] A. C. Hewson. *The Kondo Problem to Heavy Fermions* (Cambridge University Press, Cambridge, United Kingdom, 1993).

[113] N. Néel, R. Berndt, J. Kröger, T. O. Wehling, A. I. Lichtenstein, and M. I. Katsnelson. *Two-Site Kondo Effect in Atomic Chains.* Phys. Rev. Lett. **107**, 106804 (2011).

[114] E. Minamitani, N. Tsukahara, D. Matsunaka, Y. Kim, N. Takagi, and M. Kawai. *Symmetry-Driven Novel Kondo Effect in a Molecule.* Phys. Rev. Lett. **109**, 086602 (2012).

[115] J. Meyer, R. Ohmann, A. Nickel, C. Toher, R. Gresser, K. Leo, D. A. Ryndyk, F. Moresco, and G. Cuniberti. *Influence of organic ligands on the line shape of the Kondo resonance.* Phys. Rev. B **93**, 155118 (2016).

[116] Y. Li, A. T. Ngo, A. DiLullo, K. Z. Latt, H. Kersell, B. Fisher, P. Zapol, S. E. Ulloa, and S.-W. Hla. *Anomalous Kondo resonance mediated by semiconducting graphene nanoribbons in a molecular heterostructure.* Nat. Commun. **8** (2017).

[117] H. Prüser, M. Wenderoth, P. E. Dargel, A. Weismann, R. Peters, T. Pruschke, and R. G. Ulbrich. *Long-range Kondo signature of a single magnetic impurity.* Nat. Phys. **7**, 203 (2011).

[118] H. Prüser, M. Wenderoth, A. Weismann, and R. G. Ulbrich. *Mapping Itinerant Electrons around Kondo Impurities.* Phys. Rev. Lett. **108** (2012).

[119] D.-J. Choi, M. V. Rastei, P. Simon, and L. Limot. *Conductance-Driven Change of the Kondo Effect in a Single Cobalt Atom.* Phys. Rev. Lett. **108**, 266803 (2012).

[120] Q. Dubout, F. Donati, C. Wäckerlin, F. Calleja, M. Etzkorn, A. Lehnert, L. Claude, P. Gambardella, and H. Brune. *Controlling the Spin of Co Atoms on Pt(111) by Hydrogen Adsorption.* Phys. Rev. Lett. **114**, 106807 (2015).

[121] M. Ormaza, R. Robles, N. Bachellier, P. Abufager, N. Lorente, and L. Limot. *On-Surface Engineering of a Magnetic Organometallic Nanowire.* Nano Lett. **16**, 588 (2016).

[122] H. O. Frota. *Shape of the Kondo resonance.* Phys. Rev. B **45**, 1096 (1992).

[123] R. Žitko. *Kondo resonance lineshape of magnetic adatoms on decoupling layers.* Phys. Rev. B **84**, 195116 (2011).

[124] M. Pivetta, M. Ternes, F. Patthey, and W.-D. Schneider. *Diatomic Molecular Switches to Enable the Observation of Very-Low-Energy Vibrations.* Phys. Rev. Lett. **99**, 126104 (2007).

[125] W. A. Hofer, G. Teobaldi, and N. Lorente. *Creating pseudo-Kondo resonances by field-induced diffusion of atomic hydrogen.* Nanotechnology **19**, 305701 (2008).

[126] H. Chen, T. Pope, Z.-Y. Wu, D. Wang, L. Tao, D.-L. Bao, W. Xiao, J.-L. Zhang, Y.-Y. Zhang, S. Du, S. Gao, S. T. Pantelides, W. A. Hofer, and H.-J. Gao. *Evidence for Ultralow-Energy Vibrations in Large Organic Molecules.* Nano Lett. **17**, 4929 (2017).

[127] A. F. Otte, M. Ternes, K. von Bergmann, S. Loth, H. Brune, C. P. Lutz, C. F. Hirjibehedin, and A. J. Heinrich. *The role of magnetic anisotropy in the Kondo effect.* Nat. Phys. **4**, 847 (2008).

[128] A. J. Heinrich, J. A. Gupta, C. P. Lutz, and D. M. Eigler. *Single-atom spin-flip spectroscopy.* Science **306**, 466 (2004).

[129] A. F. Otte, M. Ternes, S. Loth, C. P. Lutz, C. F. Hirjibehedin, and A. J. Heinrich. *Spin Excitations of a Kondo-Screened Atom Coupled to a Second Magnetic Atom.* Phys. Rev. Lett. **103**, 107203 (2009).

[130] Y.-S. Fu, S.-H. Ji, X. Chen, X.-C. Ma, R. Wu, C.-C. Wang, W.-H. Duan, X.-H. Qiu, B. Sun, P. Zhang, J.-F. Jia, and Q.-K. Xue. *Manipulating the Kondo Resonance through Quantum Size Effects.* Phys. Rev. Lett. **99**, 256601 (2007).

[131] Y.-h. Zhang, S. Kahle, T. Herden, C. Stroh, M. Mayor, U. Schlickum, M. Ternes, P. Wahl, and K. Kern. *Temperature and magnetic field dependence of a Kondo system in the weak coupling regime.* Nat. Commun. **4**, 2110 (2013).

[132] K. Nagaoka, T. Jamneala, M. Grobis, and M. F. Crommie. *Temperature Dependence of a Single Kondo Impurity.* Phys. Rev. Lett. **88**, 077205 (2002).

[133] T. Jamneala, V. Madhavan, W. Chen, and M. F. Crommie. *Scanning tunneling spectroscopy of transition-metal impurities at the surface of gold.* Phys. Rev. B **61**, 9990 (2000).

[134] O. Újsághy, J. Kroha, L. Szunyogh, and A. Zawadowski. *Theory of the Fano resonance in the STM tunneling density of states due to a single Kondo impurity.* Phys. Rev. Lett. **85**, 2557 (2000).

[135] K. Oura, V. Lifshits, A. Saranin, A. Zotov, and M. Katayama. *Surface Science - An Introduction* (Springer, Berlin, 2003).

[136] H. Lüth. *Solid Surfaces, Interfaces and Thin Films* (Springer, Berlin, 2010).

[137] J. V. Barth. *Molecular Architectonic on Metal Surfaces.* Annu. Rev. Phys. Chem. **58**, 375 (2007).

[138] R. Otero, A. Vázquez de Parga, and J. Gallego. *Electronic, structural and chemical effects of charge-transfer at organic/inorganic interfaces.* Surf. Sci. Rep. **72**, 105 (2017).

[139] T. G. Gopakumar, M. Bernien, H. Naggert, F. Matino, C. F. Hermanns, A. Bannwarth, S. Mühlenberend, A. Krüger, D. Krüger, F. Nickel, W. Walter, R. Berndt, W. Kuch, and F. Tuczek. *Spin-Crossover Complex on Au(111): Structural and Electronic Differences Between Mono- and Multilayers.* Chem. - Eur. J. **19**, 15702 (2013).

[140] S. Ossinger, H. Naggert, L. Kipgen, T. Jasper-Tönnies, A. Rai, J. Rudnik, F. Nickel, L. M. Arruda, M. Bernien, W. Kuch, R. Berndt, and F. Tuczek. *Vacuum-Evaporable Spin-Crossover Complexes in Direct Contact with a Solid Surface: Bismuth versus Gold.* J. Phys. Chem. C **121**, 1210 (2017).

[141] W. Hieringer, K. Flechtner, A. Kretschmann, K. Seufert, W. Auwärter, J. V. Barth, A. Görling, H.-P. Steinrück, and J. M. Gottfried. *The Surface Trans Effect: Influence of Axial Ligands on the Surface Chemical Bonds of Adsorbed Metalloporphyrins.* J. Am. Chem. Soc. **133**, 6206 (2011).

[142] T. G. Gopakumar, H. Tang, J. Morillo, and R. Berndt. *Transfer of Cl Ligands between Adsorbed Iron Tetraphenylporphyrin Molecules.* J. Am. Chem. Soc. **134**, 11844 (2012).

[143] T. G. Gopakumar, T. Brumme, J. Kröger, C. Toher, G. Cuniberti, and R. Berndt. *Coverage-Driven Electronic Decoupling of Fe-Phthalocyanine from a Ag(111) Substrate.* J. Phys. Chem. C **115**, 12173 (2011).

[144] F. Bischoff, K. Seufert, W. Auwärter, S. Joshi, S. Vijayaraghavan, D. Écija, K. Diller, A. C. Papageorgiou, S. Fischer, F. Allegretti, D. A. Duncan, F. Klappenberger, F. Blobner, R. Han, and J. V. Barth. *How Surface Bonding and Repulsive Interactions Cause Phase Transformations: Ordering of a Prototype Macrocyclic Compound on Ag(111).* ACS Nano **7**, 3139 (2013).

[145] A. Kühnle. *Self-assembly of organic molecules at metal surfaces.* Curr. Opin. Colloid Interface Sci. **14**, 157 (2009).

[146] T. Yokoyama, T. Takahashi, K. Shinozaki, and M. Okamoto. *Quantitative Analysis of Long-Range Interactions between Adsorbed Dipolar Molecules on Cu(111).* Phys. Rev. Lett. **98**, 206102 (2007).

[147] I. Fernandez-Torrente, S. Monturet, K. Franke, J. Fraxedas, N. Lorente, and J. Pascual. *Long-Range Repulsive Interaction between Molecules on a Metal Surface Induced by Charge Transfer.* Phys. Rev. Lett. **99**, 176103 (2007).

[148] J. V. Barth, J. Weckesser, C. Cai, P. Günter, L. Bürgi, O. Jeandupeux, and K. Kern. *Building Supramolecular Nanostructures at Surfaces by Hydrogen Bonding.* Angew. Chem. Int. Ed. **39**, 1230 (2000).

[149] J. Repp, F. Moresco, G. Meyer, K.-H. Rieder, P. Hyldgaard, and M. Persson. *Substrate mediated long-range oscillatory interaction between adatoms: Cu/Cu(111).* Phys. Rev. Lett. **85**, 2981 (2000).

[150] S. Lukas, G. Witte, and C. Wöll. *Novel Mechanism for Molecular Self-Assembly on Metal Substrates: Unidirectional Rows of Pentacene on Cu(110) Produced by a Substrate-Mediated Repulsion.* Phys. Rev. Lett. **88**, 028301 (2001).

[151] P. Gütlich and H. A. Goodwin. *Spin Crossover – An Overall Perspective.* Top. Curr. Chem. **233**, 1 (2004).

[152] W. Kuch and M. Bernien. *Controlling the magnetism of adsorbed metal-organic molecules.* J. Phys.: Condens. Matter **29**, 023001 (2017).

[153] P. Gütlich, A. B. Gaspar, and Y. Garcia. *Spin state switching in iron coordination compounds.* Beilstein J. Org. Chem. **9**, 342 (2013).

[154] S. Shi, G. Schmerber, J. Arabski, J.-B. Beaufrand, D. J. Kim, S. Boukari, M. Bowen, N. T. Kemp, N. Viart, G. Rogez, E. Beaurepaire, H. Aubriet, J. Petersen, C. Becker, and D. Ruch. *Study of molecular spin-crossover complex $Fe(phen)_2(NCS)_2$ thin films.* Appl. Phys. Lett. **95**, 043303 (2009).

[155] M. Bernien, H. Naggert, L. M. Arruda, L. Kipgen, F. Nickel, J. Miguel, C. F. Hermanns, A. Krüger, D. Krüger, E. Schierle, E. Weschke, F. Tuczek, and W. Kuch. *Highly Efficient Thermal and Light-Induced Spin-State Switching of an Fe(II) Complex in Direct Contact with a Solid Surface.* ACS Nano **9**, 8960 (2015).

[156] X. Zhang, T. Palamarciuc, J.-F. Létard, P. Rosa, E. V. Lozada, F. Torres, L. G. Rosa, B. Doudin, and P. A. Dowben. *The spin state of a molecular adsorbate driven by the ferroelectric substrate polarization.* Chem. Commun. **50**, 2255 (2014).

[157] Y. Qi, E. Müller, H. Spiering, and P. Gütlich. *The effect of a magnetic field on the high-spin low-spin transition in [Fe(phen)$_2$(NCS)$_2$].* Chem. Phys. Lett. **101**, 503 (1983).

[158] K. Senthil Kumar and M. Ruben. *Emerging trends in spin crossover (SCO) based functional materials and devices.* Coord. Chem. Rev. **346**, 176 (2017).

[159] W. Koch and M. C. Holthausen. *A chemist's Guide to Density Functional Theory* (Wiley-VCH, Weinstein, Germany, 2nd edition, 2001).

[160] F. Jensen. *Introduction to Computational Chemistry* (Wiley & Sons Ltd, West Sussex, England, 2nd edition, 2007).

[161] P. Hohenberg and W. Kohn. *Inhomogeneous Electron Gas.* Phys. Rev. **136**, B864 (1964).

[162] W. Kohn and L. Sham. *Self-Consistent Equations Including Exchange and Correlation Effects.* Phys. Rev. A **140**, A1133 (1965).

[163] C. J. Cramer and D. G. Truhlar. *Density functional theory for transition metals and transition metal chemistry.* Phys. Chem. Chem. Phys. **11**, 10757 (2009).

[164] S.-C. Qi, J.-i. Hayashi, and L. Zhang. *Recent application of calculations of metal complexes based on density functional theory.* RSC Adv. **6**, 77375 (2016).

[165] J. P. Perdew and K. Schmidt. *Jacob's ladder of density functional approximations for the exchange-correlation energy.* AIP Conf. Proc. **577**, 1 (2001).

[166] J. P. Perdew, K. Burke, and M. Ernzerhof. *Generalized gradient approximation made simple.* Phys. Rev. Lett. **77**, 3865 (1996).

[167] A. D. Becke. *Density-Functional Exchange-Energy Approximation with Correct Asymptotic Behavior.* Phys. Rev. A **38**, 3098 (1988).

[168] J. P. Perdew. *Density-Functional Approximation for the Correlation Energy of the Inhomogeneous Electron Gas.* Phys. Rev. B **33**, 8822 (1986).

[169] A. D. Becke. *Density-functional thermochemistry. III. The role of exact exchange.* J. Chem. Phys. **98**, 5648 (1993).

[170] C. Lee, W. Yang, and R. G. Parr. *Development of the Colle-Salvetti correlation-energy formula into a functional of the electron density.* Phys. Rev. B **37**, 785 (1988).

[171] J. Tao, J. P. Perdew, V. N. Staroverov, and G. E. Scuseria. *Climbing the Density Functional Ladder: Nonempirical Meta-Generalized Gradient Approximation Designed for Molecules and Solids.* Phys. Rev. Lett. **91**, 146401 (2003).

[172] V. N. Staroverov, G. E. Scuseria, J. Tao, and J. P. Perdew. *Comparative assessment of a new nonempirical density functional: Molecules and hydrogen-bonded complexes.* J. Chem. Phys. **119**, 12129 (2003).

[173] N. Pagels, O. Albrecht, D. Görlitz, A. Y. Rogachev, M. H. Prosenc, and J. Heck. *Electronic Coupling through Intramolecular π-π Interactions in Biscobaltocenes: A Structural, Spectroscopic, and Magnetic Study.* Chem. Eur. J. **17**, 4166 (2011).

[174] *University Computing Centre, Kiel.* `https://www.rz.uni-kiel.de`.

[175] M. J. Frisch, G. W. Trucks, H. B. Schlegel, G. E. Scuseria, M. A. Robb, J. R. Cheeseman, G. Scalmani, V. Barone, B. Mennucci, and G. A. Petersson. *Gaussian 09 Revision D.01* (2013). Gaussian Inc. Wallingford CT.

[176] A. Schäfer, C. Huber, and R. Ahlrichs. *Fully Optimized Contracted Gaussian Basis Sets of Triple Zeta Valence Quality for Atoms Li to Kr.* J. Phys. Chem. **100**, 5829 (1994).

[177] F. Weigend and R. Ahlrichs. *Balanced basis sets of split valence, triple zeta valence and quadruple zeta valence quality for H to Rn: Design and assessment of accuracy.* Phys. Chem. Chem. Phys. **7**, 3297 (2005).

[178] *CreaTec Fischer & Co. GmbH.* `www.createc.de`.

[179] H. Jensen. *Zusammenbau eines Rastertunnelmikroskops und erste Messungen an einkristallinen Metalloberflächen.* Diploma thesis, Christian-Albrechts-Universität zu Kiel (2003).

[180] C. Hamann. *An electrospray ion source for ultra-high vacuum deposition of organic molecules.* Ph.D. thesis, Christian-Albrechts-Universität zu Kiel (2011).

[181] N. Hauptmann. *Force and Conductance in Molecular Junctions.* Ph.D. thesis, Christian-Albrechts-Universität zu Kiel (2013).

[182] K. Besocke. *An easily operable scanning tunneling microscope.* Surf. Sci. **181**, 145 (1987).

[183] J. Frohn, J. F. Wolf, K. Besocke, and M. Teske. *Coarse tip distance adjustment and positioner for a scanning tunneling microscope.* Rev. Sci. Instrum. **60**, 1200 (1989).

[184] *SPECS Zurich GmbH.* `http://www.specs-zurich.com`.

[185] *FEMTO Messtechnik GmbH.* `http://www.femto.de`.

[186] *Stanford Research Systems, Inc.* `http://www.thinksrs.com/`.

[187] I. Horcas, R. Fernández, J. M. Gómez-Rodríguez, J. Colchero, J. Gómez-Herrero, and A. M. Baro. *A software for scanning probe microscopy and a tool for nanotechnology.* Rev. Sci. Instrum. **78**, 013705 (2007).

[188] J. Donner, J.-P. Broschinski, B. Feldscher, A. Stammler, H. Bögge, T. Glaser, and D. Wegner. *Correlating Electronic and Magnetic Coupling in Large Magnetic Molecules via Scanning Tunneling Microscopy.* Phys. Rev. B **95**, 165441 (2017).

[189] M. Bazarnik, B. Bugenhagen, M. Elsebach, E. Sierda, A. Frank, M. H. Prosenc, and R. Wiesendanger. *Toward Tailored All-Spin Molecular Devices.* Nano Lett. **16**, 577 (2016).

[190] E. A. Ziemann, N. Freudenreich, N. Speil, T. Stein, N. Van Steerteghem, K. Clays, and J. Heck. *Synthesis, Structure and NLO Properties of a 1,3,5-Substituted Tricationic Cobaltocenium Benzene Complex.* J. Organomet. Chem. **820**, 125 (2016).

[191] A. Vecchi, P. Galloni, B. Floris, S. V. Dudkin, and V. N. Nemykin. *Metallocenes meet porphyrinoids: Consequences of a fusion.* Coord. Chem. Rev. **291**, 95 (2015).

[192] S. Venkataramani, U. Jana, M. Dommaschk, F. D. Sönnichsen, F. Tuczek, and R. Herges. *Magnetic Bistability of Molecules in Homogeneous Solution at Room Temperature.* Science **331**, 445 (2011).

[193] M. Dommaschk, M. Peters, F. Gutzeit, C. Schütt, C. Näther, F. D. Sönnichsen, S. Tiwari, C. Riedel, S. Boretius, and R. Herges. *Photoswitchable Magnetic Resonance Imaging Contrast by Improved Light-Driven Coordination-Induced Spin State Switch.* J. Am. Chem. Soc. **137**, 7552 (2015).

[194] B. Baisch, D. Raffa, U. Jung, O. M. Magnussen, C. Nicolas, J. Lacour, J. Kubitschke, and R. Herges. *Mounting Freestanding Molecular Functions onto Surfaces: The Platform Approach.* J. Am. Chem. Soc. **131**, 442 (2009).

[195] U. Jung, C. Schütt, O. Filinova, J. Kubitschke, R. Herges, and O. Magnussen. *Photoswitching of Azobenzene-Functionalized Molecular Platforms on Au Surfaces.* J. Phys. Chem. C **116**, 25943 (2012).

[196] F. L. Otte, S. Lemke, C. Schütt, N. R. Krekiehn, U. Jung, O. M. Magnussen, and R. Herges. *Ordered Monolayers of Free-Standing Porphyrins on Gold.* J. Am. Chem. Soc. **136**, 11248 (2014).

[197] M. Hammerich and R. Herges. *Laterally Mounted Azobenzenes on Platforms.* J. Org. Chem. **80**, 11233 (2015).

[198] C. M. Whitehouse, R. N. Dreyer, M. Yamashita, and J. B. Fenn. *Electrospray ionization for mass-spectrometry of large biomolecules.* Science **246**, 64 (1989).

[199] J. B. Fenn. *Electrospray Wings for Molecular Elephants (Nobel Lecture).* Angew. Chem. Int. Ed. **42**, 3871 (2003).

[200] J. A. Zasadzinski, R. Viswanathan, L. Madsen, J. Garnaes, D. K. Schwartz, and others. *Langmuir-blodgett films.* Science **263**, 1726 (1994).

[201] *Press release: The Nobel prize in Chemistry 2002.* `http://www.nobelprize.org/nobel_prizes/chemistry/laureates/2002/press.html`. 9. October 2002.

[202] J. H. Gross. *Mass Spectrometry. A Textbook.* (Springer-Verlag Berlin Heidelberg, 2004).

[203] V. N. Morozov and T. Y. Morozova. *Electrospray Deposition as a Method for Mass Fabrication of Mono- and Multicomponent Microarrays of Biological and Biologically Active Substances.* Anal. Chem. **71**, 3110 (1999).

[204] Z. Ouyang, Z. Takáts, T. A. Blake, B. Gologan, A. J. Guymon, J. M. Wiseman, J. C. Oliver, V. J. Davisson, and R. G. Cooks. *Preparing protein microarrays by soft-landing of mass-selected ions.* Science **301**, 1351 (2003).

[205] J. Donner, J.-P. Broschinski, T. Glaser, and D. Wegner. *Deposition and Self-Assembly of Large Magnetic Molecules.* J. Phys. Chem. C **119**, 28660 (2015).

[206] L. Vitali, S. Fabris, A. M. Conte, S. Brink, M. Ruben, S. Baroni, and K. Kern. *Electronic Structure of Surface-supported Bis(phthalocyaninato) terbium(III) Single Molecular Magnets.* Nano Lett. **8**, 3364 (2008).

[207] S. Rauschenbach, F. L. Stadler, E. Lunedei, N. Malinowski, S. Koltsov, G. Costantini, and K. Kern. *Electrospray Ion Beam Deposition of Clusters and Biomolecules.* Small **2**, 540 (2006).

[208] N. B. Cech and C. G. Enke. *Practical implications of some recent studies in electrospray ionization fundamentals.* Mass Spectrom. Rev. **20**, 362 (2001).

[209] G. Taylor. *Disintegration of water drops in an electric field.* Proc. R. Soc. A **280**, 383 (1964).

[210] D. Duft, T. Achtzehn, R. Müller, B. A. Huber, and T. Leisner. *Coulomb fission: Rayleigh jets from levitated microdroplets.* Nature **421**, 128 (2003).

[211] D. C. Taflin, T. L. Ward, and E. J. Davis. *Electrified droplet fission and the Rayleigh limit.* Langmuir **5**, 376 (1989).

[212] L. Konermann, E. Ahadi, A. D. Rodriguez, and S. Vahidi. *Unraveling the Mechanism of Electrospray Ionization.* Anal. Chem. **85**, 2 (2013).

[213] V. Katta, S. K. Chowdhury, and B. T. Chait. *Electrospray Ionization: A New Tool for the Analysis of Ionic Transition-Metal Complexes.* J. Am. Chem. Soc. **112**, 5348 (1990).

[214] C. Hamann, R. Woltmann, I.-P. Hong, N. Hauptmann, S. Karan, and R. Berndt. *Ultrahigh Vacuum Deposition of Organic Molecules by Electrospray Ionization.* Rev. Sci. Instrum. **82**, 033903 (2011).

[215] K. Buchmann. *Scanning Tunneling Microscopy of Functionalised Molecular Platforms deposited using a new Ion Funnel.* Diploma thesis, Christian-Albrechts-Universität zu Kiel (2012).

[216] N. Hauptmann, C. Hamann, H. Tang, and R. Berndt. *Soft-Landing Electrospray Deposition of the Ruthenium Dye N3 on Au(111).* J. Phys. Chem. C **117**, 9734 (2013).

[217] S. Karan, T. G. Gopakumar, H. Jacob, S. Meyer, F. Tuczek, and R. Berndt. *Remotely Triggered Geometrical Isomerization of a Binuclear Complex.* J. Am. Chem. Soc. **136**, 6163 (2014).

[218] T. Jasper-Tönnies, M. Gruber, S. Karan, H. Jacob, F. Tuczek, and R. Berndt. *Deposition of a Cationic Fe(III) Spin-Crossover Complex on Au(111): Impact of the Counter Ion.* J. Phys. Chem. Lett. **8**, 1569 (2017).

[219] N. Hauptmann, K. Scheil, T. G. Gopakumar, F. L. Otte, C. Schütt, R. Herges, and R. Berndt. *Surface Control of Alkyl Chain Conformations and 2D Chiral Amplification.* J. Am. Chem. Soc. **135**, 8814 (2013).

[220] N. Hauptmann, L. Groß, K. Buchmann, K. Scheil, C. Schütt, F. L. Otte, R. Herges, C. Herrmann, and R. Berndt. *High-conductance surface-anchoring of a mechanically flexible platform-based porphyrin complex.* New J. Phys. **17**, 013012 (2015).

[221] L. Bogani and W. Wernsdorfer. *Molecular spintronics using single-molecule magnets.* Nat. Mater. **7**, 179 (2008).

[222] V. A. Dediu, L. E. Hueso, I. Bergenti, and C. Taliani. *Spin Routes in Organic Semiconductors.* Nat. Mater. **8**, 707 (2009).

[223] C. Barraud, P. Seneor, R. Mattana, S. Fusil, K. Bouzehouane, C. Deranlot, P. Graziosi, L. Hueso, I. Bergenti, V. Dediu, F. Petroff, and A. Fert. *Unravelling the Role of the Interface for Spin Injection into Organic Semiconductors.* Nat. Phys. **6**, 615 (2010).

[224] K. V. Raman, A. M. Kamerbeek, A. Mukherjee, N. Atodiresei, T. K. Sen, P. Lazić, V. Caciuc, R. Michel, D. Stalke, S. K. Mandal, S. Blügel, M. Münzenberg, and J. S. Moodera. *Interface-Engineered Templates for Molecular Spin Memory Devices.* Nature **493**, 509 (2013).

[225] S. Steil, N. Großmann, M. Laux, A. Ruffing, D. Steil, M. Wiesenmayer, S. Mathias, O. L. A. Monti, M. Cinchetti, and M. Aeschlimann. *Spin-Dependent Trapping of Electrons at Spinterfaces*. Nat. Phys. **9**, 242 (2013).

[226] M. Gruber, F. Ibrahim, S. Boukari, H. Isshiki, L. Joly, M. Peter, M. Studniarek, V. Da Costa, H. Jabbar, V. Davesne, U. Halisdemir, J. Chen, J. Arabski, E. Otero, F. Choueikani, K. Chen, P. Ohresser, W. Wulfhekel, F. Scheurer, W. Weber, M. Alouani, E. Beaurepaire, and M. Bowen. *Exchange Bias and Room-Temperature Magnetic Order in Molecular Layers*. Nat. Mater. **14**, 981 (2015).

[227] K. Bairagi, A. Bellec, V. Repain, C. Chacon, Y. Girard, Y. Garreau, J. Lagoute, S. Rousset, R. Breitwieser, Y.-C. Hu, Y. C. Chao, W. W. Pai, D. Li, A. Smogunov, and C. Barreteau. *Tuning the Magnetic Anisotropy at a Molecule-Metal Interface*. Phys. Rev. Lett. **114**, 247203 (2015).

[228] M. Gruber, F. Ibrahim, S. Boukari, L. Joly, V. Da Costa, M. Studniarek, M. Peter, H. Isshiki, H. Jabbar, V. Davesne, J. Arabski, E. Otero, F. Choueikani, K. Chen, P. Ohresser, W. Wulfhekel, F. Scheurer, E. Beaurepaire, M. Alouani, W. Weber, and M. Bowen. *Spin-Dependent Hybridization between Molecule and Metal at Room Temperature through Interlayer Exchange Coupling*. Nano Lett. **15**, 7921 (2015).

[229] F. A. Ma'Mari, T. Moorsom, G. Teobaldi, W. Deacon, T. Prokscha, H. Luetkens, S. Lee, G. E. Sterbinsky, D. A. Arena, D. A. MacLaren, M. Flokstra, M. Ali, M. C. Wheeler, G. Burnell, B. J. Hickey, and O. Cespedes. *Beating the Stoner criterion using molecular interfaces*. Nature **524**, 69 (2015).

[230] F. Djeghloul, M. Gruber, E. Urbain, D. Xenioti, L. Joly, S. Boukari, J. Arabski, H. Bulou, F. Scheurer, F. Bertran, P. Le Fèvre, A. Taleb-Ibrahimi, W. Wulfhekel, G. Garreau, S. Hajjar-Garreau, P. Wetzel, M. Alouani, E. Beaurepaire, M. Bowen, and W. Weber. *High Spin Polarization at Ferromagnetic Metal–organic Interfaces: A Generic Property*. J. Phys. Chem. Lett. **7**, 2310 (2016).

[231] T. Choi, S. Bedwani, A. Rochefort, C.-Y. Chen, A. J. Epstein, and J. A. Gupta. *A Single Molecule Kondo Switch: Multistability of Tetracyanoethylene on Cu(111)*. Nano Lett. **10**, 4175 (2010).

[232] T. Komeda, H. Isshiki, J. Liu, Y.-F. Zhang, N. Lorente, K. Katoh, B. K. Breedlove, and M. Yamashita. *Observation and electric current control of a local spin in a single-molecule magnet*. Nat. Commun. **2**, 217 (2011).

[233] R. Robles, N. Lorente, H. Isshiki, J. Liu, K. Katoh, B. K. Breedlove, M. Yamashita, and T. Komeda. *Spin Doping of Individual Molecules by Using Single-Atom Manipulation*. Nano Lett. **12**, 3609 (2012).

[234] H. Kim, Y. H. Chang, S.-H. Lee, Y.-H. Kim, and S.-J. Kahng. *Switching and Sensing Spin States of Co–porphyrin in Bimolecular Reactions on Au(111) Using Scanning Tunneling Microscopy.* ACS Nano **7**, 9312 (2013).

[235] V. Iancu, A. Deshpande, and S.-W. Hla. *Manipulation of the Kondo Effect via Two-Dimensional Molecular Assembly.* Phys. Rev. Lett. **97**, 266603 (2006).

[236] M. Gruber, V. Davesne, M. Bowen, S. Boukari, E. Beaurepaire, W. Wulfhekel, and T. Miyamachi. *Spin state of spin-crossover complexes: From single molecules to ultrathin films.* Phys. Rev. B **89**, 195415 (2014).

[237] T. Esat, T. Deilmann, B. Lechtenberg, C. Wagner, P. Krüger, R. Temirov, F. B. Anders, M. Rohlfing, and F. S. Tautz. *Transfering spin into an extended π orbital of a large molecule.* Phys. Rev. B **91**, 144415 (2015).

[238] T. Esat, B. Lechtenberg, T. Deilmann, C. Wagner, P. Krüger, R. Temirov, M. Rohlfing, F. B. Anders, and F. S. Tautz. *A chemically driven quantum phase transition in a two-molecule Kondo system.* Nat. Phys. **12**, 867 (2016).

[239] S. Karan and R. Berndt. *Generation of spin in single cholesterol molecules on gold.* Phys. Chem. Chem. Phys. **18**, 9334 (2016).

[240] K. Bairagi, O. Iasco, A. Bellec, A. Kartsev, D. Li, J. Lagoute, C. Chacon, Y. Girard, S. Rousset, F. Miserque, Y. J. Dappe, A. Smogunov, C. Barreteau, M.-L. Boillot, T. Mallah, and V. Repain. *Molecular-scale dynamics of light-induced spin cross-over in a two-dimensional layer.* Nat. Commun. **7**, 12212 (2016).

[241] M. Gruber, T. Miyamachi, V. Davesne, M. Bowen, S. Boukari, W. Wulfhekel, M. Alouani, and E. Beaurepaire. *Spin Crossover in $Fe(phen)_2(NCS)_2$ Complexes on Metallic Surfaces.* J. Chem. Phys. **146**, 092312 (2017).

[242] U. G. E. Perera, H. J. Kulik, V. Iancu, L. G. G. V. Dias da Silva, S. E. Ulloa, N. Marzari, and S.-W. Hla. *Spatially Extended Kondo State in Magnetic Molecules Induced by Interfacial Charge Transfer.* Phys. Rev. Lett. **105**, 106601 (2010).

[243] A. Mugarza, C. Krull, R. Robles, S. Stepanow, G. Ceballos, and P. Gambardella. *Spin coupling and relaxation inside molecule-metal contacts.* Nat. Commun. **2**, 490 (2011).

[244] A. DiLullo, S.-H. Chang, N. Baadji, K. Clark, J.-P. Klöckner, M.-H. Prosenc, S. Sanvito, R. Wiesendanger, G. Hoffmann, and S.-W. Hla. *Molecular Kondo Chain.* Nano Lett. **12**, 3174 (2012).

[245] A. Stróżecka, M. Soriano, J. I. Pascual, and J. J. Palacios. *Reversible Change of the Spin State in a Manganese Phthalocyanine by Coordination of CO Molecule.* Phys. Rev. Lett. **109**, 147202 (2012).

[246] J. Liu, H. Isshiki, K. Katoh, T. Morita, K. Breedlove, Brian, M. Yamashita, and T. Komeda. *First Observation of a Kondo Resonance for a Stable Neutral Pure Organic Radical, 1,3,5-Triphenyl-6-oxoverdazyl, Adsorbed on the Au(111) Surface.* J. Am. Chem. Soc. **135**, 651 (2013).

[247] W. Wang, R. Pang, G. Kuang, X. Shi, X. Shang, P. N. Liu, and N. Lin. *Intramolecularly resolved Kondo resonance of high-spin Fe(II)-porphyrin adsorbed on Au(111).* Phys. Rev. B **91**, 045440 (2015).

[248] E. Minamitani, Y.-S. Fu, Q.-K. Xue, Y. Kim, and S. Watanabe. *Spatially extended underscreened Kondo state from collective molecular spin.* Phys. Rev. B **92**, 075144 (2015).

[249] L. Zhang, A. Bagrets, D. Xenioti, R. Korytár, M. Schackert, T. Miyamachi, F. Schramm, O. Fuhr, R. Chandrasekar, M. Alouani, M. Ruben, W. Wulfhekel, and F. Evers. *Kondo effect in binuclear metal-organic complexes with weakly interacting spins.* Phys. Rev. B **91**, 195424 (2015).

[250] B. Warner, F. El Hallak, N. Atodiresei, P. Seibt, H. Prüser, V. Caciuc, M. Waters, A. J. Fisher, S. Blügel, J. van Slageren, and C. F. Hirjibehedin. *Sub-molecular modulation of a 4f driven Kondo resonance by surface-induced asymmetry.* Nat. Commun. **7**, 12785 (2016).

[251] K. J. Franke, G. Schulze, and J. I. Pascual. *Competition of Superconducting Phenomena and Kondo Screening at the Nanoscale.* Science **332**, 940 (2011).

[252] G. E. Pacchioni, M. Pivetta, L. Gragnaniello, F. Donati, G. Autès, O. V. Yazyev, S. Rusponi, and H. Brune. *Two-Orbital Kondo Screening in a Self-Assembled Metal–organic Complex.* ACS Nano **11**, 2675 (2017).

[253] C. Lindström. *Synthese und Charakterisierung mehrkerniger benzolverbrückter Cobalt-Sandwich-Komplexe.* Ph.D. thesis, Universität Hamburg (2016).

[254] U. Hagenau, J. Heck, E. Hendrickx, A. Persoons, T. Schuld, and H. Wong. *A new Heterobimetallic Basic NLO Chromophore.* Inorg. Chem. **35**, 7863 (1996).

[255] C. F. Hermanns, K. Tarafder, M. Bernien, A. Krüger, Y.-M. Chang, P. M. Oppeneer, and W. Kuch. *Magnetic Coupling of Porphyrin Molecules Through Graphene.* Adv. Mater. **25**, 3473 (2013).

[256] P. E. Blöchl. *Projector Augmented-Wave Method.* Phys. Rev. B **50**, 17953 (1994).

[257] G. Kresse and J. Furthmüller. *Efficient Iterative Schemes for Ab Initio Total-Energy Calculations Using a Plane-Wave Basis Set.* Phys. Rev. B **54**, 11169 (1996).

[258] H. Lesnard, M.-L. Bocquet, and N. Lorente. *Dehydrogenation of Aromatic Molecules under a Scanning Tunneling Microscope: Pathways and Inelastic Spectroscopy Simulations*. J. Am. Chem. Soc. **129**, 4298 (2007).

[259] E. O. Fischer and R. Jira. *Di-cyclopentadienyl-kobalt(II)*. Z. Naturforsch. **8 b**, 327 (1953).

[260] M. Ormaza, P. Abufager, N. Bachellier, R. Robles, M. Verot, T. Le Bahers, M.-L. Bocquet, N. Lorente, and L. Limot. *Assembly of Ferrocene Molecules on Metal Surfaces Revisited*. J. Phys. Chem. Lett. **6**, 395 (2015).

[261] N. Bachellier, M. Ormaza, M. Faraggi, B. Verlhac, M. Vérot, T. Le Bahers, M.-L. Bocquet, and L. Limot. *Unveiling Nickelocene Bonding to a Noble Metal Surface*. Phys. Rev. B **93**, 195403 (2016).

[262] M. Ormaza, N. Bachellier, M. N. Faraggi, B. Verlhac, P. Abufager, P. Ohresser, L. Joly, M. Romeo, F. Scheurer, M.-L. Bocquet, N. Lorente, and L. Limot. *Efficient Spin-Flip Excitation of a Nickelocene Molecule*. Nano Lett. **17**, 1877 (2017).

[263] T. Hascall, V. Beck, S. Barlow, and A. R. Cowley. *Synthesis and Characterization of a Bimetallic Boratabenzene Cobalt Complex*. Organometallics **23**, 3808 (2004).

[264] V. Zlatić, B. Horvatić, and D. Šokčević. *Density of states for intermediate valence and Kondo systems*. Z. Phys. B **59**, 151 (1985).

[265] L. Giovanelli, A. Savoyant, M. Abel, F. Maccherozzi, Y. Ksari, M. Koudia, R. Hayn, F. Choueikani, E. Otero, P. Ohresser, J.-M. Themlin, S. S. Dhesi, and S. Clair. *Magnetic Coupling and Single-Ion Anisotropy in Surface-Supported Mn-Based Metal–organic Networks*. J. Phys. Chem. C **118**, 11738 (2014).

[266] S. Gueddida, M. Gruber, T. Miyamachi, E. Beaurepaire, W. Wulfhekel, and M. Alouani. *Exchange Coupling of Spin-Crossover Molecules to Ferromagnetic Co Islands*. J. Phys. Chem. Lett. **7**, 900 (2016).

[267] C. Barraud, K. Bouzehouane, C. Deranlot, D. J. Kim, R. Rakshit, S. Shi, J. Arabski, M. Bowen, E. Beaurepaire, S. Boukari, F. Petroff, P. Seneor, and R. Mattana. *Phthalocyanine Based Molecular Spintronic Devices*. Dalton Trans. **45**, 16694 (2016).

[268] M. Cinchetti, V. A. Dediu, and L. E. Hueso. *Activating the Molecular Spinterface*. Nat. Mater. **16**, 507 (2017).

[269] A. Mugarza, R. Robles, C. Krull, R. Korytár, N. Lorente, and P. Gambardella. *Electronic and Magnetic Properties of Molecule-Metal Interfaces: Transition-Metal Phthalocyanines Adsorbed on Ag(100)*. Phys. Rev. B **85**, 155437 (2012).

[270] C. Krull, R. Robles, A. Mugarza, and P. Gambardella. *Site- and Orbital-Dependent Charge Donation and Spin Manipulation in Electron-Doped Metal Phthalocyanines*. Nat. Mater. **12**, 337 (2013).

[271] G. E. Pacchioni, M. Pivetta, L. Gragnaniello, F. Donati, G. Autès, O. V. Yazyev, S. Rusponi, and H. Brune. *Two-Orbital Kondo Screening in a Self-Assembled Metal–organic Complex*. ACS Nano **11**, 2675 (2017).

[272] T. Knaak, M. Gruber, C. Lindström, J. Heck, and R. Berndt. *Ligand-Induced Energy Shift and Localization of Kondo Resonances in Cobalt-Based Complexes on Cu(111)*. Nano Lett. **17**, 7146 (2017).

[273] Y. S. Fu, Q. K. Xue, and R. Wiesendanger. *Spin-Resolved Splitting of Kondo Resonances in the Presence of RKKY-Type Coupling*. Phys. Rev. Lett. **108**, 87203 (2012).

[274] O. Shoji, H. Tanaka, T. Kawai, and Y. Kobuke. *Single Molecule Visualization of Coordination-Assembled Porphyrin Macrocycles Reinforced with Covalent Linkings*. J. Am. Chem. Soc. **127**, 8598 (2005).

[275] R. Hellwig, T. Paintner, Z. Chen, M. Ruben, A. P. Seitsonen, F. Klappenberger, H. Brune, and J. V. Barth. *Epitaxy-Induced Assembly and Enantiomeric Switching of an On-Surface Formed Dinuclear Organocobalt Complex*. ACS Nano **11**, 1347 (2017).

[276] T. J. Kealy and P. L. Pauson. *A New Type of Organo-Iron Compound*. Nature **168**, 1039 (1951).

[277] A. Togni and R. L. Halterman. *Metallocenes: Synthesis Reactivity Applications* (Wiley-VCH, 1998).

[278] M. T. Lee, B. M. Foxman, and M. Rosenblum. *Cofacial Metallocenes. Synthesis and Crystal Structure of 1,8-Diferrocenylnaphthalene*. Organometallics **4**, 539 (1985).

[279] S. Barlow and D. O'Hare. *Metal-Metal Interactions in Linked Metallocenes*. Chem. Rev. **97**, 637 (1997).

[280] M. Wagner. *A New Dimension in Multinuclear Metallocene Complexes*. Angew. Chem., Int. Ed. **45**, 5916 (2006).

[281] L. E. Wilson, C. Hassenrück, R. F. Winter, A. J. P. White, T. Albrecht, and N. J. Long. *Ferrocene- and Biferrocene-Containing Macrocycles towards Single-Molecule Electronics*. Angew. Chem., Int. Ed. **56**, 6838 (2017).

[282] P. Nguyen, P. Gómez-Elipe, and I. Manners. *Organometallic Polymers with Transition Metals in the Main Chain*. Chem. Rev. **99**, 1515 (1999).

[283] A. Escribano, T. Steenbock, C. Stork, C. Herrmann, and J. Heck. *Why Are Dithienylethene-Linked Biscobaltocenes so Hard to Photoswitch?* ChemPhysChem **18**, 596 (2017).

[284] C. Elschenbroich, M. Wolf, O. Schiemann, K. Harms, O. Burghaus, and J. Pebler. *Head-on versus Side-on [5–5] Bitrovacenes Featuring Benzene and Naphthalene Units as Spacers: How π-Stacking Affects Exchange Coupling and Redox Splitting.* Organometallics **21**, 5810 (2002).

[285] F. Benner. *C_3-Symmetric Paramagnetic Metallocenes as Molecular Magnetic Materials.* Master's thesis, Universität Hamburg (2017).

[286] N. Pagels and J. Heck. *Synthesis and Structural Characterization of 1,8-Biscobaltocen-1'-Ylium-Naphthalene Dication: Towards Paramagnetic, Cofacially Stacked Metallocenes.* J. Organomet. Chem. **693**, 241 (2008).

[287] A. Bahde. *Spin-Polarized Molecules on Metal Surfaces: Do They Keep Their Spin?* B.S. Thesis, Universität Hamburg (2015).

[288] M. Böhringer, K. Morgenstern, W.-D. Schneider, R. Berndt, F. Mauri, A. De Vita, and R. Car. *Two-Dimensional Self-Assembly of Supramolecular Clusters and Chains.* Phys. Rev. Lett. **83**, 324 (1999).

[289] S. Karan, C. Hamann, H. Tang, A. R. Stefankiewicz, J.-M. Lehn, and R. Berndt. *Surface Trapping and STM Observation of Conformational Isomers of a Bis(Terpyridine) Ligand from Metallosupramolecular Grids.* ChemPhysChem **16**, 1370 (2015).

[290] L. Gao, W. Ji, Y. B. Hu, Z. H. Cheng, Z. T. Deng, Q. Liu, N. Jiang, X. Lin, W. Guo, S. X. Du, W. A. Hofer, X. C. Xie, and H.-J. Gao. *Site-Specific Kondo Effect at Ambient Temperatures in Iron-Based Molecules.* Phys. Rev. Lett. **99**, 106402 (2007).

[291] B. W. Heinrich, L. Limot, M. V. Rastei, C. Iacovita, J. P. Bucher, D. M. Djimbi, C. Massobrio, and M. Boero. *Dispersion and Localization of Electronic States at a Ferrocene/Cu(111) Interface.* Phys. Rev. Lett. **107**, 216801 (2011).

[292] T. Knaak, T. G. Gopakumar, B. Schwager, F. Tuczek, R. Robles, N. Lorente, and R. Berndt. *Surface cis Effect: Influence of an Axial Ligand on Molecular Self-Assembly.* J. Am. Chem. Soc. **138**, 7544 (2016).

[293] T. Knaak. *Rastersondenmikroskopie an einem makrozyklischen Eisenkomplex auf Au(111).* Diploma thesis, Christian-Albrechts-Universität zu Kiel (2012).

[294] W. R. Scheidt and C. A. Reed. *Spin-state/Stereochemical Relationships in Iron Porphyrins: Implications for the Hemoproteins.* Chem. Rev. **81**, 543 (1981).

[295] V. Goulle, A. Harriman, and J.-M. Lehn. *An electro-photoswitch: redox switching of the luminescence of a bipyridine metal complex.* J. Chem. Soc., Chem. Commun., **0**, 1034 (1993).

[296] O.-S. Jung, D. H. Jo, Y.-A. Lee, B. J. Conklin, and C. G. Pierpont. *Bistability and Molecular Switching for Semiquinone and Catechol Complexes of Cobalt. Studies on Redox Isomerism for the Bis(pyridine) Ether Series Co(py$_2$X)(3,6-DBQ)$_2$, X = O, S, Se, and Te.* Inorg. Chem. **36**, 19 (1997).

[297] C. E. Powell, M. P. Cifuentes, J. P. Morrall, R. Stranger, M. G. Humphrey, M. Samoc, B. Luther-Davies, and G. A. Heath. *Organometallic Complexes for Nonlinear Optics. 30.[1] Electrochromic Linear and Nonlinear Optical Properties of Alkynylbis(diphosphine)ruthenium Complexes.* J. Am. Chem. Soc. **125**, 602 (2003).

[298] K. Tanaka, N. Kitamura, Y. Takahashi, and Y. Chujo. *Reversible signal regulation system of ^{19}F NMR by redox reactions using a metal complex as a switching module.* Bioorgan. Med. Chem. **17**, 3818 (2009).

[299] T. Leoni, O. Guillermet, H. Walch, V. Langlais, A. Scheuermann, J. Bonvoisin, and S. Gauthier. *Controlling the Charge State of a Single Redox Molecular Switch.* Phys. Rev. Lett. **106**, 216103 (2011).

[300] D. A. Scherlis, M. Cococcioni, P. Sit, and N. Marzari. *Simulation of Heme Using DFT + U: A Step toward Accurate Spin-State Energetics.* J. Phys. Chem. B **111**, 7384 (2007).

[301] Y. Li Huang, Y. Lu, T. C. Niu, H. Huang, S. Kera, N. Ueno, A. T. S. Wee, and W. Chen. *Reversible single-molecule switching in an ordered monolayer molecular dipole array.* Small **8**, 1423 (2012).

[302] F. Sedona, M. Di Marino, D. Forrer, A. Vittadini, M. Casarin, A. Cossaro, L. Floreano, A. Verdini, and M. Sambi. *Tuning the catalytic activity of Ag(110)-supported Fe phthalocyanine in the oxygen reduction reaction.* Nat. Mater. **11**, 970 (2012).

[303] K. Nilson, J. Åhlund, M.-N. Shariati, E. Göthelid, P. Palmgren, J. Schiessling, S. Berner, N. Mårtensson, and C. Puglia. *Rubidium Doped Metal-Free Phthalocyanine Monolayer Structures on Au(111).* J. Phys. Chem. C **114**, 12166 (2010).

[304] Y. Bai, F. Buchner, M. T. Wendahl, I. Kellner, A. Bayer, H.-P. Steinrück, H. Marbach, and J. M. Gottfried. *Direct Metalation of a Phthalocyanine Monolayer on Ag(111) with Coadsorbed Iron Atoms.* J. Phys. Chem. C **112**, 6087 (2008).

[305] X. Ge, C. Manzano, R. Berndt, L. T. Anger, F. Köhler, and R. Herges. *Controlled Formation of an Axially Bonded Co-Phthalocyanine Dimer.* J. Am. Chem. Soc. **131**, 6096 (2009).

[306] C. Isvoranu, B. Wang, K. Schulte, E. Ataman, J. Knudsen, J. N. Andersen, M. L. Bocquet, and J. Schnadt. *Tuning the spin state of iron phthalocyanine by ligand adsorption.* J. Phys.: Condens. Matter **22**, 472002 (2010).

[307] C. Wäckerlin, D. Chylarecka, A. Kleibert, K. Müller, C. Iacovita, F. Nolting, T. A. Jung, and N. Ballav. *Controlling spins in adsorbed molecules by a chemical switch.* Nat. Commun. **1**, 1 (2010).

[308] K. Seufert, W. Auwärter, and J. V. Barth. *Discriminative Response of Surface-Confined Metalloporphyrin Molecules to Carbon and Nitrogen Monoxide.* J. Am. Chem. Soc. **132**, 18141 (2010).

[309] K. Seufert, M.-L. Bocquet, W. Auwärter, A. Weber-Bargioni, J. Reichert, N. Lorente, and J. V. Barth. *Cis-dicarbonyl binding at cobalt and iron porphyrins with saddle-shape conformation.* Nat. Chem. **3**, 114 (2011).

[310] T. Tanaka and A. Osuka. *Conjugated porphyrin arrays: synthesis, properties and applications for functional materials.* Chem. Soc. Rev. **44**, 943 (2015).

[311] Y. F. Wang, K. Wu, J. Kröger, and R. Berndt. *Structures of phthalocyanine molecules on surfaces studied by STM.* AIP Adv. **2**, 041402 (2012).

[312] W. Auwärter, D. Écija, F. Klappenberger, and J. V. Barth. *Porphyrins at interfaces.* Nat. Chem. **7**, 105 (2015).

[313] K. W. Hipps, L. Scudiero, D. E. Barlow, and M. P. Cooke. *A Self-Organized 2-Dimensional Bifunctional Structure Formed by Supramolecular Design.* J. Am. Chem. Soc. **124**, 2126 (2002).

[314] M. de Wild, S. Berner, H. Suzuki, H. Yanagi, D. Schlettwein, S. Ivan, A. Baratoff, H.-J. Güntherodt, and T. A. Jung. *A Novel Route To Molecular Self-Assembly: Self-Intermixed Monolayer Phases.* ChemPhysChem **3**, 881 (2002).

[315] D. Bonifazi, H. Spillmann, A. Kiebele, M. de Wild, P. Seiler, F. Cheng, H.-J. Güntherodt, T. Jung, and F. Diederich. *Supramolecular Patterned Surfaces Driven by Cooperative Assembly of C_{60} and Porphyrins on Metal Substrates.* Angew. Chem. Int. Ed. **43**, 4759 (2004).

[316] Z.-Y. Yang, S.-B. Lei, L.-H. Gan, L.-J. Wan, C. Wang, and C.-L. Bai. *The Effect of Polarity on Coadsorbed Molecular Nanostructures of Substituted Phthalocyanine and Thiol Molecules.* ChemPhysChem **6**, 65 (2005).

[317] Y. L. Huang, W. Chen, and A. T. S. Wee. *Molecular Trapping on Two-Dimensional Binary Supramolecular Networks.* J. Am. Chem. Soc. **133**, 820 (2011).

[318] F. Buchner, K. Seufert, W. Auwärter, D. Heim, J. V. Barth, K. Flechtner, J. M. Gottfried, H.-P. Steinrück, and H. Marbach. *NO-Induced Reorganization of Porphyrin Arrays.* ACS Nano **3**, 1789 (2009).

[319] T. G. Gopakumar, F. Matino, B. Schwager, A. Bannwarth, F. Tuczek, and R. Berndt. *Coverage Driven Formation of Homochiral Domains of an Achiral Molecule on Au(111).* J. Phys. Chem. C **114**, 18247 (2010).

[320] W. H. Woodruff, R. W. Pastor, and J. C. Dabrowiak. *Resonance Raman Studies of Macrocyclic Complexes. 1. Structural and Electronic Effects in Synthetic Metal(II) Porphyrin Analogues.* J. Am. Chem. Soc. **98**, 7999 (1976).

[321] G. Kresse and J. Furthmüller. *Efficiency of ab-initio total energy calculations for metals and semiconductors using a plane-wave basis set.* Comput. Mater. Sci. **6**, 15 (1996).

[322] A. Tkatchenko and M. Scheffler. *Accurate Molecular Van der Waals Interactions from Ground-State Electron Density and Free-Atom Reference Data.* Phys. Rev. Lett. **102**, 073005 (2009).

[323] G. Kresse and D. Joubert. *From ultrasoft pseudopotentials to the projector augmented-wave method.* Phys. Rev. B **59**, 1758 (1999).

[324] S. L. Dudarev, G. A. Botton, S. Y. Savrasov, C. J. Humphreys, and A. P. Sutton. *Electron-energy-loss spectra and the structural stability of nickel oxide: An LSDA+U study.* Phys. Rev. B **57**, 1505 (1998).

[325] M. C. Weiss, B. Bursten, S.-M. Peng, and V. L. Goedken. *Effects of peripheral steric constraints and metal ion size on the structure of three five-coordinate macrocyclic ligand complexes of the type [M($C_{22}H_{22}N_4$)X], M = cobalt(III), iron(III), manganese(II); X = iodine, chlorine, triethylamine.* J. Am. Chem. Soc. **98**, 8021 (1976).

[326] U. Harten, A. M. Lahee, J. P. Toennies, and C. Wöll. *Observation of a soliton reconstruction of Au(111) by high-resolution helium-atom diffraction.* Phys. Rev. Lett. **54**, 2619 (1985).

[327] C. Wöll, S. Chiang, R. J. Wilson, and P. H. Lippel. *Determination of atom positions at stacking-fault dislocations on Au(111) by scanning tunneling microscopy.* Phys. Rev. B **39**, 7988 (1989).

[328] A. Borgogno, F. Rastrelli, and A. Bagno. *Predicting the spin state of paramagnetic iron complexes by DFT calculation of proton NMR spectra.* Dalton Trans. **43**, 9486 (2014).

[329] J. Gottfried, K. J. Schmidt, S. L. M. Schroeder, and K. Christmann. *Adsorption of carbon monoxide on Au(110)-(*1×2*).* Surf. Sci. **536**, 206 (2003).

[330] F. Charra and J. Cousty. *Surface-induced chirality in a self-assembled monolayer of discotic liquid crystal.* Phys. Rev. Lett. **80**, 1682 (1998).

[331] K. E. Plass, A. L. Grzesiak, and A. J. Matzger. *Molecular Packing and Symmetry of Two-Dimensional Crystals.* Acc. Chem. Res. **40**, 287 (2007).

[332] K.-H. Ernst. *Molecular chirality at surfaces.* Phys. Status Solidi B **249**, 2057 (2012).

[333] G. Pawin, K. L. Wong, K.-Y. Kwon, and L. Bartels. *A Homomolecular Porous Network at a Cu(111) Surface.* Science **313**, 961 (2006).

[334] V. L. Goedken, S.-M. Peng, J. A. Molin-Norris, and Y.-a. Park. *Carbon monoxide complexes of iron(II): synthesis and structural studies of five-and six-coordinate complexes of the macrocyclic ligand,* $C_{22}H_{22}N_4$. J. Am. Chem. Soc. **98**, 8391 (1976).

[335] A. Klose, J. Hesschenbrouck, E. Solari, M. Latronico, C. Floriani, N. Re, A. Chiesi-Villa, and C. Rizzoli. *The metal-carbon multiple bond in iron(I)- and iron(II)-dibenzotetramethyltetra[14]azaannulene: carbene, carbonyl, and isocyanide derivatives.* J. Organomet. Chem. **591**, 45 (1999).

[336] A. L. P. Silva, L. F. de Almeida, A. L. B. Marques, J. d. J. G. Varela, A. A. Tanaka, and A. B. F. da Silva. *CO bonding in* FeN_4 *complexes and the effect of the macrocycle ligand: A DFT study.* Polyhedron **67**, 36 (2014).

[337] N. Knorr, H. Brune, M. Epple, A. Hirstein, M. A. Schneider, and K. Kern. *Long-range adsorbate interactions mediated by a two-dimensional electron gas.* Phys. Rev. B **65**, 115420 (2002).

[338] F. Silly, M. Pivetta, M. Ternes, F. Patthey, J. P. Pelz, and W. D. Schneider. *Creation of an Atomic Superlattice by Immersing Metallic Adatoms in a Two-Dimensional Electron Sea.* Phys. Rev. Lett. **92**, 016101 (2004).

[339] Y. Wang, X. Ge, C. Manzano, J. Kröger, R. Berndt, W. A. Hofer, H. Tang, and J. Cerda. *Supramolecular patterns controlled by electron interference and direct intermolecular interactions.* J. Am. Chem. Soc. **131**, 10400 (2009).

[340] Z. Cheng, L. Gao, Z. Deng, N. Jiang, Q. Liu, D. Shi, S. Du, H. Guo, and H.-J. Gao. *Adsorption Behavior of Iron Phthalocyanine on Au(111) Surface at Submonolayer Coverage.* J. Phys. Chem. C **111**, 9240 (2007).

[341] J. Fraxedas, S. García-Gil, S. Monturet, N. Lorente, I. Fernández-Torrente, K. J. Franke, J. I. Pascual, A. Vollmer, R.-P. Blum, N. Koch, and P. Ordejón. *Modulation of Surface Charge Transfer through Competing Long-Range Repulsive versus Short-Range Attractive Interactions.* J. Phys. Chem. C **115**, 18640 (2011).

[342] A. Vilan, D. Aswal, and D. Cahen. *Large-Area, Ensemble Molecular Electronics: Motivation and Challenges.* Chem. Rev. **117**, 4248 (2017).

[343] C. Jia, A. Migliore, N. Xin, S. Huang, J. Wang, Q. Yang, S. Wang, H. Chen, D. Wang, B. Feng, Z. Liu, G. Zhang, D.-H. Qu, H. Tian, M. A. Ratner, H. Q. Xu, A. Nitzan, and X. Guo. *Covalently bonded single-molecule junctions with stable and reversible photoswitched conductivity.* Science **352**, 1443 (2016).

[344] S. Sanvito. *Molecular spintronics.* Chem. Soc. Rev. **40**, 3336 (2011).

[345] N. Fuentes, A. Martín-Lasanta, L. Álvarez de Cienfuegos, M. Ribagorda, A. Parra, and J. M. Cuerva. *Organic-based molecular switches for molecular electronics.* Nanoscale **3**, 4003 (2011).

[346] H. Naggert, A. Bannwarth, S. Chemnitz, T. von Hofe, E. Quandt, and F. Tuczek. *First observation of light-induced spin change in vacuum deposited thin films of iron spin crossover complexes.* Dalton Trans. **40**, 6364 (2011).

[347] B. Warner, J. C. Oberg, T. G. Gill, F. El Hallak, C. F. Hirjibehedin, M. Serri, S. Heutz, M.-A. Arrio, P. Sainctavit, M. Mannini, G. Poneti, R. Sessoli, and P. Rosa. *Temperature- and Light-Induced Spin Crossover Observed by X-ray Spectroscopy on Isolated Fe(II) Complexes on Gold.* J. Phys. Chem. Lett. **4**, 1546 (2013).

[348] E. Ludwig, H. Naggert, M. Kalläne, S. Rohlf, E. Kröger, A. Bannwarth, A. Quer, K. Rossnagel, L. Kipp, and F. Tuczek. *Iron(II) Spin-Crossover Complexes in Ultrathin Films: Electronic Structure and Spin-State Switching by Visible and Vacuum-UV Light.* Angew. Chem. Int. Ed. **53**, 3019 (2014).

[349] M. Magott, O. Stefańczyk, B. Sieklucka, and D. Pinkowicz. *Octacyanidotungstate(IV) Coordination Chains Demonstrate a Light-Induced Excited Spin State Trapping Behavior and Magnetic Exchange Photoswitching.* Angew. Chem. Int. Ed. **56**, 13283 (2017).

[350] M. Gruber, T. Miyamachi, V. Davesne, M. Bowen, S. Boukari, W. Wulfhekel, M. Alouani, and E. Beaurepaire. *Spin crossover in $Fe(phen)_2(NCS)_2$ complexes on metallic surfaces.* J. Chem. Phys. **146**, 092312 (2017).

[351] E. C. Constable. *Terpyridines: From chemical obscurity to common supramolecular motifs.* Chem. Soc. Rev. **36**, 246 (2007).

[352] G. D. Harzmann. *Novel Tailor-Made Externally Triggerable Single-Molecular Switches for Molecular Electronics.* Ph.D. thesis, Universität Basel (2014).

[353] G. D. Harzmann, R. Frisenda, H. S. J. van der Zant, and M. Mayor. *Single-molecule spin switch based on voltage-triggered distortion of the coordination sphere.* Angew. Chem. Int. Ed. **54**, 13425 (2015).

[354] J. J. Parks, A. R. Champagne, T. A. Costi, W. W. Shum, A. N. Pasupathy, E. Neuscamman, S. Flores-Torres, P. S. Cornaglia, A. A. Aligia, C. A. Balseiro, and others. *Mechanical Control of Spin States in Spin-1 Molecules and the Underscreened Kondo Effect.* Science **328**, 1370 (2010).

[355] E. A. Osorio, K. Moth-Poulsen, H. S. J. van der Zant, J. Paaske, P. Hedegård, K. Flensberg, J. Bendix, and T. Bjørnholm. *Electrical Manipulation of Spin States in a Single Electrostatically Gated Transition-Metal Complex.* Nano Lett. **10**, 105 (2010).

[356] R. Davidson, O. A. Al-Owaedi, D. C. Milan, Q. Zeng, J. Tory, F. Hartl, S. J. Higgins, R. J. Nichols, C. J. Lambert, and P. J. Low. *Effects of Electrode-Molecule Binding and Junction Geometry on the Single-Molecule Conductance of bis-*$2,2':6',2''$*-Terpyridine-based Complexes.* Inorg. Chem. **55**, 2691 (2016).

[357] X. Zhang, Z.-X. Wang, H. Xie, M.-X. Li, T. J. Woods, and K. R. Dunbar. *A cobalt(II) spin-crossover compound with partially charged TCNQ radicals and an anomalous conducting behavior.* Chem. Sci. **7**, 1569 (2016).

[358] R. Sakamoto, K.-H. Wu, R. Matsuoka, H. Maeda, and H. Nishihara. π*-Conjugated bis(terpyridine)metal complex molecular wires.* Chem. Soc. Rev. **44**, 7698 (2015).

[359] H. Maeda, R. Sakamoto, and H. Nishihara. *Interfacial synthesis of electrofunctional coordination nanowires and nanosheets of bis(terpyridine) complexes.* Coord. Chem. Rev. **346**, 139 (2017).

[360] T. Brandl. *Multifold-Linked Fe(II) Terpyridine Cage Complexes.* Master's Thesis, Universität Basel (2015).

[361] G. D. Harzmann, R. Frisenda, H. S. J. van der Zant, and M. Mayor. *Single-molecule spin switch based on voltage-triggered distortion of the coordination sphere.* Angew. Chem., Int. Ed. **54**, 13425 (2015).

[362] G. D. Harzmann, M. Neuburger, and M. Mayor. *4,4-Disubstituted Terpyridines and Their Homoleptic Fe Complexes.* Eur. J. Inorg. Chem. **2013**, 3334 (2013).

[363] S. T. Howard. *Conformers, Energetics, and Basicity of 2,2'-Bipyridine.* J. Am. Chem. Soc. **118**, 10269 (1996).

[364] D. Syomin, J. Kim, B. E. Koel, and G. B. Ellison. *Identification of Adsorbed Phenyl* (C_6H_5) *Groups on Metal Surfaces: Electron-Induced Dissociation of Benzene on Au(111).* J. Phys. Chem. B **105**, 8387 (2001).

[365] K. Tonigold and A. Groß. *Adsorption of small aromatic molecules on the (111) surfaces of noble metals: A density functional theory study with semiempirical corrections for dispersion effects.* J. Chem. Phys. **132**, 224701 (2010).

[366] A. Pronschinske, Y. Chen, G. F. Lewis, D. A. Shultz, A. Calzolari, M. Buongiorno Nardelli, and D. B. Dougherty. *Modification of Molecular Spin Crossover in Ultrathin Films*. Nano Lett. **13**, 1429 (2013).

[367] S.-D. Jiang, B.-W. Wang, H.-L. Sun, Z.-M. Wang, and S. Gao. *An Organometallic Single-Ion Magnet*. J. Am. Chem. Soc. **133**, 4730 (2011).

[368] M. Jeletic, P.-H. Lin, J. J. Le Roy, I. Korobkov, S. I. Gorelsky, and M. Murugesu. *An Organometallic Sandwich Lanthanide Single-Ion Magnet with an Unusual Multiple Relaxation Mechanism*. J. Am. Chem. Soc. **133**, 19286 (2011).

[369] Y.-S. Meng, C.-H. Wang, Y.-Q. Zhang, X.-B. Leng, B.-W. Wang, Y.-F. Chen, and S. Gao. *(Boratabenzene)(cyclooctatetraenyl) lanthanide complexes: a new type of organometallic single-ion magnet*. Inorg. Chem. Front. **3**, 828 (2016).

[370] K. L. M. Harriman and M. Murugesu. *An Organolanthanide Building Block Approach to Single-Molecule Magnets*. Acc. Chem. Res. **49**, 1158 (2016).

Acknowledgment

First of all, I would like to express my sincere gratitude to my adviser Prof. Dr. Richard Berndt for the opportunity to do research in his group and to write this thesis. Literally, his door is always open: At all times, he was ready for help and fruitful discussions about research, our publications or my thesis.
Besides, I would like to thank

- Manuel Gruber for our joint research, all the support and proofreading of my thesis.
- Thiruvancheril G. Gopakumar and Nadine Hauptmann for good mentoring at the beginning of my PhD time.
- Bettina Schwager and Prof. Dr. Felix Tuczek for the synthesis of the FeTMTAA molecules and valuable discussions.
- Christoph Lindström, Sarah Puhl, Florian Benner, Alejandra Escribano, and Prof. Dr. Jürgen Heck for the synthesis of the interconnected cobalt-based complexes and valuable discussions.
- Gero D. Harzmann, Thomas Brandl, and Prof. Dr. Marcel Mayor for the synthesis of the $Fe(tpy)_2$ SCO complexes and valuable discussions.
- Marie-Laure Bocquet, Nicolás Lorente, and Roberto Robles for on-surface DFT calculations and valuable discussions.
- Christian Hamann for the ESI setup and answering many questions about it.
- Kristof Buchmann, Sujoy Karan, Alexander Köbke, and Katharina Scheil for excellent teamwork in the ESI-lab.
- René Woltmann for technical advice and always quick and flawless manufacturing of components that were essential for the operation of the ESI lab.
- Jörg Neubauer and Hans-Joachim Neumann for technical assistance regarding the computers and the electronics equipment.
- my office mates Lars Mühlenberend, Simon Altenburg, and Jan Homberg.

- Alexander Weismann and Thomas Jürgens for answering any experimental and theoretical question.
- Michael Mohr, Svenja Mühlenberend, Peter-Jan Peters, Natalia Schneider, Johannes Schöneberg, Torben Jasper-Tönnies and all of my other colleagues and former coworkers for an always pleasant atmosphere in the group.
- Monika Seeger for perfect help with any administration matters.
- the Deutsche Forschungsgemeinschaft for financial support through SFB668 and SFB677.

Finally, I would like to thank my parents, my brother, my sister, and Leonie for unconditional support.

Typeset in LaTeX.